Copyright © 2005, by the author(s).
All rights reserved.

Permission to make digital or hard copies of all or part of this work for personal or classroom use is granted without fee provided that copies are not made or distributed for profit or commercial advantage and that copies bear this notice and the full citation on the first page. To copy otherwise, to republish, to post on servers or to redistribute to lists, requires prior specific permission.

MODELING AND CALIBRATION OF RESIST PROCESSES IN PHOTOLITHOGRAPHY

by

Lei Yuan

Memorandum No. UCB/ERL M05/26

1 May 2005

MODELING AND CALIBRATION OF RESIST PROCESSES IN PHOTOLITHOGRAPHY

by

Lei Yuan

Memorandum No. UCB/ERL M05/26

1 May 2005

ELECTRONICS RESEARCH LABORATORY

College of Engineering
University of California, Berkeley
94720

Modeling and Calibration of Resist Processes in Photolithography

By

Lei Yuan

Spring 2005

This research is fully funded by SRC/DARPA under grants SRC 01_MC_460 and DARPA MDA972-01-1-0021.

Modeling and Calibration of Resist Processes in Photolithography

by

Lei Yuan

B.S. (University of Science and Technology of China) 1995
M.E. (University of Science and Technology of China) 1998

A dissertation submitted in partial satisfaction of the

requirements for the degree of

Doctor of Philosophy

in

Mechanical Engineering

in the

GRADUATE DIVISION

of the

UNIVERSITY of CALIFORNIA, BERKELEY

Committee in charge:

Professor Andrew R. Neureuther, Chair
Professor David B. Bogy
Professor Jeffrey Bokor
Professor Panayiotis Papadopoulos

Spring 2005

The dissertation of Lei Yuan is approved:

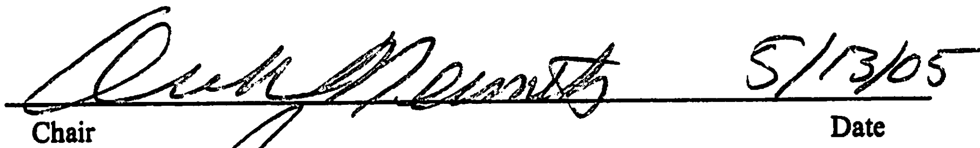

Chair Date

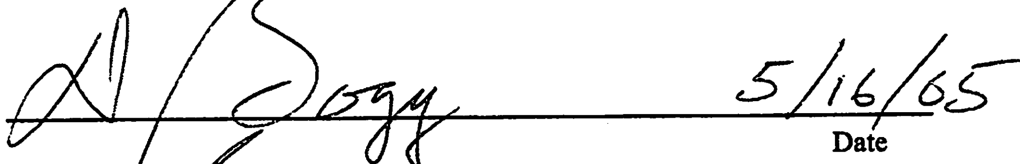

Date

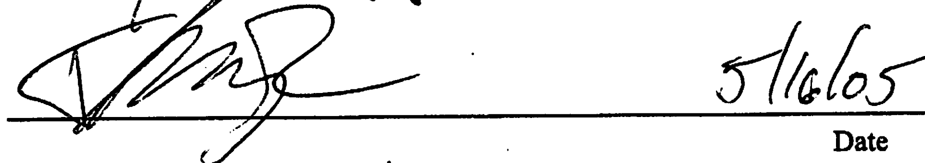

Date

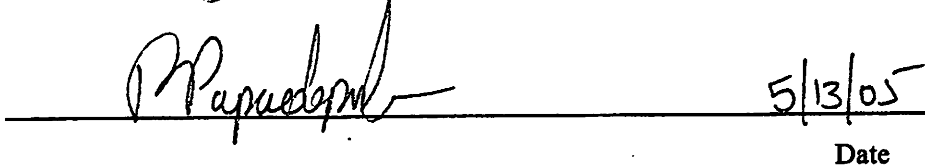

Date

University of California, Berkeley

Spring 2005

Modeling and Calibration of Resist Processes in Photolithography

Copyright © 2005

By

Lei Yuan

Abstract

Modeling and Calibration of Resist Processes in Photolithography

by

Lei Yuan

Doctor of Philosophy in Mechanical Engineering

University of California, Berkeley

Professor Andrew R. Neureuther, Chair

Research in this dissertation is to model resist recording processes from imaging to resist on wafer of both continuous and microscopic scales by developing new models as well as designing super sensitive test patterns for model calibration. An enhanced simulation platform — STORM-II is first developed to carry out the study of quantitative resist modeling in this dissertation. With an improved finite element implementation, STORM-II improves computation speed by a factor of 4~9 compared with the previous version.

State-dependent acid diffusion during post-exposure bake (PEB) is investigated with the help of a new insight to the preferential effect of acid transportation. Based on this new insight, three resist structures being sensitive to diffusion type are employed to characterize acid diffusion, which are sequentially double exposed cross, standing waves and double exposed sharp tip (DEST). Two chemically-amplified resists (CARs) — IBM APEX-E and Shipley UV210 are examined and acid transportation is found to be retarded by resist reaction in both resists resulting in reduced non-Fickian acid diffusion.

In this dissertation, DEST has been applied to enhance by one order of magnitude the sensitivity of resist profile to material phenomena. DEST has been successfully employed to visualize and calibrate acid contamination, quencher surface loss and to monitor minor fluctuation of process conditions. A fundamental tradeoff between resist resolution and resist blur is illustrated through correlating the radius of the DEST tip (the smallest printed feature) with imaging non-uniformity (standing waves).

The research of quencher effect begins with an in-depth study of a new acid-equilibrium-quencher (AEQ) modeling that is first proposed by Dr. Nagahara. Quencher study is conducted through interpreting resist reaction kinetics of both a weak acid KrF model resist and a strong acid ArF model resist over a variety of quencher loadings and exposure conditions. First and strong evidence of acid buffering effect is shown in the KrF model resist. Two different quencher mechanisms of both with and without acid buffering effect are found to exist depending on different acid strength.

In addition to quantifying macroscopic CD, line-edge roughness as statistical CD variation is also investigated leading to the development of continuous-based LER modeling strategy. This new approach is able to evaluate the effects of process conditions on LER formation without numerical complexity and has been applied to analyze LER generation as influenced by shot noise, flare and non-Fickian acid diffusion. A stress/strain induced crack propagation LER model is proposed to understand the mysterious large correlation distance in LER.

Other than rigorous resist modeling, in this dissertation, two compact resist models — RTM-α and RTM-β are developed to conduct rapid and accurate evaluation of resist effects in 2D layout printing. These two models improve prediction accuracy significantly compared with two commercially available compact models as verified using LSI Logic 130nm technology.

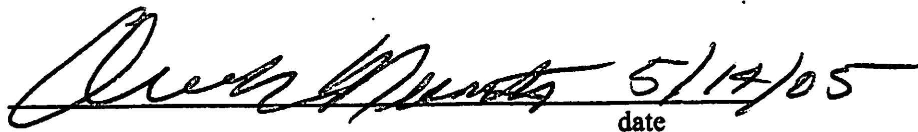

date

Professor Andrew R. Neureuther

Committee chair

TABLE OF CONTENTS

Chapter 1 Introduction 1

1.1 Lithography basics 1

1.2 Scope of this dissertation 2

Chapter 2 Background and Content 6

2.1 Background of lithography technology 6

2.2 Background of resist modeling 7

2.3 Contents of this dissertation 10

2.3.1 Development of STORM-II 11

2.3.2 Characterization of non-Fickian acid diffusion during PEB 11

2.3.3 DEST as sensitive test pattern for resist characterization 15

2.3.4 In-depth study of acid-equilibrium-quencher (AEQ) model 16

2.3.5 Development of continuous line-edge roughness (LER) modeling.......... 18

2.3.6 Development of two-dimensional resist threshold model (RTM) 21

Chapter 3 Development of STORM-II 23

3.1 Abstract 23

3.2 Resist models in STORM-II 23

3.2.1 Resist model in previous STORM 23

3.2.2 Acid and quencher mutual diffusion model 25

3.2.3 Acid-equilibrium-quencher (AEQ) model 25

3.2.4 Model of resist surface phenomena 26

3.3 Finite element method in STORM-II 26

3.3.1 Time space discretization 27

3.3.2 Finite element formulation of acid and quencher mutual diffusion.......... 29

3.4 Numerical performance of STORM-II 31

Chapter 4 Characterization of non-Fickian Acid Diffusion in DUV Chemically-amplified Resist (CAR) 34

4.1 Abstract 34

4.2 Acid diffusion sensitive test patterns.......... 35

4.3 Characterization of IBM APEX-E and Shipley UV210 based on diffusion

sensitive patterns 42
4.4 Study of multi-dissolution model using programmed double exposure 50
4.5 Conclusions 54
Chapter 5 Applying Double Exposed Sharp Tip (DEST) Technique to Characterize
Material Phenomena in DUV Photoresist 56
5.1 Abstract 56
5.2 Double exposed sharp tip (DEST) technique 57
5.3 Experiment conditions 59
5.4 Fundamental tradeoff between resist resolution and blur in lithography..... 60
5.5 DEST for visualizing resist substrate interaction 62
5.6 Modeling of resist substrate and top surface interaction 65
5.7 DEST application in characterizing non-Fickian acid diffusion 68
5.8 DEST application as accurate process monitor 72
5.9 Conclusions 74
Chapter 6 Understanding Quencher Mechanism by Considering Photoacid Dissociation
Equilibrium in Chemically-amplified Resist 76
6.1 Abstract 76
6.2 Concepts of full-dissociation-quencher (FDQ) model and
acid-equilibrium-quencher (AEQ) model 77
6.3 Experimental preparation 80
6.3.1 Resist materials 80
6.3.2 Real-time FTIR measurement of reaction kinetics 82
6.4 AEQ modeling in STORM-II 86
6.5 Experimental verification of FDQ and AEQ 87
6.5.1 Modeling reaction kinetics for KrF model resist 87
6.5.2 Modeling reaction kinetics for ArF model resist 92
6.5.3 Discussion of quencher effect in both model resists 96
6.6 Calculation of exposure latitude and environmental stability by applying AEQ
model 102
6.7 Conclusions 104
Chapter 7 Investigation of Shot-noise Induced Line Edge Roughness by Continuous

Model Based Simulation 106
7.1 Abstract 106
7.2 Concepts of continuous LER modeling 107
7.2.1 Modeling of exposure statistics 107
7.2.2 Modeling of post-exposure bake 108
7.2.3 Statistical lateral dissolution model (SLDM) 110
7.3 Effect of acid diffusion type on line-edge roughness 112
7.4 Study of shot noise effect with flare 115
7.5 Effect of resist contrast on line-edge roughness 118
7.6 Analysis of large unlikely resist event (LURE) 119
7.7 Stress induced crack propagation LER model 121
7.8 Conclusions 124
Chapter 8 Development of Fast Resist Model for Accurate Prediction of Two-Dimension Layout 126
8.1 Abstract 126
8.2 Pattern dependency of resist threshold 127
8.3 Formulation of two new resist threshold model 130
8.4 Numerical verification of resist threshold model 134
8.5 Experimental verification of resist threshold model 139
8.6 Conclusions 143
Chapter 9 Summary 144
Bibliography 149

FIGURES

Figure 2.1 Chemically-amplified resist process 9

Figure 3.1 Example of STORM-II simulation (a) T shape pattern (top view) (b) simulated resist profile 24

Figure 3.2 (a) 2D elbow resist pattern and speed comparison (b) at various diffusion constants ω (c) at various D_0 33

Figure 4.1 (a) scheme of double exposed cross pattern (b) double exposed cross pattern of 0.3um trench (UV210) (c) double exposed cross pattern of 0.4um trench (UV210) 36

Figure 4.2 STORM simulation of double exposed cross pattern (a) no acid diffusion (b) acid diffusion 37

Figure 4.3 Acid transportation in sequentially double exposed cross structure as predicted by ENF and RNF diffusion types 39

Figure 4.4 Acid transportation in sequentially double exposed cross structure as predicted by ENF and RNF diffusion types........ 40

Figure 4.5 (a) Image intensity of standing waves (b) Acid movement in the region of standing waves predicted by enhanced and reduced non-Fickian diffusion modes 41

Figure 4.6 (a) Image intensity of standing waves (b) resist profile predicted by enhanced non-Fickian diffusion model (c) resist profile predicted by reduced non-Fickian diffusion model (d)) resist profile predicted by Fickian diffusion model... 42

Figure 4.7 Dose-to-clear verse PEB time for (a) APEX-E (b) UV210 45

Figure 4.8 Experimental measurements and simulation prediction of (a) 1D trench widths (b) the corner-to-corner spacing of sequentially double exposed cross pattern in APEX-E.. 46

Figure 4.9 Resist profile resulting from standing waves in APEX-E (a) predicted by Fickian diffusion model (b) predicted by reduced non-Fickian diffusion (c) SEM measurement 47

Figure 4.10 Experimental measurements and simulaiton predictions of (a) one-

dimensional trench width (b) corner-to-corner spacing of sequentially double exposed cross pattern in UV210 49

Figure 4.11 Resist profile resulting from standing waves in UV210 (a) predicted by Fickian diffusion model (b) predicted by reduced non-Fickian diffusion (c) SEM measurement 50

Figure 4.12 Image intensity of programmed foreground/background exposure of (a) trench (b) trench end gap 51

Figure 4.13 (a) Development thresholds of APEX-E for 1D trench and trench end pattern (b) Experimental measurements and predictions of trench widths assuming single-development threshold and multi-development threshold.... 53

Figure 4.14 Development threshold of UV210 for (a) 1D trench (b) trench end patterns 54

Figure 5.1 (a) Double exposed sharp tip technique (b) SEM of DEST wedge shape islands 58

Figure 5.2 Image intensity of (a) DEST technique (b) single exposed wedge shape pattern 59

Figure 5.3 Magnification factor of DEST over CD 59

Figure 5.4 (a) APEX-E DEST (b) UV210 DEST (c) Standing waves in APEX-E resist (d) Standing waves in UV210 resist 62

Figure 5.5 APEX-E DEST on (a) bare silicon (b) 80A silicon nitride (c) 900A silicon nitride (d) AR3-600 coating with RTC top coating 63

Figure 5.6 UV210 DEST (a) on bare silicon (b) on 80A silicon nitride (c) on AR3-600 coating 65

Figure 5.7 (a) APEX-E DEST on 80A silicon nitride (b) APEX-E DEST on 800A silicon nitride (c) DEST simulation assuming $K_S = 0$ (d) $K_S = -0.004$ (e) $K_S = -0.010$ 67

Figure 5.8 UV210 DEST on top of bare silicon (a) SEM (b) STORM-3D simulation, ... 68

Figure 5.9 (a) DEST structure (b) critical dimension (c) STORM-3D simulation of dimension variation upon diffusivity 69

Figure 5.10 Top-down wedge shape island of UV210 DEST as predicted by Fickian

and reduced non-Fickian diffusions at the same diffusion length................ 69

Figure 5.11 (a) standing wave on iso space (b) STORM simulation of deprotection contour assuming Fickian diffusion (c) STORM simulation of deprotection contour assuming reduced non-Fickian diffusion................................ 71

Figure 5.12 Standing wave effect on the DEST profile as predicted by assuming (a) Fickian diffusion (b) Reduced non-Fickian diffusion.......................... 72

Figure 5.13 Dimension changes of CD and DEST islands for UV210 resist upon (a) dose nonuniformity (b) PEB temperature variation............................. 73

Figure 5.14 Measurements of dimension changes of CD and DEST for APEX-E resist over PEB temperature variation...74

Figure 6.1 K_a range of fluorinated-super acid and non-fluorinated weaker acid. Acid becomes weaker in non-aqueous matrices.................. 79

Figure 6.2 KrF resist (non-fluorinated-weak-photoacid system)..............................81

Figure 6.3 ArF resist (fluorinated-strong-photoacid system).................. 82

Figure 6.4 Real time PEB FTIR measurement system.................................... 83

Figure 6.5 The reactions in model KrF model resist......................... 84

Figure 6.6 FTIR Spectra for KrF model resist... 84

Figure 6.7 The reactions in model ArF resist 85

Figure 6.8 FTIR Spectra for model ArF resist 85

Figure 6.9 AEQ fitting of the deprotection reaction (KrF model resist / 90°C PEB) (data points: FTIR measurements/solid curve: modeling fitting 88

Figure 6.10 Prediction of protection concentration at 60 sec 90°C PEB (a) FDQ model (k_r = 1.0, k_l = 0.24, k_n = 3.0, m = 0.8, C=0.03) (b) AEQ model (K_a = 0.03, k_r = 3.6, k_l = 0.275, k_n = 4.0, m = 0.72, C=0.03) (Triangles are experimental data and circles are the fitting results. $[HA]_{generated}$: photo generated acid, $[Q_0]$: initial quencher loading 90

Figure 6.11 Prediction of protection concentration at 60 sec 100°C PEB (a) FDQ model (k_r = 1.0, k_l = 0.06, k_n = 10.0, m = 0.8, C=0.03) (b) AEQ model (K_a = 0.03, k_r = 8.8, k_l = 0.24, k_n = 15.0, m = 0.88, C=0.03) (Triangles are experimental data and circles are the fitting results. $[HA]_{generated}$: photo generated acid, $[Q_0]$: initial quencher loading)................................ 90

Figure 6.12 Prediction of protection concentration at 60 sec 110°C PEB (a) FDQ model (k_r = 1.0, k_l = 0.12, k_n = 7.0, m = 0.8, C=0.03) (b) AEQ model (K_u = 0.03, k_r = 15.4 k_l = 0.22, k_n = 18.0, m = 1.02, C=0.03) (Triangles are experimental data and circles are the fitting results. $[HA]_{generated}$: photo generated acid, $[Q_0]$: initial quencher loading.) 91
Figure 6.13 Arrhenius plot for reactions in KrF resist 91
Figure 6.14 FDQ fitting of deprotection reaction (ArF resist / 120°C PEB). (data points: FTIR measurements/solid curve: modeling fitting) PEB 120°C: k_r = 2.2, k_l = 0.0, k_n = 4.44, m = 1.03, C=0.05 93
Figure 6.15 FDQ prediction of protection concentration at 60sec of 110°C PEB (k_r=0.22, k_l=0.0, k_n=1.33, m = 1.08, C=0.05) (triangles: experimental data/circles: model fitting) 93
Figure 6.16 FDQ prediction of protection concentration at 60sec 120°C PEB (k_r = 0.44, k_l = 0.0, k_n = 4.0, m = 1.03, C=0.05) (triangles: experimental data and circles: model fitting) 94
Figure 6.17 FDQ prediction of protection concentration at 60sec 130°C PEB (k_r=0.66, k_l =0.0, k_n=7.11, m = 0.75, C=0.05) (triangles: experimental data and circles: model fitting) 94
Figure 6.18 Arrhenius plot for deprotection and neutralization reactions in ArF model resist 96
Figure 6.19 Reaction contrast with various quencher loading (KrF resist/PEB 100°C) 101
Figure 6.20 Reaction contrast with various quencher loading (KrF resist/PEB 100°C) 101
Figure 6.21 Best dose variation with quencher loading 102
Figure 6.22 Exposure latitude calculation (AEQ model) 103
Figure 6.23 Environmental stability calculation (AEQ model) 104
Figure 7.1 (a) near-edge dissolution (b) lateral dissolution paths (c) mean and fluctuation of deprotection concentration 111
Figure 7.2 Dissolution rate curve 112
Figure 7.3 (a) near-edge dissolution (b) lateral dissolution paths (c) mean and fluctuation

of deprotection concentration..113
Figure 7.4 Deprotection concentration of partially exposed resist surface simulated by (a) RNF (b) FD (c) ENF..114
Figure 7.5 (a) Resist edge for LER simulation (b) LER calculation results...............115
Figure 7.6 (a) Image intensity with various flare ratios (b) Shot noise induced LER under different flare ratios..117
Figure 7.7 LER versus flare (a) KrF resist, UVII-HS (courtesy of M. Williamson [107] at UC Berkeley) (b) EUV resist, EUV-2D, (courtesy of M. Chandhok at Intel)... 118
Figure 7.8 (a) Dissolution rates for different n factor (b) LER versus n factor..............119
Figure 7.9 LURE generation and equivalent lateral dissolution path..................... 120
Figure 7.10 (a) Statistical distribution of resist edge deviation (b) probability of 2D defect..121
Figure 7.11 Correlation length of LER for (a) UVII-HS (KrF) (b) TOK11 (ArF) (c) EUV-2D (EUV)..123
Figure 7.12 Pattern deformation obtained by (a) using ZEP resist in X-ray lithography [88] (b) using Shipley EUV-2D resist in EUV lithography [89, 90].......... 124
Figure 8.1 (a) line-end gap (b) iso trench (c) trench-end gap (d) dense lines............ 129
Figure 8.2 Thresholds extracted from (a) SEM measurements (b) STORM simulations..129
Figure 8.3 (a) Line-end gap (b) dense lines (c) trench-end gap (d) Images on the normal direction (e) images on the transverse direction...........................133
Figure 8.4 Five variables used in 2D-RTM (a) three on the normal direction (b) two on transverse direction..133
Figure 8.5 (a) line end feature (b) image intensity along the normal cut (c) image contour..135
Figure 8.6 Results of fitting STORM simulations by use of RTM-β (a) average error of fitting Model 1 (b) maximum error of fitting Model 1 (c) average error of fitting Model 2 (b) maximum error of fitting Model 2...137
Figure 8.7 Results of fitting the first set of rigorous simulations (a) VTU (maximum/average errors: 55/12.5 nm) (b) VT-5 (maximum/average errors: 5.0/1.5nm) (c) RTM-α (maximum/average errors: 9.3/2.5nm) (d) RTM-β

(maximum/average errors: 5.8/1.7nm).. 138

Figure 8.8 Results of fitting the second set of rigorous simulations (a) VTU (maximum/average errors: 53/13 nm nm) (b) VT-5 (maximum/average errors: 5.46/1.58nm) (c) RTM-α (maximum/average errors: 9.6/2.5nm) (d) RTM-β (maximum/average errors: 4.15/1.55nm).. 139

Figure 8.9 Fitting errors for training procedure (a) VT-U (maximum/average errors: 7.4/2.67nm) (c) VT-5 (maximum/average errors: 3.25/1.23nm) (e) RTM-α (maximum/average errors: 3.7/1.4 nm) (g) RTM-β (maximum/average errors: 3.0/1.2 nm).. 141

Figure 8.10 Prediction errors for predicting procedure (a) VT-U (maximum/average errors: 11.0/4.0nm) (b) VT-5 (maximum/average errors: 5.6/2.8 nm) (c) RTM-α (maximum/average errors: 2.69/1.0 nm) (d) RTM-β (maximum/average errors: 4.0/1.8 nm).. 142

Acknowledgements

I am grateful to my advisor, Professor Andrew R. Neureuther for his great guidance and support in the past five years. His curiosity to scientific discoveries and persistence of being excellent and leading in academic research has motivated me to achieve this dissertation, and far more beyond. I would like to thank Professor Panayiotis Papadopoulos for serving as chair of my qualification examination and member of my dissertation committee. My thanks also go to Professor David Bogy, Professor Jeffrey Bokor and Professor Tsu-Jae King for serving on my qualification examination and dissertation committee.

I am truly thankful to Kim Chan of Berkeley Microlab for her consistent and excellent support on experimental work. Without her help, this dissertation would take much longer. I would like to thank Dr. Seiji Nagahara from NEC Electronics, who not only educated me much resist chemistry but also coordinated a productive research collaboration among Berkeley, NEC Electronics, JSR Micron and Litho Tech Japan, which resulted into one chapter of this dissertation.

I would like to thank my colleagues and friends, Dr. Ebo Croffie, Dr. Mosong Cheng, Dr. Bo Wu, Dr. Kostas Adam, Dr. Tom Pistor, Dr. Yunfei Deng, Dr. Mike Williamson, Dr. Yijian Cheng, Dr. Yashesh Shroff, Dr. Michael Shumway, Dr. Yan Wang, Dr. Runzhi (Tiger) Chang, Dr. Jason Cain, Mr. Charlie Zhang, Mr. Paul Friedberg, Dr. Frank

Gennari, Dr. Garth Robins, Mr. Michael Lam, Mr. Greg McIntyre, Mr. Wojtek Jacob Poppe, Mr. Scott Hafeman, Mr. Dan Ceperley. Their friendship has made my PhD study more interesting.

This research was fully funded by SRC/DARPA under grants SRC 01_MC_460 and DARPA MDA972-01-1-0021. Their generosity is greatly appreciated.

1 Introduction

1. Lithography basics

Lithography is a semiconductor manufacture process that transfers patterns from mask to wafers through an imaging system in a highly accurate, stable and efficient manner. Lithography technology has been and will continue to be a major driving force to sustain the amazing "Moore's Law" of integrated circuit industry that the number of transistors per unit area is doubled approximately every 18 months [1]. Cutting edge 90nm lithography technology is capable of printing 65nm line on wafer by the use of 193nm wavelength light rendering an amazing resolution of about one third wavelength [2]. Immersion lithography will be employed for next technology node and EUV lithography is the emerging technology. Photoresist as the recording medium to the imaging system is an important technology aspect of lithography and has been enhanced by the application of chemically-amplified resist (CAR) [3, 4]. The resist recording mechanism is the focus of this dissertation.

The challenges in the resist recording are to understand and put into engineering model many resist phenomena. For a CAR system, the efficiency of acid generation upon exposure determines resist sensitivity. Acid transportation during post-exposure bake

(PEB) is a major source of resist bias of latent edge formation. Resist profile is formed after development that has high selectivity to resist reaction level. Statistical nonuniformity of resist line is an important aspect of pattern printing and often called line-edge roughness (LER). Process robustness of the resist recording that is as important as critical dimension (CD) can be improved by adding quencher. These mechanisms are entangled in a complex manner and simulations can provide leverage on the integration.

2. Scope of this dissertation

This dissertation examines the resist recording process and establishes engineering models. The work began with the extension of STORM — a simulation platform developed in University of California at Berkeley for quantifying resist models in conjunction with parameter extraction. STORM-II is developed with improvements in both computation speed and simulation scope. Experiments were then of interest in observing effects of resist parameters. This led to the invention of a sequential double exposed cross pattern for visualizing acid diffusion phenomena and extracting model parameters. An extension of this double exposure method was applied to produce a double exposed resist sharp tip (DEST). The super sensitivity of DEST to material phenomena enabled accurate resist calibration. In the aspect of quencher mechanism, an in-depth study of acid buffering effect was executed through a collaborative work to understand the quencher effect. In addition to quantifying continuous mechanisms, line-edge roughness as statistical CD variation was also investigated leading to the development of continuous-based LER modeling strategy. While major effort of this

study was devoted to enhance rigorous resist modeling, the limitation of high computation cost of rigorous modeling drove the development of fast compact resist models in the last part of this dissertation.

Chapter 2 introduces the background and content of this dissertation. In chapter 3, STORM-II, an enhanced simulation platform for resist modeling, is introduced. Compared with previous STORM, a speed improvement of a factor of 4 ~ 9 can be achieved by STORM-II by the use of elemental variable elimination technique for finite element implementation.

In chapter 4, the existence of state-dependent acid transportation is determined and its influence on pattern printing is quantified for CAR systems. This state-dependent acid transportation is often called non-Fickian acid diffusion or type II acid diffusion. Although a great deal of efforts have been devoted to quantify non-Fickian acid diffusion, only limited success had been gained and even contradictive results are present due to a lack of understanding of non-Fickian diffusion as well as accurate test patterns. With the help of a new physical insight to non-Fickian diffusion, two diffusion sensitive patterns are used to characterize non-Fickian acid diffusion successfully, which are sequentially double exposed cross patterns and standing waves. Acid transportation is found to be retarded by resist reaction in both IBM APEX-E and Shipley UV210 resist.

In chapter 5, a modification of the double exposure technique as used in chapter 4 leads to the application of a double exposed sharp tip (DEST) technique. Lacking of test

patterns for accurate parameter extraction has been one of major challenges limiting the success of rigorous resist modeling. Being super sensitive to material phenomena, DEST thus provides an excellent way of visualizing and calibrating resist phenomena. In this chapter, DEST is applied to characterize non-Fickian acid diffusion, resist surface phenomena as well as to monitor process conditions.

In chapter 6, quencher effect is investigated through collaboration with Dr. Seiji Nagahara (NEC Electronics). Quencher is commonly used in advanced CA resists to improve resist performance in many aspects. Regardless of its extensive applications, there is no well established quencher modeling that is able to explain quencher effects and provide guidance for a better use of quencher. The study of quencher modeling began with in-depth examination of a new acid-equilibrium-quencher (AEQ) modeling that was originally proposed by Dr. Seiji Nagahara [19~21]. The study in chapter 7 shows that acid buffering effect exists in a weak acid KrF resist but not strong acid ArF resist, which indicates that two different quencher mechanisms are present depending on the acid strength.

In chapter 7, a continuous line-edge roughness (LER) modeling is developed to analyze the influences of process conditions on LER. This newly-developed LER model can be numerically implemented without computational complexity that constrains the application of molecular level LER simulations. This continuous LER modeling applies a discrete model of 1~2nm scale for exposure, continuous reaction-diffusion model of 5~7nm scale for post-exposure bake (PEB) and a newly developed statistical lateral

dissolution model (SLDM) of 1nm scale for development. This new LER modeling is applied to investigate the effects of shot noise, exposure flare and non-Fickian acid diffusion on LER formation. In addition to the above engineering model, stress/strain-induced crack propagation LER model is proposed to understand the large scale of correlation distance in LER that has not been predicted by any LER model to the best of author's knowledge. Only preliminary proof of this new physical LER model is presented here due to a lack of time.

The study in chapter 8 is in the aspect of compact resist modeling, where two new resist threshold models RTM-α and RTM-β have been developed for better predictions of 2D layout printing. Lithography simulation of large scale up to full chip layouts is needed in many aspects of lithography technologies, where the stringent requirement on model efficiency makes rigorous resist modeling not suitable due to prohibitive computation cost. Therefore, compact resist models are highly demanded. In this chapter, RTM-α determines resist edge location based on image intensities along directions both normal and parallel to resist edge while RTM-β defines resist edge based on both image intensity and the shape of image contour. The effectiveness of both models has been proved through extensive numerical and experimental studies and their accuracy has been compared with commercial compact models.

2 Background and Content

1. Background of lithography technology

A prediction made by Gordon E. Moore four years after the production of the first integrated circuit chip has guided IC industry for forty years. In 1965, Moore envisioned an exponential growth in the number of transistors per integrated circuit chip [1], which is well known as the "Moore's Law". Although the pace of growth appears to have slowed down recently, the number of transistors per unit area is doubled approximately every 18 months in past forty years, which is only made possible by continuous shrinkage of minimum feature size on chip. The major driving force to print ever-smaller transistors is the advancement of lithography technology.

In lithography process, patterns of circuit devices are transferred from mask to wafers through an imaging system in a highly accurate, stable and efficient manner. An irradiation sensitive material — photoresist is often used as the recording medium on wafer that allows subsequent pattern transfer to the underlying layers. Chemically-amplified resist (CAR) is the most widely used photoresist.

Cutting edge 90nm lithography technology can print isolated lines of one-third

wavelength and pitches of one half wavelength using Deep Ultra-Violet (DUV) light of 193nm wavelength [2]. Lithography technology is exceptionally challenging for three reasons. Firstly, resolution target in the state-of-art technology is well below so-called limit as indicated by Rayleigh resolution criteria aggressively pushing the limit of imaging system. Higher resolution can be achieved by implementing a shorter wavelength and high NA imaging system in combination of low K_1 process. Extreme Ultra-Violet (EUV) light source with 13.4nm wavelength will be used for emerging lithography. Secondly, resolution and robustness of the lithography process seem to be contradictive targets. For example, a high NA imaging system that achieves better resolution decreases depth of defocus (DOF). This difficulty leads to the development of immersion lithography. Another example is that, although EUV technology realizes very high resolution by the use of a short wavelength of 13.4nm, it is sensitive to small mask defects making EUV mask fabrication very difficult. Thirdly, the process control in leading technology is very stringent. Therefore, any imperfection in the lithography process, such as lens aberration, flare effect, exposure uniformity, PEB temperature fluctuation and resist uniformity are now of concerns and need to be evaluated carefully. All these issues can increase the complexity of lithography process exponentially.

2. Background of resist modeling

Rick Dill pioneered optical lithography modeling for his landmark papers published in 1975 [5~8]. In these papers, Dill introduced the first imaging model for incoherent illumination system and the first resist exposure model now known as the "Dill model".

In 1979, Neureuther and his collaborators published a series of papers exploring the influence of partial coherence illumination and etching process [9~12] and released the first lithography modeling tool SAMPLE [13]. Since then, tremendous effort has been devoted to this field and nowadays lithography modeling has become indispensable to lithography development and applications. Lithography modeling helps lithographers in almost every phase of lithography development, such as evaluating emerging technologies, optimizing process conditions and interpreting experimental observations. Many lithography simulation tools are available for lithography community, such as SAMPLE [13], PROLITH [14], SOLID-C [15], SUPREM [16], TEMPEST [17] and PANOROMIC [18].

Resist modeling, born in the same time as optical modeling, still remains immature while optical simulation tools have gained great success. CARs are generally composed of four components — photoacid generator (PAG), polymer resin, dissolution inhibitor and base quencher. PAG produces acid upon exposure to DUV or EUV light. During post-exposure bake (PEB), acid catalyzes thermal induced chemical reaction making the irradiated resist volume soluble in aqueous developer. This catalyzed reaction is often called deprotection reaction since the dissolution inhibitor groups (protected groups) are cleaved by this reaction. Meanwhile, acid diffusion from high dose region to low dose region will change resist latent edge formation as well as smooth material and image nonuniformity. In addition, a neutralization process between acid and quencher lessens acid diffusion. During PEB, many CARs exhibit first volume expansion and then shrinkage in PEB resulted from desorption of volatile by-product groups created by the

deprotection reaction. Figure 1 shows the schematic of a typical photoresist process flow.

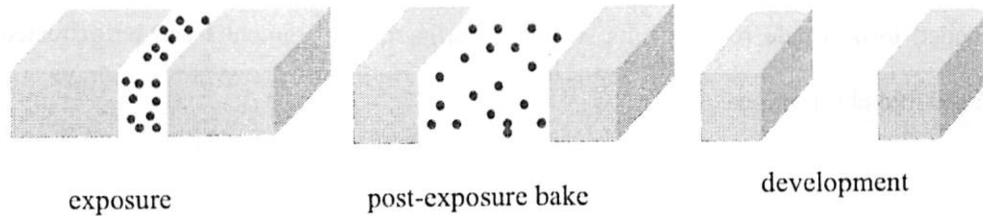

Fig. 1 Chemically-amplified resist process

According to ITRS roadmap, quantitative resist modeling is still a bottleneck for lithography simulation. Resist modeling is especially challenging due to the following three reasons.

Firstly, a chemically-amplified resist (CAR) system is a highly complex system in comparison with optics. Many material phenomena are present and entangled, such as PAG dissociation, acid diffusion, quencher diffusion, deprotection reaction, neutralization reaction, quencher buffering [19~21], resist film expansion and shrinkage, evaporation of volatile byproduct and possibly phase separation [22]. There are even greater complexities in immersion lithography, where material leaching into the liquid and water uptake are possible. Developing a comprehensive quantitative resist model is currently close to mission impossible.

Secondly, a fundament difficulty in quantifying resist model is that most of the resist

events cannot be observed or measured directly. To extract resist parameters, numerical interpretations of test patterns on wafers are often necessary. Since all resist phenomena are entangled in forming patterns, specifically designed test patterns are greatly demanded to decouple resist events so that specific resist parameters can be extracted from specific observations.

Thirdly, strong nonlinearity of resist modeling makes computer simulation vastly inefficient. The nonlinearity in resist modeling is due to state dependent acid diffusion, acid and quencher mutual diffusion and high resist dissolution contrast. Another fact that will complicate numerical implementation of resist modeling dramatically is that continuous modeling scheme will not be sufficient while the size of the simulation target goes down below or comparable to the size of polymer molecule. This challenge signifies the necessity to establish a multi-scale simulation scheme that would links the continuous modeling and the molecular dynamics in the near future.

3. Contents of this dissertation

Research in this dissertation is to model the mechanisms of pattern transfer from imaging to resist on wafer of both continuous and microscopic scales by developing new models as well as designing super sensitive test patterns for model characterization. Study in this dissertation explores several material phenomena critical for quantifying the resist recording process, including non-Fickian acid diffusion, quencher mechanism, line-edge roughness, pattern design for model calibration and fast compact model for full chip scale

simulation.

3.1 Development of STORM-II

STORM-II is a new version of simulation platform for resist models with enhancement in both modeling and algorithm and the ability of three-dimensional simulations. In the aspect of modeling, STORM-II incorporates acid/quencher mutual diffusion model, acid-equilibrium-quencher (AEQ) model, acid/quencher surface phenomena model and continuous LER simulation. In the aspect of numerical algorithm, a finite element method that applies elemental level variable elimination is used to reduce the size of the global equation system and thus improves computation efficiency. Speed improvement of a factor ranging from 4 ~ 9 will be obtained.

3.2 Characterization of non-Fickian acid diffusion during PEB

The improvement of resolution and sensitivity obtained by chemically-amplified resist (CAR) is largely due to a so-called amplification effect, which means one photo-generated acid is able to catalyze hundreds of deprotection reactions during PEB. This effect is only made possible with acid transportation in the resist matrix. Acid diffusion has been found to be a key resist event that influences latent pattern formation. It washes out standing waves, reduces line edge roughness, and sets intrinsic resolution limit [23]. Fukuda and other researchers [24, 25, 26] also proposed quencher diffusion during PEB. Quencher diffusion has not been fully explored due to the difficulty of separating acid and quencher diffusion effects.

Post-exposure bake (PEB) is often modeled as reaction-diffusion process that leads to the following equations,

$$\begin{aligned} \frac{\partial A}{\partial t} &= k_r(1-A)H^m \\ \frac{\partial H}{\partial t} &= \nabla(D\nabla H) - K_l H \end{aligned} \tag{1}$$

Here A and H are the normalized reacted site and acid concentration. The parameters k_r, k_l and D are reaction rate, acid loss rate and acid diffusivity respectively. Ferguson [27] first used IR absorption to monitor the extent of reaction and photoacid generation and found a factor m was needed to predict the extent of reaction over various exposure doses. A large body of literature of PEB modeling is present, most of which differ in how to model the state dependence of acid transportation. Some models even show contradictive results due to a lack of accurate methods to quantify resist models. Depending on how acid diffusivity is influenced by reacted sites, acid diffusion can be divided into three types, which are Fickian, enhanced non-Fickian and reduced non-Fickian types. In the Fickian diffusion type, the acid diffusivity remains a constant no matter what the level of deprotection is. In the enhanced non-Fickian diffusion type, the acid diffusivity increases due to the deprotection reaction, while it decreases in the reduced non-Fickean type. Non-Fickian diffusion is sometimes called type II diffusion.

Zuniga et al [28] observed a steady trench space increase in IBM APEX-E resist in a speed of 50nm/min which suggested a type II acid diffusion front. Proof of non-Fickian diffusion in APEX-E was also found by observing thickness loss versus PEB time in a top-to-top experiment. In this experiment, an unexposed resist film was put in contact

with an exposed film to allow acids to diffuse between two films and thus the thickness loss of the unexposed resist film indicated acid diffusion constant. Zuniga suggested that acid transportation should to be enhanced by reacted sites to interpret experiment results. Peterson *et al* [29] extracted diffusion parameters by interpreting the change of standing waves with acid diffusion. Postnikov *et al* [23] devised a trilayer "sandwich" of polymer films to monitor acid transport in t-BOC resist and found that acid transportation was negligible in PHOST — a fully reacted resist matrix. Stewart et al [30] continued the use of this "sandwich" experiment to explore acid diffusion in sulfonic acid. Croffie et al [31] proposed a moving boundary acid transport model based on free volume generation and polymer densification assumptions. In this model, the densified polymer matrix inhibited the diffusion of any acid trapped in the deprotected sites resulting in a moving acid diffusion front. Houle *et al* [32] proposed a method to create a high contrast photoacid profile and extracted diffusion parameters by fitting the simulation of resist reaction to FTIR measurements. In this method, a 248nm resist film was irradiated at 193nm wavelength to produce a thin acid-containing layer at the top surface due to the high absorption of 193nm wavelength. Their conclusion was that Fickian diffusion was sufficiently accurate. In reference [33], a focus-exposure matrix was used to calibrate resist parameters. Lin and his coworkers [34, 35] demonstrated the use of x-ray and neutron reflectometry as a general method to measure the spatial evolution of the reaction-diffusion process with nanometer resolution. An important observation was that the reaction front profile generated by a sharp acid profile was rather smooth. It was different from what many researchers used to believe, which was that a steep reaction profile was resulted by the enhanced non-Fickian acid diffusion thus increasing resist

contrast and rendering vertical resist sidewall angle.

Sensitive test patterns are critical to the success of quantifying and verifying acid diffusion model. Frequently used one-dimension features, such as one-dimensional critical dimension (CD) and thickness change, essentially calibrate diffusion length and cannot adequately differentiate between Fickian and non-Fickian diffusion types. Two dimensional patterns, such as standing waves [29] and line end gap [36], have been used. However, due to the lacking of physical insight of non-Fickian acid transportation, the applications of these 2D test patterns were not successful. For example, it was suggested that the enhanced non-Fickian diffusion would be more efficient for smoothing standing waves [29]. Research in chapter 4 will show that the enhanced non-Fcikian acid diffusion tends to remain standing waves.

In this dissertation, physical insight into acid transportation in Fickian and non-Fickian diffusion types will be illustrated for chemically-amplified resist (CAR) systems. According to this new insight, two diffusion-sensitive patterns for the detection of acid diffusion are proposed, which are a sequentially double exposed cross pattern and standing waves from an isolated trench. Their shapes on the wafer are highly dependent on the type of acid diffusion. By comparing the simulated shapes of these two patterns with experimental SEM measurements, a method of characterizing PEB modeling is developed to distinguish Fickian and non-Fickian diffusion and extract diffusion parameters accurately.

3.3 DEST as sensitive test pattern for resist characterization

Quantifying resist model parameters often requires matching model simulations with experiment measurements of test patterns. The sensitivity of the test pattern to resist properties largely determines the accuracy of the resist modeling. The difficulties in extracting resist parameters become even more challenging in immersion lithography where material leaching into the liquid and water uptake are possible [38, 39]. For cutting edge process control, minute process fluctuations, such as dose nonuniformity of 1% and PEB temperature variations of +/- 0.5°C, need be monitored accurately. The linewidth CD is not suitable for this purpose because CD variations upon these process fluctuations are too small to be accurately measured. More sensitive measurement techniques are needed and this study suggests the use of a double exposure technique with a slight rotation between two consecutive exposures. This produces sharp tips smaller than any diffraction limited features and is hence called double exposed sharp tip (DEST) technique.

The determination of resist parameters from SEM measurements is highly challenging. To the best of the author's knowledge, no well-established method can quantify resist surface phenomena other than interpreting the T-topping and resist footing. To examine the acid diffusion type in PEB, sequentially double exposed cross pattern and standing waves have been proposed and applied in APEX-E and UV210 resists in this dissertation. However, the very small diffusion length in some advanced CARs demands even more sensitive test patterns.

This dissertation explores the use of slightly rotated double exposed pattern to enhance by one order of magnitude the sensitivity of resist profile to resist surface interaction and diffusion phenomena [40]. The double exposure technique on which it is based on is now common in lithography. It was applied to print large marks for in-line optical characterization of imaging tools [41]. Single exposure of similar wedge-shaped openings was used for *in-situ* defocus monitoring by Izuha *et al* [42]. For resist characterization, the self-interaction of the line and space pattern on double exposure creates sharp tips that go well beyond the diffraction limit.

3.4 In-depth study of acid-equilibrium quencher (AEQ) model

Bases such as air-borne amine contaminants are critical issue for CAR systems [43]. However, if an amine is pre-formulated in CARs, then it is renamed as quencher, which helps CA resists in various respects [44~54]. While loading quencher is originally motivated to realize better environmental stability for CA resists, the quencher also renders better resist contrast [54, 55], resist resolution [49], exposure latitude [50] (EL), and line edge roughness (LER) [50, 51]. Furthermore, the quencher is frequently used to precisely control the vertical resist shape, iso-focal bias, and resist sensitivity.

Although the quencher is being used extensively in advanced CAR systems, the quencher mechanism still remains unclear. Conventional full-dissociation-quencher (FDQ) model that derives the active acid by simply subtracting the quencher amount from photo generated acid cannot explain quencher effects. Quencher diffusion and image contrast enhancement were also modeled to understand quencher effects [54, 55]. However, both

models had gained limited success and a new understanding is desired. By titration experiments using liquid model resist, quencher effects were examined [19, 20]. The pH behavior in organic solvents showed that the acid dissociation equilibrium should be considered to understand observed acid buffering effects induced by the addition of quencher. These observations motivated a new acid-equilibrium-quencher (AEQ) model that was first proposed by Nagahara [20, 21]. AEQ model assumes an existence of acid dissociation equilibrium in CA resists and the acid dissociation is buffered by adding the quencher making CAR a more robust system in a manner similar to the buffered acid.

While only preliminary evidences of AEQ model were shown for a liquid resist sample, in this dissertation, more in-depth study of AEQ model is done using real solid CA resists, where quencher effect is investigated through interpreting the evolvement of reactions as measured by a novel real-time Fourier Transform Infrared Spectroscopy (FTIR) technique [56]. The solid model CA resists used in this work consist of both a KrF acetal type resist with a diazomethane photo acid generator (PAG) (weak acid system) and an ArF ester type resist with a sulfonium salt PAG (strong acid system). A variety of resist samples with different amounts of quencher loading are irradiated and measured at various doses and bake temperatures. It is found that acid buffering effect exists in the weak acid KrF model resist but not ArF model resist.

3.5 Development of continuous line-edge roughness (LER) modeling

As device features continue to shrink, line-edge roughness (LER) consumes increasingly more error budget for critical dimension (CD). This increasing importance of LER has motivated many studies. Both numerical and analytical methods for modeling LER are highly desired to gain insight into its origins. While all current methods for modeling LER treat the post-exposure bake (PEB) and development as discrete processes, this dissertation proposes continuous models for both. This newly developed LER model is thus able to provide insights into the physical phenomena leading to LER without numerical complexity and without the need for knowledge of microscopic resist parameters.

Extensive work has been done in LER modeling and simulation. A monomer-scale LER simulator was developed [57~59], in which the post-exposure bake (PEB) was modeled by discrete acid transport and reaction events and the development process was modeled by discrete critical ionization (CI) model. The work of Pawloski *et al* [60], which applied molecular dynamics simulation to study the diffusion of developer molecules during the development of novolac resist, might be useful for the calculation of LER. Ocola *et al* [61] also simulated LER for an E-beam resist. Their model used the percolation theory of development along with the assumption that each photoacid created a small soluble volume via diffusion reactions during PEB. An issue of great concern is the impact of shot noise on LER in EUV lithography, which was simulated by Cobb *et al* [62] based upon comprehensive modeling of the statistics of photon absorption, acid generation, polymer deprotection and resist development. Preliminary results did not show any apparent increase in LER caused by exposure shot noise in EUV resist. While molecular

level simulation of the resist processes resulting in LER is an obvious choice given the length scale of LER, it is prohibitively expensive. Furthermore, the input parameters for these simulators are often unknown because it is extremely difficult to characterize resist at the microscopic level.

A small number of analytical models for LER also exist. Smith [63, 64] modeled shot noise as image fluctuation resulting from the variation of the number of photons incident upon a resist pixel. O'Brien and Mason [65] investigated shot noise induced yield loss in printing very large arrays of contact features, wherein a chip was said to fail if the dose for any contact falled outside the process window. Unfortunately, the analysis of these models depends upon the selection of the pixel size or feature size, which cannot be determined physically. A more comprehensive analytical model of shot noise and LER was developed by Gallatin and Liddle [66, 67], which incorporated the effects of acid generation, post-exposure bake and development. This model predicted the correct trend of surface roughness versus dose, but oversimplified the modeling of PEB and development. Recently, Neureuther and Pease [68] employed generating function methods to derive the statistics of reaction events as a result from a cascade of dependent sequential events of irradiation, acid generation and reaction. Their study led to a simple but meaningful analytical formula of LER as influenced by shot noise.

In the model proposed in this study, the acid creation will be modeled by two consecutive statistical processes. First, the variation on the photon number in the area of a single PAG is converted into local dose fluctuation. Second, acid generation is determined according

to a second statistical process for PAG dissociation. PEB is then modeled as partial differential equations based diffusion-reaction process. Statistical lateral dissolution model (SLDM) is proposed to model development. SLDM describes the near-edge dissolution as composed of many one-dimension lateral dissolution events simulated by Monte-Carlo method. This simple dissolution model is able to model the accumulation effect of deprotection fluctuations along the dissolution path that leads to the final line-edge position. This strategy of continuous LER modeling is applied to study the impacts of non-Fickean diffusion, shot noise and resist contrasts on LER formation. SLDM is also used to analyze large unlikely roughness event (LURE), which are large defects that occur at probabilities as low as $10^{-13} \sim 10^{-16}$ per line edge position, but can cause chip degradation or catastrophic failure.

A very important characteristic of line-edge roughness is the large correlation length ranging from 100nm to 300nm that has been seen in all KrF, ArF and EUV resists [69]. This large length scale cannot be predicted by any LER model and a new physical insight into LER origins is desired. This dissertation proposes a stress-induced crack propagation model to understand the large correlation-length scale of LER. This model assumes that stress in chemically-amplified resist will generate many microscopic cracks that act as micro dissolution channels for solvent penetration into resist film. The random crack propagation and/or merging, whose length scale is in the same order as stress, are responsible to the large scale correlation length. Stress in resist is caused by resist volume swelling and shrinkage that may happen either in PEB or in development, or both. Some references will be introduced to provide preliminary proof of this new physical LER

model. This new model will be applied to understand the influence of the flare effect on LER formation, the global scale of which has not been well explained by any LER modeling to author's knowledge.

3.6 Development of two-dimensional resist threshold model (RTM)

Lithography simulation of large scale up to full chip layouts is needed in many aspects of both optical and non-optical lithography technologies. The stringent requirement on model efficiency suitable for designs with large layouts necessitates methods capable of evaluating resist effect quickly and accurately. Rigorous resist modeling based on partial differential equations is not suitable due to the prohibitive computation cost and simplified resist models, often called compact resist models, are necessary.

Several compact models are currently available. VTR (variable threshold resist) model [70~72] that is employed extensively by commercial OPC tools assumes adaptive resist threshold as a function of parameters extracted from pre-simulated image intensities. Another often quoted method calculates critical dimension by convolution of the optical image profile with resist blur function that is often in the form of Gaussian function [73~76]. Mack *et al* proposed "lumped parameter model" that is able to determine CD as well as sidewall profile [77, 78]. Although the above compact resist models have been extensively used to predict CD, they have very limited success in the cases of two-dimension layouts.

In this dissertation, two novel compact resist models are developed to include the 2D

patterns in the prediction of feature edges. RTM-α assumes resist threshold as a function of five image properties on directions both normal and parallel to the feature edge. In RTM-β, three of five parameters are image properties on the direction normal to resist edge while the other two parameters describes the shape of resist frontier that is represented by an image contour. Both models employ a second order polynomial function to formulate resist threshold. The accuracy of RTM-α and RTM-β is verified by using extensively rigorous resist simulations (300 cases) and SEM measurements (87 cases) of two dimensional layouts printed by the use of LSI Logic 130nm technology and compared with two widely-used compact models VTU and VT5. [70~72]

3 Development of STORM-II

1. Abstract

STORM-II is a new version of resist simulation platform developed in University of California at Berkeley. Compared with the previous version of STORM, STORM-II is enhanced in both resist model and numerical algorithm. The models that are incorporated in STORM-II are simply listed in this chapter and will be illustrated in more details in following chapters. In the aspect of numerical algorithm, a finite element method that applies elemental variable elimination is used and its formulation will be described by formulating acid and quencher mutual diffusion as an example. While the previous version can only conduct two-dimensional simulation, STORM-II is extended to simulate three-dimensional profiles providing more details of resist pattern printing (Fig. 1).

2. Resist models in STORM-II

2.1 Resist model in previous STORM

The previous STORM models post-exposure bake (PEB) as a simple reaction-diffusion system as described by equation (1),

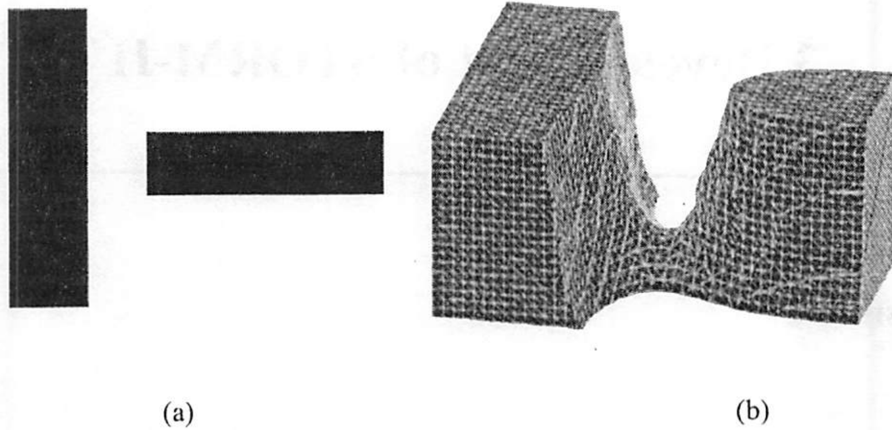

(a) (b)

Fig. 1 Example of STORM-II simulation (a) T shape pattern (top view)
(b) simulated resist profile

$$
\begin{aligned}
&\frac{\partial A}{\partial t} = K_r(1-A)H^m \\
&\frac{\partial H}{\partial t} = \nabla(D\nabla H) - K_l H \\
&H(t=0) = 1 - e^{-1.0 \cdot C \cdot Dose} \\
&D = D_0 e^{\omega A}
\end{aligned}
\qquad (1)
$$

Here A and H are deprotection and acid concentration. The parameter K_r is chemical reaction rate and the acid loss rate K_l models intrinsic acid loss. Diffusion constants D_0 and ω are able to model state dependent acid diffusion that is referred as non-Fickian diffusion or type-II diffusion and Fickian diffusion is obtained by assuming ω=0. The constant m is a fitting factor that is introduced to fit deprotection reaction for flood exposure experiments. [27]

2.2 Acid and quencher mutual diffusion model

One weakness of modeling in Section 2.1 is that quencher effect is not modeled correctly and can only be indicated by the intrinsic acid loss rate K_l. This is improved by introducing acid and quencher diffusion model,

$$\begin{aligned}
&\frac{\partial A}{\partial t} = K_r(1-A)H^m \\
&\frac{\partial H}{\partial t} = \nabla(D\nabla H) - K_n HQ - K_l H \\
&\frac{\partial Q}{\partial t} = \nabla(D_Q \nabla Q) - K_n HQ \\
&H(t=0) = 1 - e^{-1.0*C*Dose} \\
&D = D_0 e^{\omega A}
\end{aligned} \tag{2}$$

Here Q, K_n and D_Q are quencher concentration, quencher neutralization rate and quencher diffusivity respectively. In this model, acid loss due to quencher neutralization and intrinsic loss are modeled separately.

2.3 Acid-equilibrium quencher (AEQ) model

As will be discussed in chapter 6, acid-dissociation-equilibrium (AEQ) is existent in a weak-acid CAR system. AEQ modeling is described by the following equations,

$$\frac{\partial [H^+]_{active}}{\partial t} = \nabla(D_H \nabla [H^+])) - K_n[H^+][Q] + K_d[HA] - K_c[H^+][A^-] - K_{loss}[H^+]$$

$$\frac{\partial [HA]}{\partial t} = \nabla(D_{HA} \nabla [HA])) - K_n[HA][Q] - K_d[HA] + K_c[H^+][A^-] - K_{loss}[HA]$$

$$\frac{\partial [A^-]}{\partial t} = K_n[HA][Q] + K_d[HA] - K_c[H^+][A^-] - K_{loss}[H^+] \tag{3}$$

$$\frac{\partial[Q]}{\partial t} = D_Q \nabla^2 [Q] - K_n [HA][Q] - K_n [H^+][Q]$$

$$\frac{\partial[P]}{\partial t} = -K_r [H^+][P]$$

In AEQ modeling, acid consists of two parts — catalytic acid $[H^+]_{active}$ and inactive acid [HA]. $[A^-]$ is the concentration of acid conjugate base. The parameters D_H, D_{HA} and D_Q are diffusivities of catalytic acid, inactive acid and quencher molecules respectively. The parameters K_d and K_c are acid dissociation rate and recombination rates that describe the acid dissociation equilibrium and the ratio $K_a = K_d / K_c$ indicates acid strength.

2.4 Model of resist surface phenomena

Resist surface phenomena modeled in STORM-II include acid and quencher surface loss that are described by the following boundary conditions,

$$D_H \frac{\partial H}{\partial n} = K_{SH} H$$
$$D_Q \frac{\partial Q}{\partial n} = K_{SQ} Q \qquad (4)$$

The first boundary condition models the acid surface transportation using acid surface loss rate K_{SH} while the second boundary condition describes the quencher surface loss using quencher surface loss rate K_{SQ}.

3. Finite element method in STORM-II

The finite element method used in STORM-II eliminates part of variables at the

elemental level so that the size of global equation system is reduced and simulation speed can be improved. This method is illustrated by deriving finite element formulation for equations (2) and equations (4). The initial-boundary value problem is shown as following,

Differential equations:

$$\begin{aligned} \frac{\partial A}{\partial t} &= K_r(1-A)H^m \\ \frac{\partial H}{\partial t} &= \nabla(D\nabla H) - K_n HQ - K_l H \\ \frac{\partial Q}{\partial t} &= \nabla(D_Q \nabla Q) - K_n HQ \end{aligned} \tag{5.a}$$

Boundary conditions:

$$\begin{aligned} D_H \frac{\partial H}{\partial n} &= K_{SH} H \\ D_Q \frac{\partial Q}{\partial n} &= K_{SQ} Q \end{aligned} \tag{5.b}$$

Initial conditions:

$$\begin{aligned} H(t = 0\,\text{sec}) &= 1 - e^{-C*Dose} \\ Q(t = 0\,\text{sec}) &= Q_0 \\ A(t = 0\,\text{sec}) &= 0 \end{aligned} \tag{5.c}$$

3.1 Time space discretization

STORM-II applies a variable time step second-order implicit backward differentiation formula BDF2, which is the same as used in previous STORM [79]. The BDF2 formulation is derived from the fact that an arbitrary time-dependent smooth function U(t) can be described by the following formula,

$$U_{j+1} = aU_j + bU_{j-1} + ch\dot{U}_{j+1} + dh^3 \dddot{U}_{j+1}(\xi) \tag{6}$$

Here $h=t_{j+1}-t_j$ is the current time step and ξ is a time between t_j and t_{j+1}. Coefficients a, b, and c are functions of current time step h and previous time step $h_1=t_j-t_{j-1}$,

$$\begin{aligned} a &= \frac{(h+h_1)^2}{h_1^2 + 2*h*h_1} \\ b &= -\frac{h^2}{h_1^2 + 2*h*h_1} \\ c &= h + h_1 * b \end{aligned} \tag{7}$$

Substituting equation (7) into (6) gives formula of a first order derivative of U(t) at time step $j+1$,

$$\begin{aligned} \dot{U}_{j+1} &= \frac{U_{j+1} - \overline{U}}{c(h_1, h)} + error(h^2) \\ \overline{U} &= (aU_j + bU_{j-1}) \end{aligned} \tag{8}$$

Applying equation (8), time space discretization of equation system (5.a) is obtained,

$$\frac{A_{j+1} - \overline{A}}{c} = K_r(1 - A_{j+1})H_{j+1}{}^m \quad \text{(a)}$$

$$\frac{H_{j+1} - \overline{H}}{c} = \nabla(D_0 e^{\omega A_{j+1}} \nabla H_{j+1}) - K_n H_{j+1} Q_{j+1} - K_l H_{j+1} \quad \text{(b)} \tag{9}$$

$$\frac{Q_{j+1} - \overline{Q}}{c} = \nabla(D_Q \nabla Q_{j+1}) - K_n H_{j+1} Q_{j+1} \quad \text{(c)}$$

According to equation (9.a),

$$A_{j+1} = \frac{K_r H_{j+1} + \overline{A}/c}{1/c + K_r H_{j+1}} \tag{10}$$

Substituting equation (10) into (9.b) reduces the number of equations that need be assembled into the global equation system,

$$
\begin{aligned}
\frac{H_{j+1}-\overline{H}}{c} &= \nabla(D_0 e^{\omega A_{j+1}} \nabla H_{j+1}) - K_n H_{j+1} Q_{j+1} - K_l H_{j+1} \\
\frac{Q_{j+1}-\overline{Q}}{c} &= \nabla(D_Q \nabla Q_{j+1}) - K_n H_{j+1} Q_{j+1} \\
\text{where} \quad A_{j+1} &= \frac{K_r H_{j+1} + \overline{A}/c}{1/c + K_r H_{j+1}}
\end{aligned}
\tag{11}
$$

In previous STORM, all three equations in (9) are formulated by finite element method and a global equation system of *3*N* dimension is generated, where N is the total number of element nodes. In STORM-II, equation (9.a) is eliminated at the elemental level so that the size of the global equation system reduces to *2*N*. The computation speed is predicted to be improved by a factor of 2. In the resist modeling that assumes zero quencher diffusivity, the variable of quencher Q can also be eliminated. In this case, the size of the global equation system will be further reduced to N and a speed improvement by a factor of 9 is predicted.

3.2 Finite element formulation of acid and quencher mutual diffusion

In finite element method, the whole simulation domain is approximated by a summation of man small elements,

$$
\begin{aligned}
&\textit{volume} \qquad \Omega = \sum \Omega^e \\
&\textit{surface} \qquad S = \sum S^e
\end{aligned}
\tag{12}
$$

Finite element method is derived from a weak form of equations (11) within each element Ω^e,

$$\int_{\Omega^e} \delta\left(\begin{Bmatrix} H_{j+1} \\ Q_{j+1} \end{Bmatrix}\right)^T \begin{Bmatrix} \dfrac{H_{j+1}-\overline{H}}{c} \\ \dfrac{Q_{j+1}-\overline{Q}}{c} \end{Bmatrix} d\Omega -$$

$$\int_{\Omega^e} \delta\left(\begin{Bmatrix} H_{j+1} \\ Q_{j+1} \end{Bmatrix}\right)^T \begin{Bmatrix} (\nabla(D_0 e^{\omega A_{j+1}} \nabla H_{j+1}) - K_n H_{j+1} Q_{j+1} - K_l H_{j+1}) \\ \nabla(D_Q \nabla Q_{j+1}) - K_n H_{j+1} Q_{j+1} \end{Bmatrix} d\Omega = \begin{Bmatrix} 0 \\ 0 \end{Bmatrix} \tag{13}$$

where $A_{j+1} = \dfrac{K_r H_{j+1} + \overline{A}/c}{1/c + K_r H_{j+1}}$

Here $\delta\left(\begin{Bmatrix} H_{j+1} \\ Q_{j+1} \end{Bmatrix}\right)^T$ is an arbitrary variation of acid and quencher concentration.

Within each element domain, variables H and Q are interpolated by the use of shape functions,

$$\begin{Bmatrix} \mathrm{H}_{j+1} \\ \mathrm{Q}_{j+1} \end{Bmatrix} = \begin{bmatrix} \tilde{\phi} & \tilde{0} \\ \tilde{0} & \tilde{\phi} \end{bmatrix} \begin{Bmatrix} \tilde{\mathrm{H}}_{j+1} \\ \tilde{\mathrm{Q}}_{j+1} \end{Bmatrix} \tag{14}$$

Here $\begin{Bmatrix} \tilde{\mathrm{H}}_{j+1} \\ \tilde{\mathrm{Q}}_{j+1} \end{Bmatrix}$ is a vector of element nodal values and $\begin{bmatrix} \tilde{\phi} & \tilde{0} \\ \tilde{0} & \tilde{\phi} \end{bmatrix}$ is a matrix of shape functions. $\begin{Bmatrix} \tilde{\mathrm{H}}_{j+1} \\ \tilde{\mathrm{Q}}_{j+1} \end{Bmatrix}$ is an eight-dimensional vector for 2D rectangular elements and a sixteen-dimensional vector is obtained for 3D block elements.

Substituting equation (14) and (5.b) into equation (13) and then applying variable separation give the following finite element formulation,

$$\underbrace{\left(\begin{bmatrix}\tilde{M} & \tilde{0}\\ \tilde{0} & \tilde{M}\end{bmatrix}+\begin{bmatrix}\tilde{K}_{H} & \tilde{0}\\ \tilde{0} & \tilde{K}_{Q}\end{bmatrix}+\begin{bmatrix}\tilde{K}_{loss} & \tilde{0}\\ \tilde{0} & \tilde{0}\end{bmatrix}\right)\begin{Bmatrix}\tilde{H}_{j+1}\\ \tilde{Q}_{j+1}\end{Bmatrix}}_{\text{same term as in previous STORM}}+$$

$$\underbrace{\left(\begin{bmatrix}\tilde{K}_{QQ} & \tilde{0}\\ \tilde{0} & \tilde{K}_{HH}\end{bmatrix}\right)\begin{Bmatrix}\tilde{H}_{j+1}\\ \tilde{Q}_{j+1}\end{Bmatrix}}_{\text{mutual diffusion terms}}-\underbrace{\left(\begin{bmatrix}\tilde{K}_{SH} & \tilde{0}\\ \tilde{0} & \tilde{K}_{SQ}\end{bmatrix}\right)\begin{Bmatrix}\tilde{H}_{j+1}\\ \tilde{Q}_{j+1}\end{Bmatrix}}_{\text{surface loss term}}=\begin{Bmatrix}\tilde{0}\\ \tilde{0}\end{Bmatrix} \tag{15}$$

where

$$\tilde{M}=\int_{\Omega^e}\frac{1}{c}\tilde{\Phi}^T\tilde{\Phi}d\Omega$$

$$\tilde{K}_H=\int_{\Omega^e}D_0e^{\omega A}(\nabla\tilde{\Phi})^T\nabla\tilde{\Phi}d\Omega$$

$$\tilde{K}_Q=\int_{\Omega^e}D_Q(\nabla\tilde{\Phi})^T\nabla\tilde{\Phi}d\Omega$$

$$\tilde{K}_{HH}=\int_{\Omega^e}K_nH_{j+1}\tilde{\Phi}^T\tilde{\Phi}d\Omega$$

$$\tilde{K}_{QQ}=\int_{\Omega^e}K_nQ_{j+1}\tilde{\Phi}^T\tilde{\Phi}d\Omega$$

$$\tilde{K}_{loss}=\int_{\Omega^e}K_l\tilde{\Phi}^T\tilde{\Phi}d\Omega$$

$$\tilde{K}_{SH}=\int_{S^e}K_{SH}\tilde{\Phi}^T\tilde{\Phi}dS$$

$$\tilde{K}_{SQ}=\int_{S^e}K_{SQ}\tilde{\Phi}^T\tilde{\Phi}dS$$

The finite element formulation (15) generates a nonlinear system as indicated by state dependent matrices of K_H, K_{HH} and K_{QQ}.

4. Numerical performance of STORM-II

Computation efficiency of STORM and STORM-II is investigated by performing numerical simulations on a two-dimensional elbow resist pattern as depicted in Fig. 2(a)

assuming a simple resist model as given in equation (1). The domain size is 1.0μm x 1.0μm and a 40 x 40 mesh is used for finite element simulation. Computation efficiency is compared under various diffusivities and ω factors as plotted in Fig. 2(b) and Fig.2(c). In Fig. 2(b), D_0 is taken as 1E-4μm^2/s and ω varies from 1.0 to 4.0. In Fig. 2(c), ω is fixed at 2.0 while diffusivity D_0 ranges from 1E-3μm^2/s to 1E-6μm^2/s. Using STORM-II, simulation speed is improved by a factor of 2~10 and the most time reduction is obtained at low ω and low diffusivity. (All computations are done on DEC-α, CPU 700MHz)

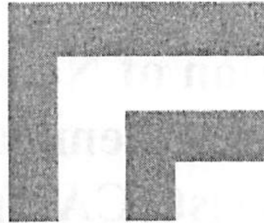

(a)

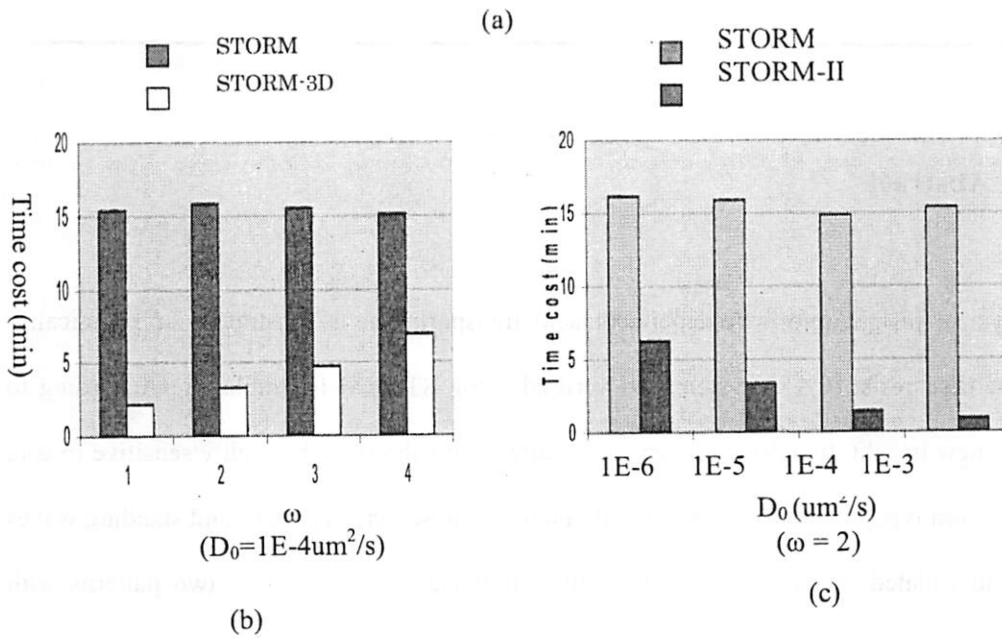

(b)

(c)

Fig.2 (a) 2D elbow resist pattern and speed comparison (b) at various diffusion constants ω (c) at various D_0

4 Characterization of Non-Fickian Acid Diffusion in DUV Chemically-amplified Resist (CAR)

1. Abstract

Physical insight into state-dependent acid transportation is illustrated for chemically-amplified resist (CAR) system and verified using STORM-II simulation. According to this new insight, two diffusion-sensitive patterns are shown to be highly sensitive to acid diffusion type, which are a sequentially double exposed cross pattern and standing waves in an isolated trench. By comparing the simulated shapes of these two patterns with experimental SEM measurements, Fickian and non-Fickian diffusion during post-exposure bake (PEB) can be distinguished. This method is successfully applied to IBM APEX-E and Shipley UV210 resists and shows that the reduced non-Fickian diffusion models both resists the best. The development thresholds in APEX-E and UV210 resists under various image slopes are systematically investigated for both one-dimensional trench and two-dimensional trench end pattern applying a programmed foreground and background double exposure to adjust the image slope. This study demonstrates that thresholds for trench end patterns are higher than that for trenches. Except for 1D

trenches in UV210, which remains a constant independent of image slope, all thresholds increase while the image slope decreases.

2. Acid diffusion sensitive features — sequentially double exposed cross pattern and standing waves

The concept of sequential double exposure as used in this study is shown in Fig 1(a). A cross pattern is printed by sequential exposure of a horizontal line and then a vertical line. Figure 1 (b) and (c) show examples of double exposed cross structure with feature sizes of 0.3um and 0.4um using Shipley UV210.

The double exposed cross structure, which is less influenced by optical diffraction, is very sensitive to acid diffusion. Due to the double exposure, the acid in the feature overlapping zone is twice as high as that in the other region and diffuses outwards during PEB. The shape of the corner in the double exposure is thus an effective means of observing acid diffusivity. Fig. 2 shows the simulations for the double exposed cross structure with and without acid diffusion. The simulation results illustrate a high sensitivity of the corner shape to the acid diffusion. This super-sensitivity of double exposed pattern to acid diffusion allows diffusion parameters to be extracted to the high degree of accuracy needed in resist profile simulation.

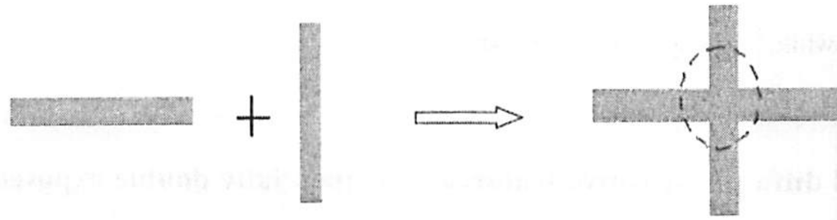

(a)

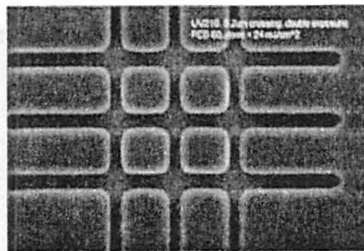

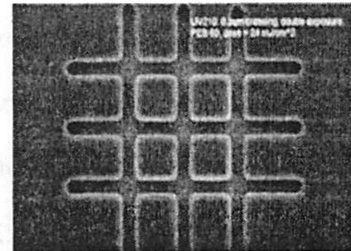

(b) (c)

Fig. 1 (a) scheme of double exposed cross pattern (b) double exposed cross pattern of 0.3um trench (UV210) (c) double exposed cross pattern of 0.4um trench (UV210)

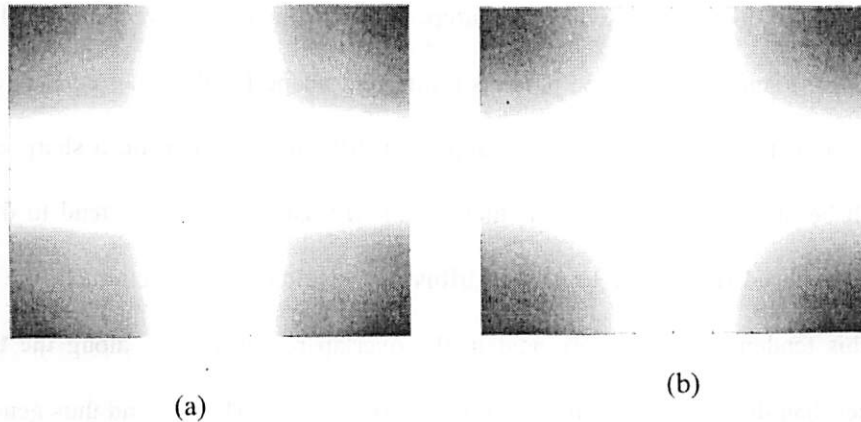

(a) (b)

Fig. 2 STORM simulation of double exposed cross pattern (a) no acid diffusion (b) with acid diffusion

More important, the double exposed cross pattern is sensitive not only to the amount of acid diffusion but also to the diffusion type. Three separate types for acid diffusion have been proposed and are investigated in this study, which are Fickian diffusion (FD), enhanced non-Fickian (ENF) and reduced non-Fickian (RNF) diffusion. In the Fickian diffusion type, the acid diffusivity remains a constant independent of deprotection reaction. In the enhanced non-Fickian diffusion type, the acid diffusivity increases due to the deprotection reaction, while it decreases in the reduced non-Fickian model. These three diffusion modes can be described by the following formula,

$$
\begin{aligned}
&D = D_0 e^{\omega A} \\
&\text{A : deprotection level} \\
&\text{D : acid diffusivity} \\
&\omega = 0, \text{Fickean diffusion} \\
&\omega > 0, \text{enhanced non - Fickean} \\
&\omega < 0, \text{reduced non - Fickean}
\end{aligned}
\tag{1}
$$

The sequentially double exposed cross pattern is particularly sensitive to the diffusion type in resist. Each diffusion type predicts a different shape for the inner corners of the overlap region. If ENF diffusion is the dominant diffusion mechanism, a sharp corner shape will be observed. The reason is that, in this diffusion type, acids tend to diffuse within the exposed region due to a high diffusivity resulted from reaction. In the cross pattern, this tendency makes more acid in the overlap region diffuse along the trench arms rather than diagonally into the unexposed corner regions (Fig. 3) and thus generates a sharp corner. If reduced non-Fickian diffusion is the case, a smooth corner shape will be observed. In this case, diffusion diagonally out of the intersection is preferred to diffusion along the arms (Fig. 3) and a smooth resist profile of the double exposed cross is produced. The Fickian diffusion type has neither preferential effect. These physical insights explained above were verified by STORM-II simulations. One quarter of a sequentially double exposed cross pattern was simulated in STORM-II assuming all three diffusion types. The deprotection profile for each diffusion type is shown in Fig.4. In the simulations, the deprotection rate and acid loss rate were 0.28 and 0.02. The acid diffusivities for the Fickian, the enhanced non-Fickian and the reduced non-Fickian diffusion cases are D_0=1E-4um^2/s, ω=0, D_0=8E-6um^2/s, ω=8 and D_0=1.5E-3um^2/s, ω=-8. The results shown in Fig. 4(a-c) verify that the shape of the cross pattern depends greatly on diffusion type. Shown in Fig. 4(d) is the SEM of a double exposed cross pattern printed in APEX-E. Comparison of this printed resist pattern with simulated deprotection profiles indicates that APEX-E has a reduced non-Fickian diffusion type. More in-depth quantitative results will be discussed in Section 3.

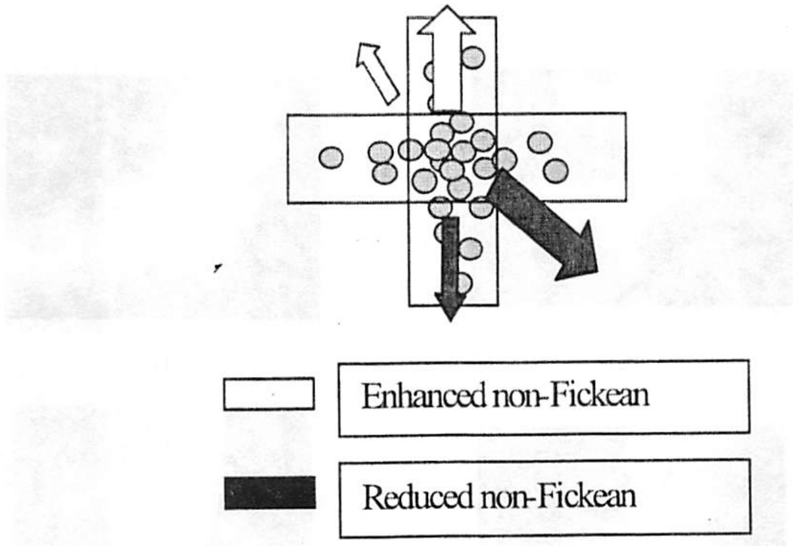

Fig. 3 Acid transportation in sequentially double exposed cross structure as predicted by ENF and RNF diffusion types

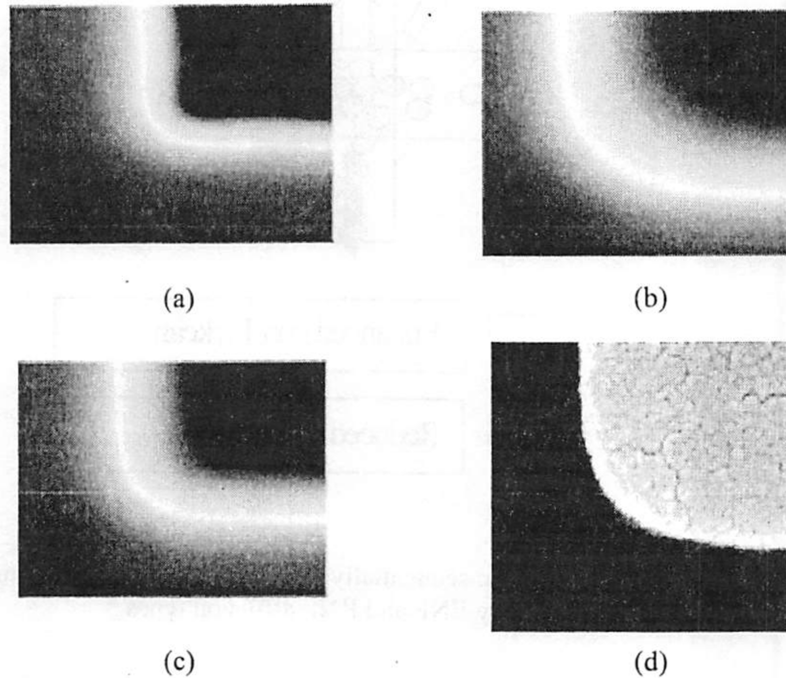

Fig. 4 Deprotection profiles of one quarter of sequentially double exposed cross pattern predicted by (a) enhanced non-Fickian mode (b) reduced non-Fickian mode (c) Fickian diffusion mode (d) SEM of the cross pattern printed in APEX-E

Standing waves are also highly sensitive to diffusion type. The same principle of acid movement as used in the sequentially double exposed cross pattern can be applied to predict the resist profile of standing waves resulted from different diffusion type. As shown in Fig. 5, the direction of diffusion for the ENF diffusion is primarily lateral tending to increase the standing waves. For the RNF diffusion, the direction of acid diffusion is more vertical tending to eliminate the destructive exposure results. The effect of Fickian diffusion will be in the middle. STORM-II simulations were made for an isolated trench printed in a 0.9um APEX-E film with no BARC giving the initial image

intensity as shown in Fig. 6(a). Figure 6 (b~d) shows the contours of the deprotection in the resist cross-section for all diffusion types. It is observed that the physical size of the standing wave is invisible for RNF diffusion, only slightly reduced for Fickian diffusion and large for ENF diffusion.

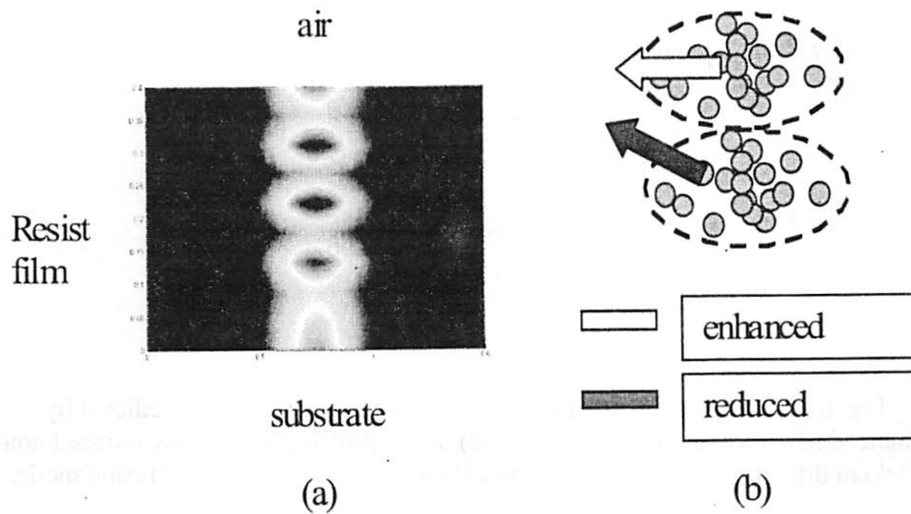

Fig. 5 (a) Image intensity of standing waves (b) Acid movement in the region of standing waves predicted by enhanced and reduced non-Fickian diffusion modes

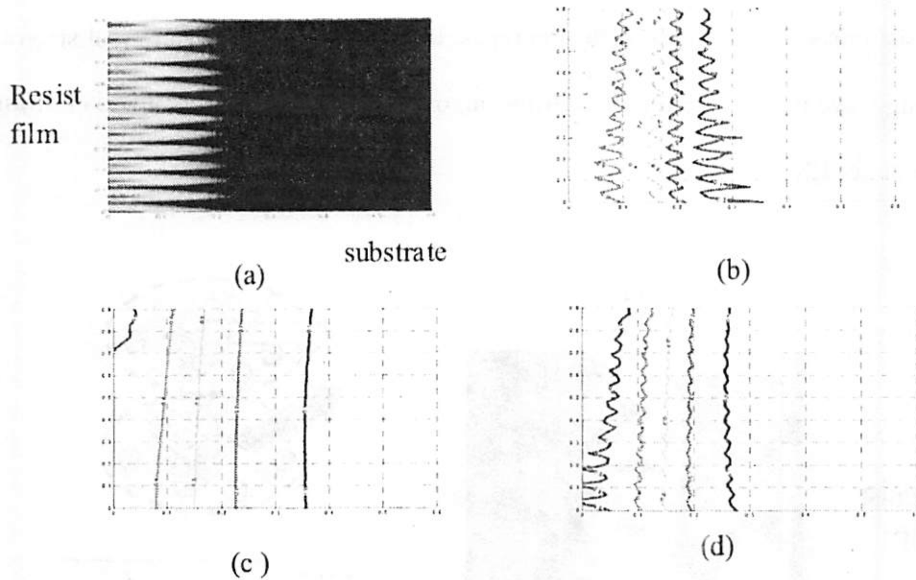

Fig. 6 (a) Image intensity of standing waves (b) resist profile predicted by enhanced non-Fickian diffusion model (c) resist profile predicted by reduced non-Fickian diffusion model (d)) resist profile predicted by Fickian diffusion model

3. Characterization of IBM APEX-E and Shipley UV210 resists based on diffusion sensitive features

Acid diffusion in APEX-E and UV210 resists is investigated in this section applying a basic PEB model as described by the following equations

$$\begin{aligned}
&\frac{\partial A}{\partial t} = K_r(1-A)H \\
&\frac{\partial H}{\partial t} = \nabla(D\nabla H) - K_l H \\
&D = D_0 e^{\alpha A}
\end{aligned} \tag{2}$$

For the development, a simple threshold model is applied as a first order approximation. For UV210, the effect of quencher loading is merged into the intrinsic acid loss as modeled by acid loss rate K_l and no equation of the quencher neutralization is required.

In the above resist model, there are five parameters to be calibrated, which can be divided into two groups according to the calibration strategy. The first group includes the reaction rate, acid loss rate and development threshold that are determined by best fitting the curve of dose-to-clear versus PEB time for flood exposure as well as the trench width. The second group is the diffusion parameter, which will be determined by interpreting the corner-to-corner spacing of the sequentially double exposed cross pattern and the visibility of standing waves.

All experiments in this chapter are conducted on an ASML tool, Model 5500/90 at a wavelength of 248nm, NA= 0.5 and σ = 0.62. Two chemically amplified resists, Shipley UV210 and IBM APEX-E, are used. Both resists are spin-coated at 3000 rpm for 30sec. The soft bake conditions for UV210 and APEX-E are 130°C, 60 seconds and 100°C, 60 seconds. The post exposure bake conditions are 130°C, 60 seconds and 90°C, 60 seconds, respectively. For APEX-E resist, a reflective top coating (RTC) is added by spinning at 3000rpm for 30 seconds and soft-baking at 100°C for 60 seconds. The development conditions are 45 sec in LDD-26W (Shipley) for UV210 and 50 sec in 0.25 N TMAH for the APEX-E. AR3-600 (Shipley) bottom antireflective coating (BARC) is applied before resist coating using the same recipe as for UV210 coating. The trenches that are used to extract the acid diffusion constants are 0.3um, 0.4um, 0.5um and 0.6um isolated trenches.

These values are 5X demagnification of mask spacing, also called designed trench width in this chapter. These trenches are also applied to generate double exposed crosses. The dose levels for APEX-E and UV210 are 10mJ/cm^2 and 29.5mJ/cm^2.

Figure 7 shows the results of dose-to-clear versus PEB time for both APEX-E and UV210 resist, from which acid loss rates of 0.015 (APEX-E) and 0.04 (UV210) are extracted. For the PEB conditions used in this study, the reaction rates estimated according to PROLITH datasheet are 0.2 (APEX-E) and 0.15 (UV210). Using these values as initial guesses, refined reaction rates based on trench width fitting are determined to be 0.3 (APEX-E) and 0.15 (UV210). In the refinement procedure, the dissolution threshold for trench width calculation is given by the following equation [80]

$$\begin{aligned} A_{Th} &= 1 - e^{K_r C} \\ C &= D_{clear} / K_l (e^{-K_l t_{PEB}} - 1) e^{-B^* t} \end{aligned} \quad (3)$$

The parameters D_{clear}, B and t are the dose-to-clear, Dill's B parameter and the thickness of resist film respectively. The term e^{-B^*t} is included because the dose at the bottom of the resist film, which determines the full clearance of the resist film, is reduced due to photon absorption through resist film. The threshold values for APEX-E and UV210 that are correspondent to the refined reaction rates are 0.3 and 0.52 respectively.

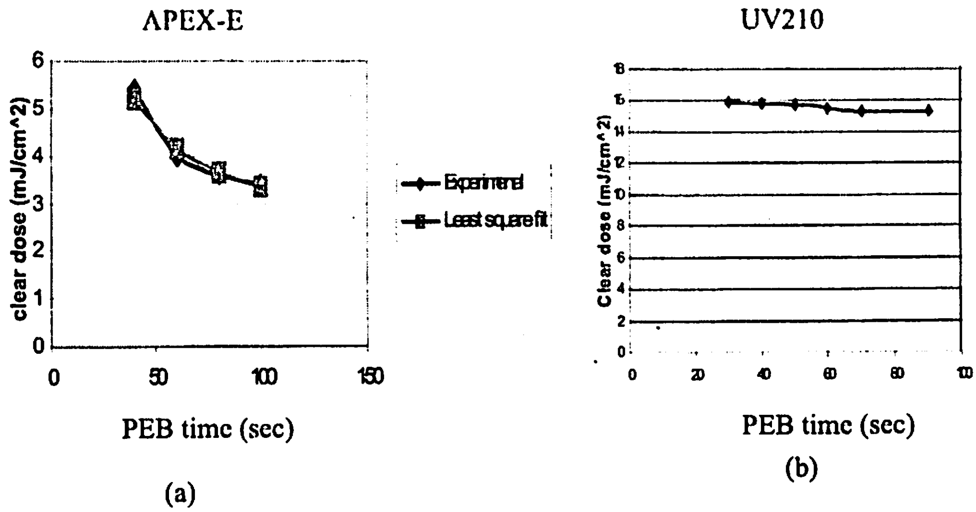

Figure 7 Dose-to-clear verse PEB time for (a) APEX-E (b) UV210

For APEX-E, all three diffusion types were simulated in STORM-II and their parameters were calibrated by fitting calculated trench widths to the experimental measurements. As shown in Fig. 8(a), if the diffusion constants D_0 and ω are well tuned, the one-dimensional trench widths can be predicted rather accurately by any diffusion type to within an error of 10nm for each. The diffusion constants for Fickian, ENF and RNF diffusions extracted from this procedure are D_0=1E-4 um^2/s, ω=0, D_0=1E-5 um^2/s, ω=5 and D_0=1E-3 um^2/s, ω=-7. Applying these extracted parameters to predict the corner-to-corner spacing differentiates diffusion type as shown in Fig. 8(b). It shows that ENF diffusion underestimates the cross spacing by about 180nm on average and does not predict the round corners as observed by SEM measurements. Although slightly improved compared with ENF, Fickian diffusion still underestimates the spacing by about 150nm. Among the three diffusion types, only RNF diffusion fits the corner-to-

corner spacing accurately and predicts round corners as are observed in SEMs. The above observations strongly indicate a reduced non-Fickian diffusion type in APEX-E resist.

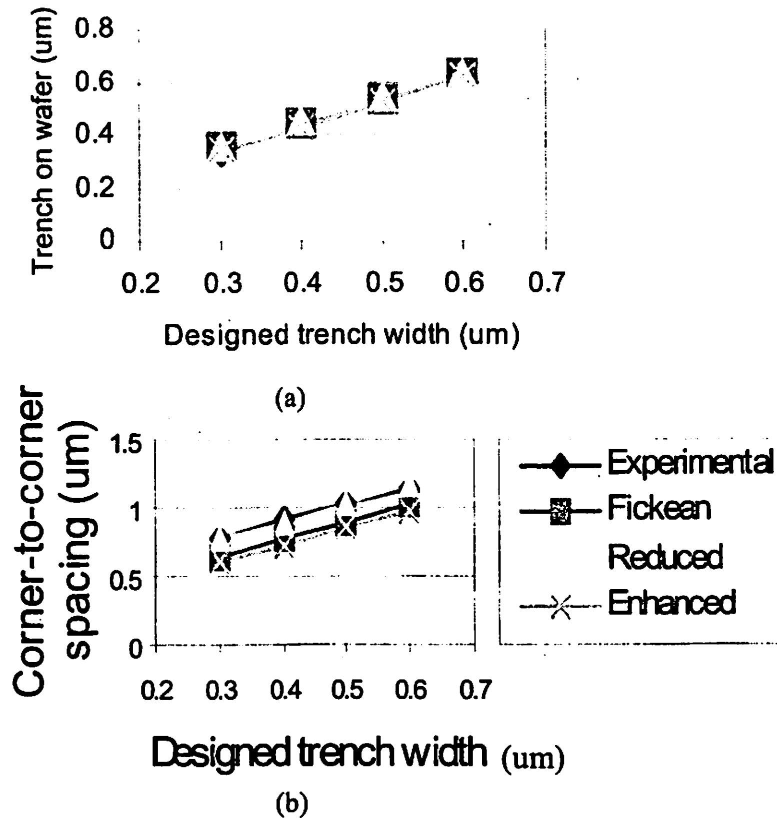

Fig. 8 Experimental measurements and simulation prediction of (a) 1D trench widths (b) the corner-to-corner spacing of sequentially double exposed cross pattern in APEX-E

A study of standing wave effects will further prove the existence of RNF diffusion in APEX-E resist. To generate standing waves, an isolated trench in a 0.9um APEX-E film without BARC was exposed. Figure 9 (a) and (b) show the contours of the deprotection concentration after 30s PEB as predicted by Fickian and RNF diffusion models. Apparently, that Fickian diffusion does not eliminate the standing wave effect while

reduced non-Fickian diffusion generates a smooth resist profile consistent with the experimental observation (Fig. 9(c)). The best fitting of both sequentially double exposed cross pattern and standing waves shows that APEX-E is best modeled by RNF diffusion with parameters D_0=1E-3 um^2/s and ω=-7.

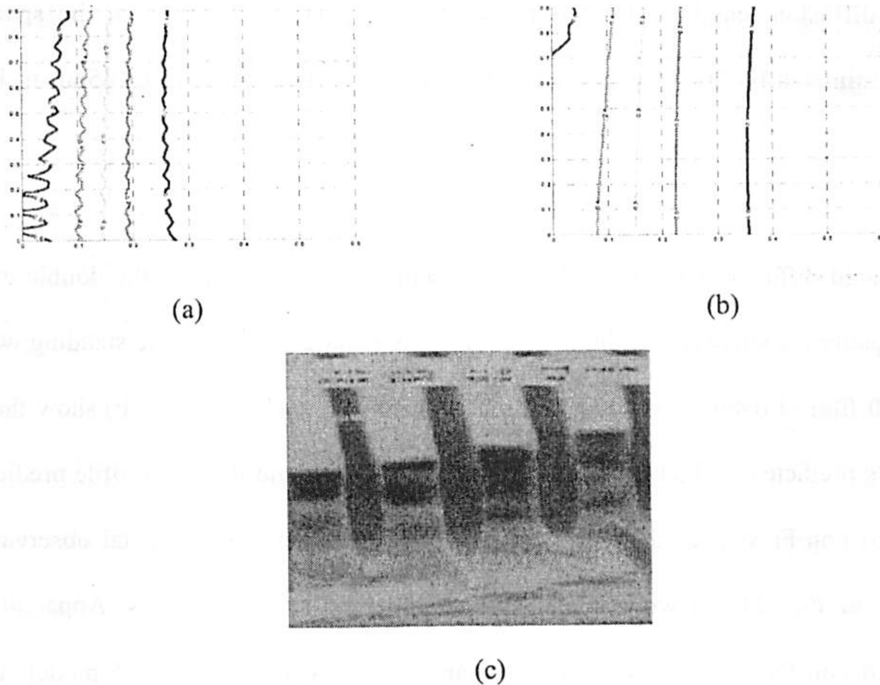

(a) (b)

(c)

Figure 9 Resist profile resulting from standing waves in APEX-E (a) predicted by Fickian diffusion model (b) predicted by reduced non-Fickian diffusion (c) SEM measurement

A similar strategy was applied to study UV210 resist. As was the case with APEX-E, one-dimensional trench widths were best fitted with all three diffusion types with appropriate diffusion constants as shown in Fig. 10 (a). The trench widths can be predicted well even assuming no diffusion. The diffusion constants extracted from trench

width fitting for Fickian and RNF diffusions are D_0=1E-4 um^2/s, ω=0 and D_0=5E-4 um^2/s, ω=-5. Using these parameters, the corner-to-corner spacing of the double exposed cross pattern was predicted and the results are shown in Fig. 10 (b). It is shown that both Fickian and RNF diffusion predict the spacing rather accurately, which is due to very small diffusion length in UV210 resist. Assuming no acid diffusion, the spacing is underestimated by 30nm, which indicates the acid diffusion length of 15nm in UV210 resist.

Since acid diffusion type in UV210 resist cannot be determined by the double exposed cross pattern, a study of standing wave effects is required. To generate standing waves, a UV210 film of 0.4um was coated on a bare wafer. Figure 11 (a) and (b) show the resist profiles predicted by Fickian and RNF diffusion. It is found that the profile predicted by reduced non-Fickian model is smooth and consistent with experimental observation as shown in Fig. 11 (c) while Fickian model predicts standing waves. Apparently, the reduced non-Fickian diffusion with constants D_0=5E-4 um^2/s and ω=-5 models UV210 resist the best.

As seen in the above experiment, the sequentially double exposed pattern is not sensitive enough to characterize small diffusion length such as in UV210 resist. In chapter 5, a double exposed sharp resist tip (DEST) technique will be shown to have higher diffusion sensitivity and is able to magnify the standing waves by one order of magnitude.

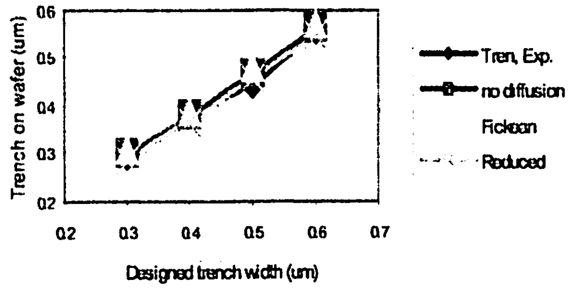

(a)

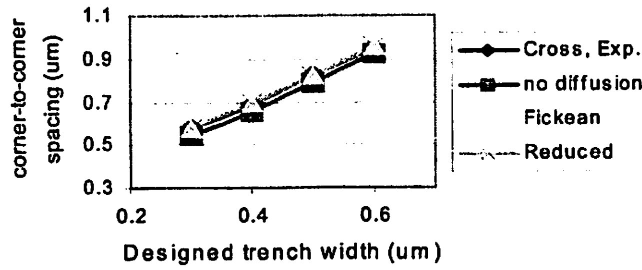

(b)

Figure 10 Experimental measurements and simulaiton predictions of (a) one-dimensional trench width (b) corner-to-corner spacing of sequentially double exposed cross pattern in UV210

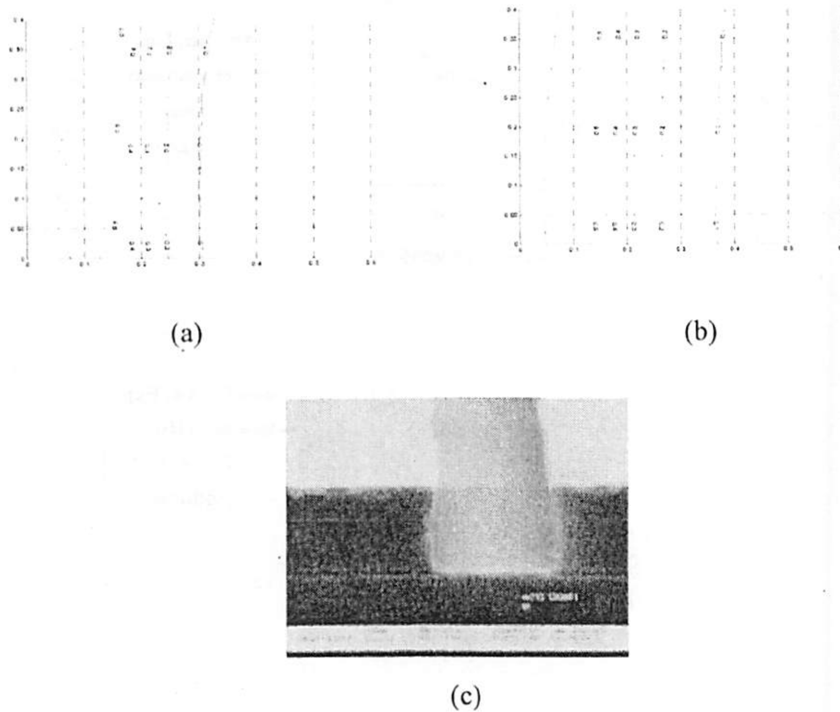

(a) (b)

(c)

Figure 11 Resist profile resulting from standing waves in UV210 (a) predicted by Fickian diffusion model (b) predicted by reduced non-Fickian diffusion (c) SEM measurement

4. Study of multi-threshold model using programmed double exposure

The technique of foreground and background double exposure consists of applying a standard exposure followed by a background exposure using a blank mask. This method is able to adjust image contrast easily as shown by Williamson [81] in studying line edge roughness. In this study, the foreground and background exposures are programmed so that the image slope is varied but the peak intensity remains constant. Using this approach, the influence of peak intensity on development threshold is excluded and the threshold will be a function of only image slope. Development threshold used in this section is not

image threshold but deprotection threshold, which means that resist volume with deprotection level higher than the threshold will dissolve and otherwise remains.

The typical image intensities of programmed double exposures for 1D trench and 2D trench end pattern are plotted in Fig. 12. For each image slope, development thresholds are extracted by fitting STORM-II simulations to experimental measurements of CDs. The resist parameters extracted in section 3 are used for STORM-II simulations. The dependency of development threshold on image slope and pattern shape is then investigated by observing results of above two patterns under various image slopes.

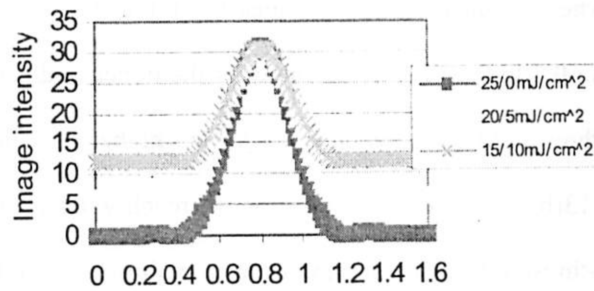

(a)

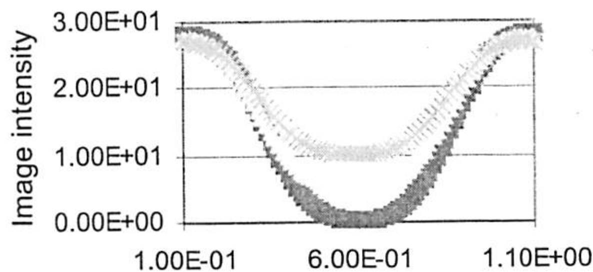

(b)

Figure 12 Image intensity of programmed foreground/background exposure of (a) trench (b) trench end gap

The series of foreground/background doses used in this experiments are 15/0 mJ/cm^2, 13.5/1.5 mJ/cm^2, 12/3 mJ/cm^2, 10.5/4.5 mJ/cm^2 for APEX-E, and 30/0 mJ/cm^2, 27.5/2.5 mJ/cm^2, 25/5 mJ/cm^2, 22.5/7.5 mJ/cm^2 for UV210. If normalized with the image slope without background exposure, the slopes for the exposure sets above are 1, 0.9, 0.8, 0.7 for APEX-E resist and 1, 0.91, 0.83, 0.75 for UV210 resist.

For APEX-E, the trenches of 0.3, 0.4, 0.5 and 0.6um are exposed to extract the thresholds for 1D trenches and 0.3/0.4um trench end pattern is used for 2D pattern. Figure 13(a) shows that when the image slope changes from 1 to 0.7, the threshold for 1D trench increases from 0.3 to 0.49 while the value for the trench end pattern increases from 0.33 to 0.54. The threshold for the trench end is always higher than that for 1D trench by about 10%. Figure 13(b) compares the prediction of trench widths using both single-threshold and multiple-threshold model. It shows that a multiple-threshold model predicts trench widths rather accurately for various image slopes while single-threshold development model fails.

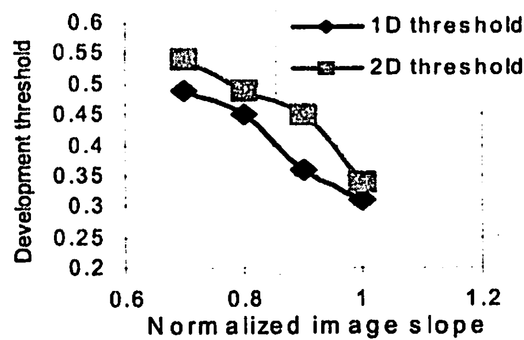

(a)

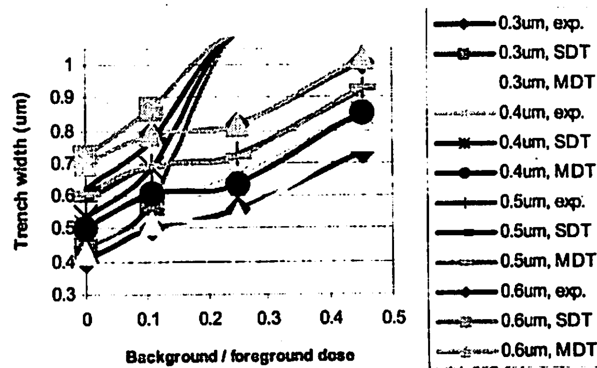

(b)

Figure 13 (a) Development thresholds of APEX-E for 1D trench and trench end pattern (b) Experimental measurements and predictions of trench widths assuming single-development threshold and multi-development threshold

Similar method is also conducted to study UV210 resist and the results are shown in Fig. 14(a). It is found that the thresholds of 1D trench are almost invariably independent of the image slope. This is probably due to the high resist contrast of UV210. Thresholds for 2D patterns are extracted using trench end patterns of 0.3/0.2um, 0.3/0.4um, 0.4/0.2um and 0.4/0.4um. For 2D patterns, correlating thresholds with deprotection slopes instead of

image slopes generates a clean linear trend as plotted in Fig. 14(b), where the threshold increases from 0.52 to 0.63 or about 20% as the deprotection slope varies from 2.7 to 0.7. For UV210 resist, multiple-threshold model is needed for 2D patterns while single threshold model is reasonably accurate for 1D trench calculation.

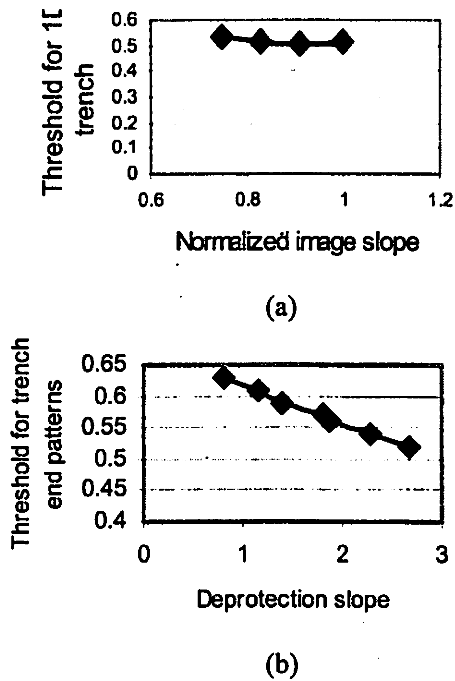

Figure 14 Development threshold of UV210 for (a) 1D trench (b) trench end patterns

5. Conclusion

The shapes of the sequentially double exposed cross pattern and standing waves are shown to be highly sensitive to the diffusion mode in CA resists. Optimal fitting of these two patterns is an effective method to determine the acid diffusion type in APEX-E and

UV210. The presence of reduced non-Fickian diffusion is found for both resists with diffusion constants D_0=1E-3 um^2/s, ω=-7 (APEX-E) and D_0=5E-4 um^2/s, ω=-5 (UV210). For UV210, this new method can detect a diffusion length as small as 15nm.

The programmed foreground and background double exposure is an easy and effective method to adjust the image slope and hence the deprotection slope. Using this technique, the dependency of development threshold on image slope or deprotection slope is studied for APEX-E and UV210. For APEX-E, the threshold for trench end patterns is higher than that for trenches by 10% on average. Both thresholds increase up to 60% when the image slope decreases by 30%. For UV210, the threshold for trenches remains a constant regardless of image slope, but the threshold for trench end patterns increases up to 20% when the deprotection slope decreases by 50%. The trend of this threshold versus the deprotection slope follows a simple linear relationship. The results above show that a multi-threshold model is required for both resists.

5 Applying Double Exposed Sharp Tip (DEST) Technique to Characterize Material Phenomena in DUV Photoresist

1. Abstract

Double exposed sharp tip (DEST) is produced by a first exposure of a line and space pattern followed by a second exposure of the same pitch with a rotation of 10 degrees. This results in long tapered fingers that cannot be made using a single exposure. The DEST tip size is on the order of the size of standing waves and can be used to examine the trade-off between resist blur and resolution. Experiments of printing DEST on a variety of substrate materials using both Shipley UV210 and IBM APEX-E resist show that DEST shape varies dramatically depending on the underlying materials. A method of characterizing resist surface phenomena based on interpreting DEST structures has been proposed and tested. STORM-II simulation studies verify the super sensitivity of DEST to non-Fickian acid diffusion and process condition fluctuations as being 10 times more than that of the critical dimension (CD) of the minimum feature size. The numerical investigations show that DEST is suitable for accurate acid diffusion calibration and process monitoring.

2. Double exposed sharp tip (DEST) technique

Double exposed sharp tip (DEST) is made by two consecutive exposures of a line and space pattern with a slight rotation as illustrated in Fig.1 (a). Sharp resist tips are produced by DEST technique as shown in Fig. 1(b), which cannot be obtained by standard single exposure. Figure 2 compares image intensities of DEST printing with a rotation of 10 degrees and single exposure of a wedge-shaped resist pattern as simulated using Panoramic. It is shown that, double exposure is able to produce sharp image tip while severe image blur is present for single exposure.

Assuming a first order kinetics as shown in Fig. 3, the latent profile formation at the DEST tip is related to the original latent formation by the factor M

$$M = \frac{\Delta DEST}{\Delta CD} = \frac{1}{\tan(\theta / 2)} \qquad (1)$$

According to Equation (1), applying a rotation of 10 degrees in DEST printing can generate sensitivity improvement of about one order of magnitude. Further numerical and experimental studies will show that the estimation based on equation (1) is fairly accurate in spite of its simplicity. It should be pointed out that this magnification factor is not due to an enhancement of the image gradient since the image gradient normal to the intersection of the wedge remains near its original value.

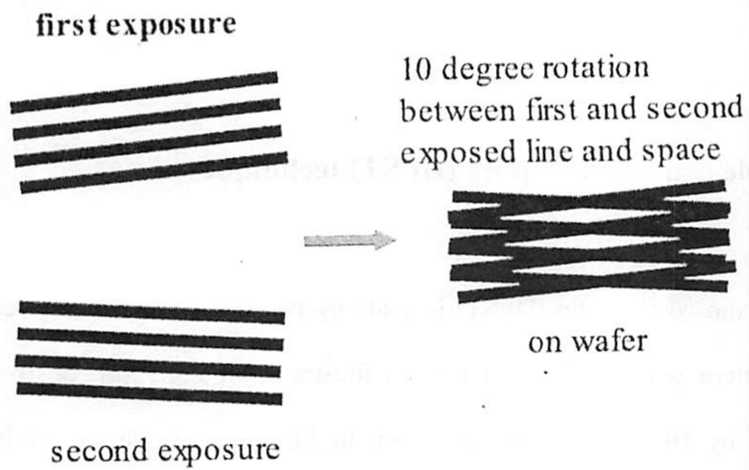

(a)

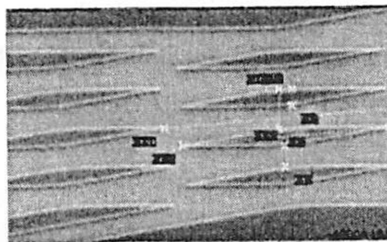

(b)

Fig.1 (a) Double exposed sharp tip technique (b) SEM of DEST wedge shape islands

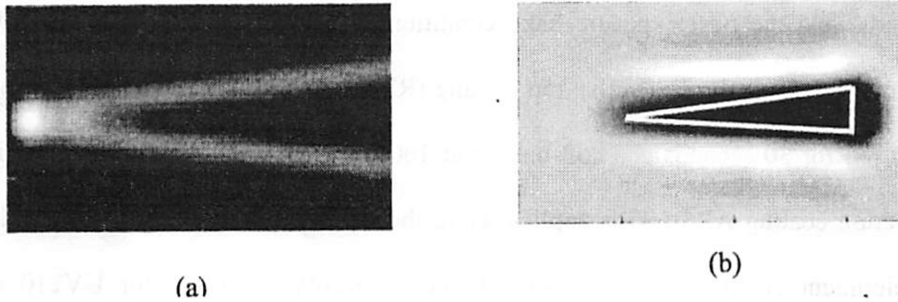

Fig. 2 Image intensity of (a) DEST technique (b) single exposed wedge shape pattern

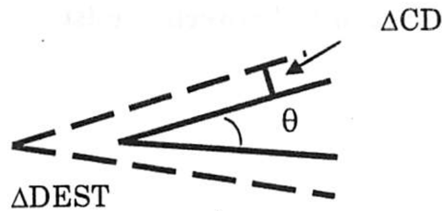

$$\Delta DEST/\Delta CD = 1.0/\tan(\theta/2.0)$$

Fig. 3 Magnification factor of DEST over CD

3. Experiment conditions

All experiments are done on an ASML tool, Model 5500/90 at the wavelength of 248nm. System parameters are NA= 0.5 and σ = 0.52. Two chemically amplified resists, Shipley UV210 and IBM APEX-E, are used. Both resists are spin-coated at 3000 rpm for 30sec. The soft bake conditions for UV210 and APEX-E are 130°C, 60 seconds and 100°C, 60

seconds, and the post exposure bake conditions are 130°C, 60 seconds and 90°C, 60 seconds, respectively. Reflective top coating (RTC) for APEX-E is added by spinning at 3000rpm for 30 seconds and soft-baking at 100°C for 60 seconds. Shipley bottom anti-reflection coating AR3-600 is applied using the same process as for UV210 resist. The development conditions are 45 seconds in LDD-26W (Shipley) for UV210 and 50 seconds in 0.25 N TMAH for the APEX-E. Silicon nitride coating is implemented by LPCVD.

4. Fundamental tradeoff between resist blur and resolution in lithography

In essence, lithography resolution is limited by blur effects that can be simply divided into two categories — optical blur and resist blur. Optical blur is caused by the projection image system acting as a low pass filter while resist blur is the consequence of material phenomena, such as acid and quencher diffusion, and limited dissolution contrast. With optical diffraction eliminated using DEST technique, the DEST tip reveals the scale of the resist blur effect. In the extreme situation of zero resist blur, an infinitely sharp DEST tip would be created.

Figure 4 (a) and (b) show DEST tips printed using APEX-E and UV210, where a 75nm radius has been observed for both resist tips. This characteristic length of 75nm indicates the scale of resist blur effect. An interesting finding is that peak-to-peak distance in

standing waves $\frac{\lambda}{2n_{resist}}$ is also close to 75nm for both resists. Although this correlation seems coincident at the first glance, it actually describes a fundamental principle of resist design — the tradeoff between resist resolution and material uniformity. On one hand, the resist blur effect sets the limit of resist resolution so that a small resist blur is preferred to push the limit of resist printing. On the other hand, the resist blur effect is critical in eliminating material nonuniformity such as standing waves and line edge roughness.

The above principle implies that a better resist resolution can be realized through two strategies. One strategy is to diminish the scale of material nonuniformity, such as applying anti-reflection coating (ARC) to reduce standing waves. The other is to enhance the smoothing efficiency of the resist blur effect so that material nonuniformity can be eliminated at small resist blur, such as acid and quencher mutual diffusion, and reduced non-Fickian diffusion.

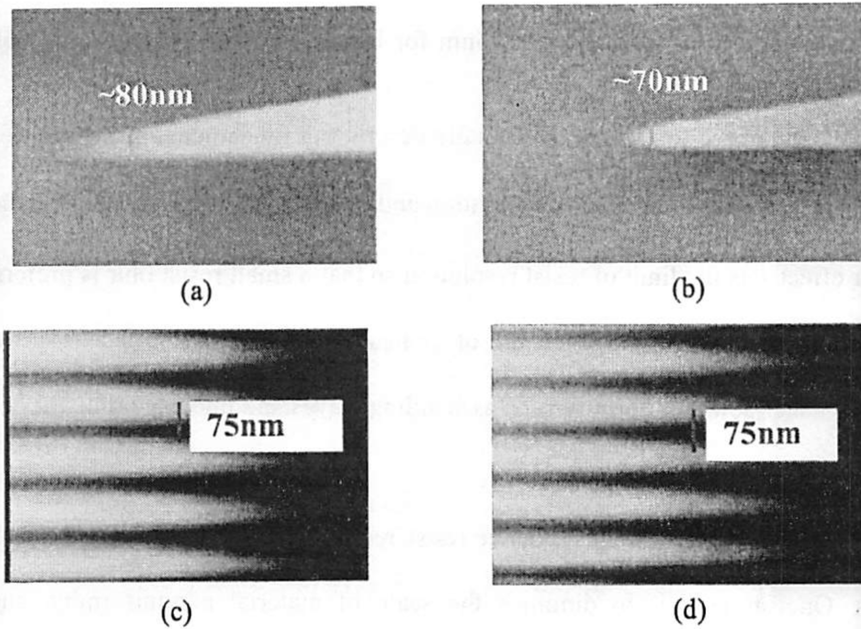

Fig. 4 (a) APEX-E DEST (b) UV210 DEST (c) Standing waves in APEX-E resist (d) Standing waves in UV210 resist

5. DEST for visualizing resist-substrate interaction

A variety of substrate materials have been used to verify DEST sensitivity to resist surface phenomena, which include bare silicon, 80A and 900A silicon nitride coatings and Shipley AR3-600 anti-reflection coating (ARC). To create the DEST pattern, a 350nm/350nm line and space pattern that is the working resolution of the exposure tool is double exposed with the irradiation energy that is best for printing a 250nm/250nm pattern.

Figure 5(a) – (d) show APEX-E DEST features on bare silicon, 80A silicon nitride, 800A

silicon nitride and AR3-600 ARC film as irradiated at doses of $5.5mJ/cm^2$, $5.5mJ/cm^2$, $8.0mJ/cm^2$ and $12.0mJ/cm^2$ respectively. RTC coating is used only for DEST printing on top of AR3-600. DEST on top of both thin and thick silicon nitride presents a long tail of about 300nm, which is not observed on top of bare silicon. A shorter DEST tail of about 100nm is found on top of the AR3-600 film. These DEST tails are believed to be caused by substrate base contamination. The AR3-600 coating does not eliminate the DEST tail completely since it is originally designed for Shipley resist rather than APEX-E. Applying the AR3-600 coating improves resist sidewall angle apparently as shown in Fig. 5(d).

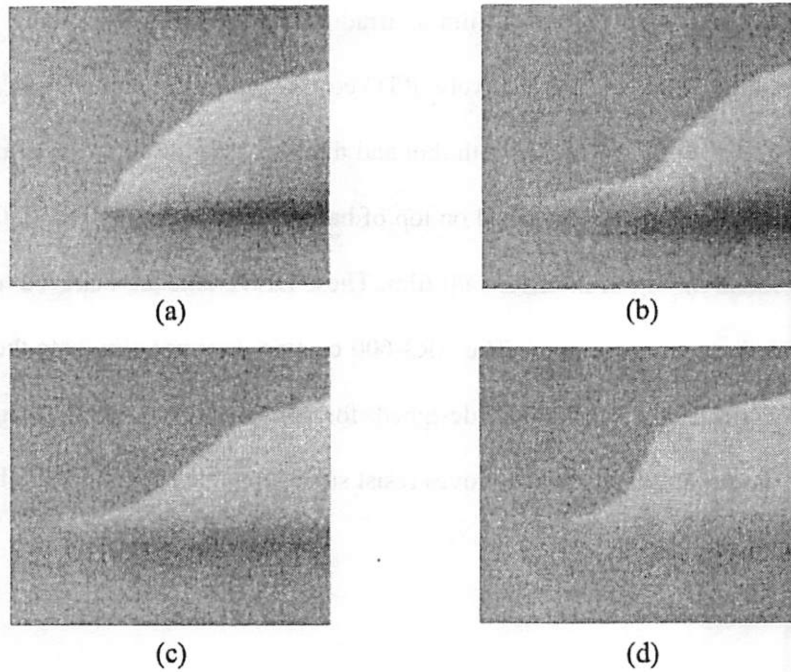

Fig.5 APEX-E DEST on (a) bare silicon (b) 80A silicon nitride (c) 900A silicon nitride (d) AR3-600 coating with RTC top coating

The same experiments are performed for UV210 on bare silicon, 80A silicon nitride and AR3-600 irradiated with doses of 17.0mJ/cm^2, 17.0mJ/cm^2 and 23.0mJ/cm^2. A 900nm UV210 film rather than optimized 420nm film is coated for a fair comparison with APEX-E resist. As a result, severe T-toppings are present and the best performance of UV210 is not demonstrated.

As shown in Fig. 6(a)–(c), the UV210 DEST shape varies dramatically while underlying materials are changed. DEST on top of bare silicon presents an interesting "aircraft

carrier" shape. On top of thin silicon nitride, a long DEST tail is observed the same as in APEX-E resist. Applying the AR3-600 coating produces a vertical resist sidewall angle.

The "aircraft carrier" shape as observed for UV210 DEST on top of bare silicon is unique, where the top resist surface appears to result from airborne base contamination and the bottom resist undercut can be explained by either aggregation of acid or loss of quencher near the substrate. In this study, quencher surface loss is assumed and will be modeled to simulate the "aircraft carrier" shape.

These experimental observations of DEST shapes over a variety of substrate materials proves that the DEST shape is super sensitive to resist surface phenomena and thus an accurate structure for visualizing resist-substrate interaction. Although all DEST experiments in this article are conducted at dry 248nm lithography, there will be no barrier to extend the DEST technique to quantify resist component leaching and water uptake for immersion lithography.

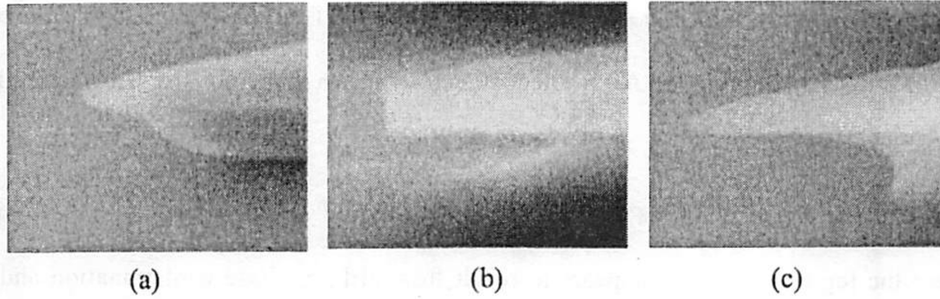

Fig.6 UV210 DEST (a) on bare silicon (b) on 80A silicon nitride (c) on AR3-600 coating

6. Modeling of resist substrate and top surface interaction

Acid and quencher mutual diffusion is modeled in STORM-II as described in the following equations,

$$\begin{aligned}
\frac{dH}{dt} &= \nabla(D_H \nabla H) - K_n QH - K_l H \\
\frac{dQ}{dt} &= D_Q \nabla^2 Q - K_n Q\, H \\
\frac{dA}{dt} &= K_r (1-A) H \\
H(t=0) &= 1 - e^{-1.0 * C * Dose}
\end{aligned} \qquad (2)$$

Here *A*, *H* and Q are normalized deprotection, photoacid and quencher concentration. The parameters K_r, K_l, K_n and *C* are deprotection reaction rate, acid loss rate, acid quencher neutralization rate and Dill's *C* parameter respectively. The parameters D_H and D_Q are acid and quencher diffusivity. The factor ω characterizes non-Fickian acid diffusion. Assumption of $D_Q = 0$, $K_n >> K_l$ and $K_n >> K_r$ simplifies the above mutual diffusion model into conventional quencher model, where active acid is obtained by simply subtracting

the quencher amount from photo generated acid.

STORM-II models T-topping and the long DEST tail by assuming acid boundary loss. The "aircraft carrier" shape is predicted by modeling quencher diffusion and surface loss. Boundary conditions are incorporated to model resist surface phenomena,

$$
\begin{aligned}
D_H \frac{dH}{dn} &= K_S H \\
D_Q \frac{dQ}{dn} &= K_{SQ} Q
\end{aligned}
\qquad (3)
$$

K_S and K_{SQ} are acid surface loss rate and quencher surface loss rate.

Figure 7(a) and (b) present APEX-E DEST on both thin and thick silicon nitride, where the same length of DEST tails indicates that the acid surface loss rate K_S is only function of substrate material. STORM-II simulations are performed using a variety of acid loss rates K_S to show the correlation between the tail length and K_S as depicted in Fig.7(c)-(e). Matching simulation results with experiment measurements of the DEST tail shows that the acid surface loss rate of APEX-E resist on top of silicon nitride is -0.0004.

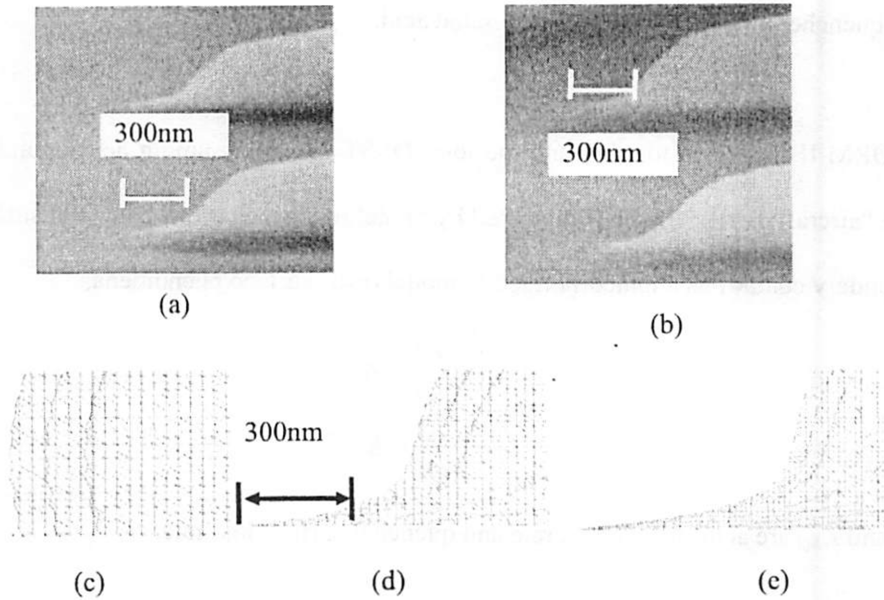

Fig.7 (a) APEX-E DEST on 80A silicon nitride (b) APEX-E DEST on 800A silicon nitride (c) DEST simulation assuming $K_S = 0$ (d) $K_S = -0.004$ (e) $K_S = -0.010$

In Fig. 8, the "aircraft carrier" shape that is found in UV210 DEST on top of bare silicon is simulated assuming quencher surface loss on the bottom in combination with base contamination on the top. STORM-II simulation uses UV210 resist parameters the same as extracted in chapter 3. Initial quencher loading and quencher diffusivity are assumed as 0.2 and 3E-4um^2/s. For boundary conditions, K_S = -0.005 and K_{SQ} = -0.010 are assumed. As shown in Fig. 8, STORM-II simulation matches the DEST profile fairly well, which verifies the effectiveness of quencher surface loss model.

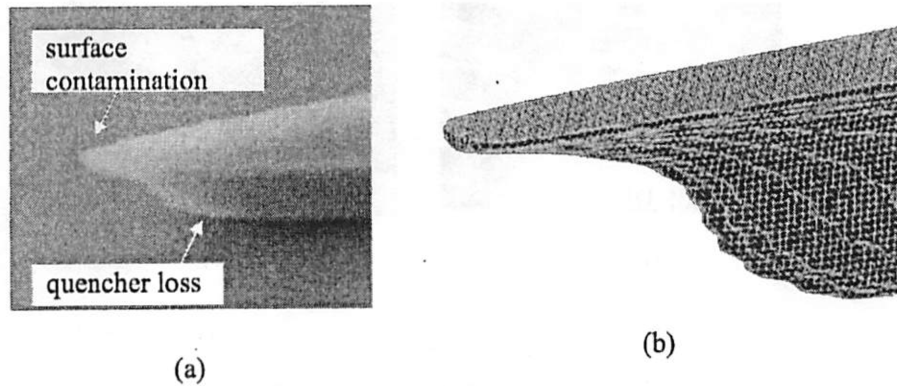

Fig.8 UV210 DEST on top of bare silicon (a) SEM (b) STORM-3D simulation

7. DEST applications in characterizing non-Fickian acid diffusion

The sensitivity of the top-down length of DEST wedge shape islands upon acid diffusivity is studied by performing STORM-II simulation and compared with the linewidth CD in Fig.9. Here APEX-E resist parameters except acid diffusivity are used and Fickian diffusion is assumed for simplicity. It is shown that the top-down length of the DEST islands presents almost 10 times better sensitivity to acid diffusion than the critical dimension.

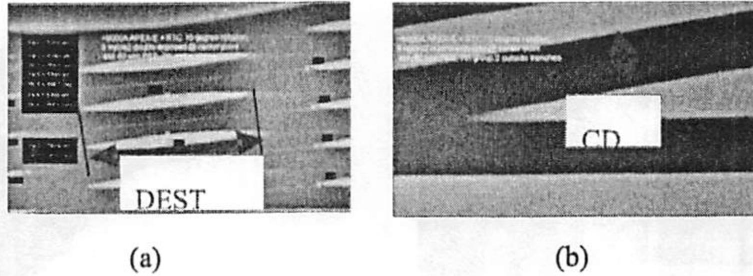

(a) (b)

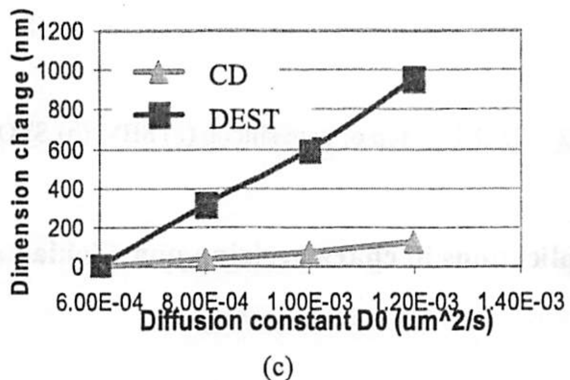

(c)

Fig.9 (a) DEST structure (b) critical dimension (c) STORM-3D simulation of dimension variation upon diffusivity

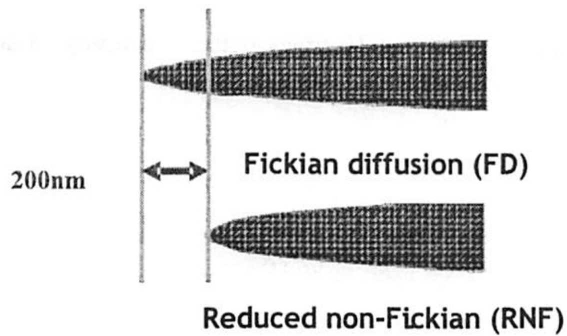

Fig. 10 Top-down wedge shape island of UV210 DEST as predicted by Fickian and reduced non-Fickian diffusions at the same diffusion length

Figure 10 shows the top-down view of UV210 DEST as generated by STORM-II simulations assuming various diffusion types. The diffusion constant used for Fickian diffusion is $D = 4E\text{-}5\ um^2/s$ while $D_0 = 5E\text{-}4\ um^2/s$ and $\omega = -5$ are assumed for non-Fickian diffusion so that both diffusion types predict the same linewidth CD. Other resist properties are taken from the UV210 resist parameters. Simulations of both diffusion types produce the same CDs that fit experiment measurements, which means that the acid diffusion type cannot be determined by interpreting only CD measurements. Even the double exposed cross pattern used in chapter 3 was not able to show much difference for the UV210 resist due to small diffusion length [37]. Here with DEST, the top-down tip to tip length of the wedge shaped island shows a 400nm difference for Fickian and RNF diffusion types and thus can be used to determine diffusion type in CAR systems.

Previous study shows that the diffusion type can be distinguished by observing the standing wave patterns. This is shown in Fig. 11. STORM-II simulations of the DEST profiles in Fig. 12 show that the DEST pattern also amplifies the ability of observing standing waves by one order of magnitude. For example, a 5nm ripple in UV210 isoline becomes a 50nm ripple in the DEST profile. For the same diffusion effect on a 2D isoline feature, the DEST profile is much smoother with reduced non-Fickian diffusion. The smooth UV210 DEST profile on top of bare silicon as measured by SEM is thus a strong evidence of RNF in the UV210.

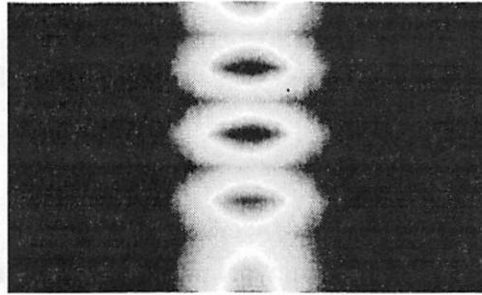

(a)

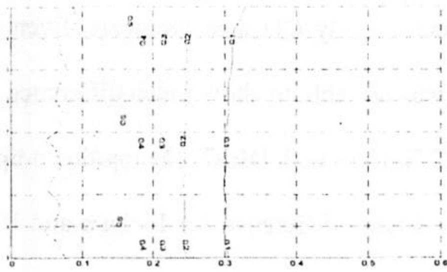

(b)

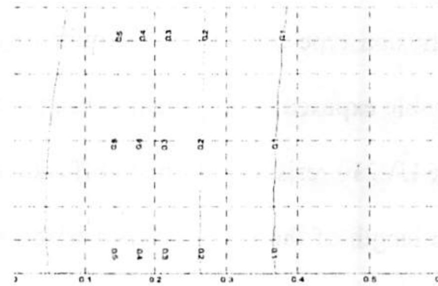

(c)

Fig.11 (a) standing wave on iso space (b) STORM simulation of deprotection contour assuming Fickian diffusion (c) STORM simulation of deprotection contour assuming reduced non-Fickian diffusion

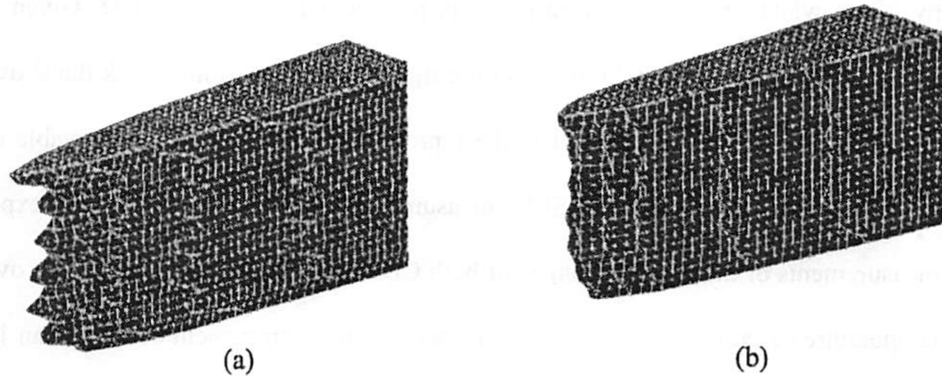

Fig.12 Standing wave effect on the DEST profile as predicted by assuming (a) Fickian diffusion (b) Reduced non-Fickian diffusion

8. DEST applications as an accurate process monitor

The DEST process amplifies the effects of parameter variations and thus is very suitable for monitoring process condition fluctuation. Figure 13 depicts the dimension changes of both linewidth CD and the top-down wedge shape DEST islands under small perturbations of process conditions predicted by STORM-3D simulation. UV210 resist parameters are used in the simulations and 30mJ/cm^2 dose and 130°C PEB temperature are assumed to be standard process conditions. As shown in Fig. 13(a) and 13(b), the length changes of the top-down wedge-shaped DEST islands are more than 15 times larger than the CD changes at the same process perturbation. At 1% dose perturbation, simulations predict a CD change of 1.5nm in comparison with a 29nm change for the DEST islands. At 0.25°C bake temperature variation, the length of DEST islands changes

by 37nm while only a 2.3nm variation is predicted for linewidth CD. Given a SEM measurement resolution of 2.0 nm, monitoring the CD alone cannot track the above small process condition fluctuations. The DEST process clearly raises the observable changes well above the 2nm noise in SEM measurements. Figure 14 shows the experiment measurements of dimension changes of both CD and DEST for APEX-E resist over PEB temperature variation up to +/-1°C. Again, sensitivity improvement of more than 10 times by using DEST technique is verified. The experimental data not falling in a straight line indicates the issue of process control quality.

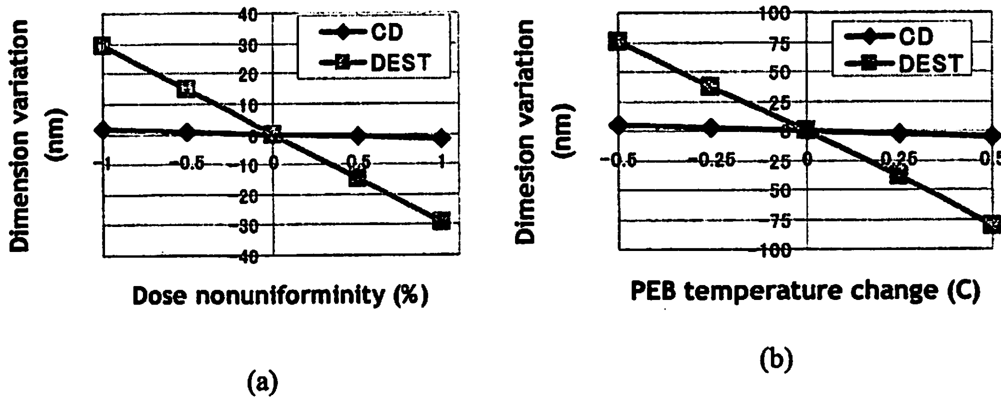

Fig. 13 Dimension changes of CD and DEST islands for UV210 resist upon (a) dose nonuniformity (b) PEB temperature variation

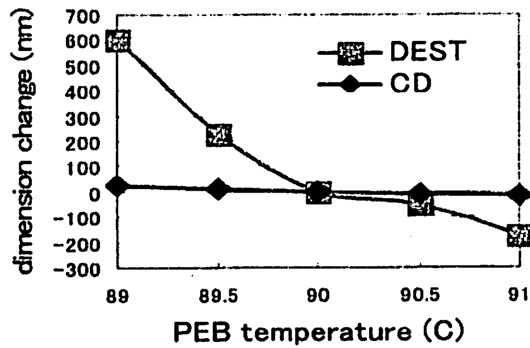

Fig. 14 Measurements of dimension changes of CD and DEST for APEX-E resist over PEB temperature variation

9. Conclusions

Double exposed sharp tip (DEST) has been printed using both APEX-E and UV210 resists. DEST tip size, the smallest printable resist feature, reveals the scale of resist blur, which is about 75nm for both resists. The finding that the scale of resist blurs is the same as that of standing waves is an evidence of a tradeoff between resolution and uniformity in chemically-amplified resist system. Several resist phenomena, including standing wave reduction via applying anti-reflection coating and acid/quencher mutual diffusion, are reconsidered from the viewpoint of the tradeoff between resist resolution and uniformity.

Various DEST resist profile shapes, including long tails and "aircraft carrier" undercut, are observed when varying the substrate material. The super sensitivity of the DEST shape to resist surface events enables accurate observation and characterization of resist

surface phenomena as verified by using APEX-E and UV210 resists. The "aircraft carrier" shape undercut in UV210 DEST on top of bare silicon implies either aggregation of acid or loss of quencher on the substrate. The "aircraft carrier" shape has been predicted by assuming quencher diffusion and surface loss. Further study is still necessary to gain in-depth physical insight into this interesting DEST shape.

Numerical studies show that the top-down length of DEST wedge-shaped islands is a strong function of both the acid diffusion length and the diffusion type. These DEST structures can be used to characterize non-Fickian diffusion in CAR systems. Furthermore, DEST exaggerates the scale of standing wave effects by a factor of 10 and is thus good for determining acid diffusion type. Only the reduced non-Fickian diffusion model can predict the disappearance of standing waves in the UV210 DEST profile. This is also strong evidence of the existence of RNF in UV210 resist. Both numerical and experimental studies show that the length of the DEST islands is more than 10 times more sensitive to process condition fluctuations than linewidth CDs and therefore DEST is good for accurate process monitor demanded by stringent process control for the leading lithography technology.

6 Understanding Quencher Mechanism by Considering Photoacid Dissociation Equilibrium in Chemically-amplified Resist (CAR)

1. Abstract

In this chapter, an in-depth study of a new acid-equilibrium-quencher (AEQ) model is conducted. AEQ model was first proposed by Dr. Nagahara [19, 20, 21] to explain quencher effects and verified using a liquid model resist. This study further investigates AEQ model using solid model CA resist systems through interpreting reaction kinetics during post-exposure bake (PEB). The model resists used in this work consist of both a KrF acetal type resist with weak photoacid generator (PAG) and an ArF ester-type resist with strong photoacid generator. The reaction kinetics in model resists is measured by employing a real-time Fourier-Transform-Infrared Spectroscopy (FTIR) during PEB. For the weak acid system, the AEQ model correctly predicts the deprotection-reaction kinetics over a variety of quencher loadings and exposure conditions with only one set of resist parameters while conventional fully-dissociation-quencher (FDQ) model cannot fit the deprotection reaction to any extent. This result provides a strong evidence of the

existence of quencher induced acid buffering in a weak-acid resist system. Different from the KrF model resist, for ArF resist, the conventional FDQ model appropriately predicts the deprotection reaction fairly well, which means that the conventional FDQ model is accurate enough to describe the strong acid system. The new AEQ model is incorporated into STORM-II and some examples of quencher effects are simulated.

2. Concepts of full-dissociation-quencher (FDQ) model and acid-equilibrium-quencher (AEQ) model

In the conventional quencher model called "Full-Dissociation-Quencher (FDQ) model" in this chapter, PAG generates the photoacid $[HA]_{generated}$ upon UV irradiation,

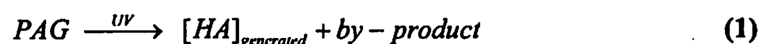

$$PAG \xrightarrow{UV} [HA]_{generated} + by-product \quad (1)$$

The photo generated acid is assumed to be strong enough to result in a full dissociation (reaction 2).

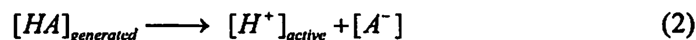

$$[HA]_{generated} \longrightarrow [H^+]_{active} + [A^-] \quad (2)$$

Here $[H]^+_{active}$ represents "catalytic" acid that catalyzes the deprotection reaction during PEB. $[A]^-$ in reaction 2 represents the conjugate base of the acid.

In FDQ model, one part of $[H]^+_{active}$ is neutralized by quencher (Q) through reaction 3 and loses the catalytic ability and all deprotection reaction is catalyzed by the remaining acids after neutralization reaction.

$$[H^+]_{active} + [Q] \rightarrow [H^+Q] \quad (3)$$

Recently, some researchers [53, 54] consider the transient FDQ to understand quencher effects, which suggests that the deprotection reaction starts even before neutralization reaction (3) is completed and the quenched acid also contributes to deprotection to some extent. FDQ model in this study includes this type of transient models.

Although straightforward, the FDQ model cannot explain some common quencher effects such as that adding quencher improves environmental stability of resist. Therefore, new chemistry phenomena should be investigated and the FDQ model be revisited. One questionable assumption in the FDQ model is that photoacid acts as strong acid in resist matrix and full acid dissociation occurs. However, it may not be true because the acid strength sometimes decreases dramatically in organic solvents such as resist matrix even it is super strong in water. The acid strength in solid resists must be investigated carefully.

The acid strength is often described by constants K_a or pK_a. In an acid-dissociation-equilibrium system as described in equation (4), the constant K_a is defined by formula (5), where Ka and K_c are the acid dissociation-reaction rate and combination-reaction rate.

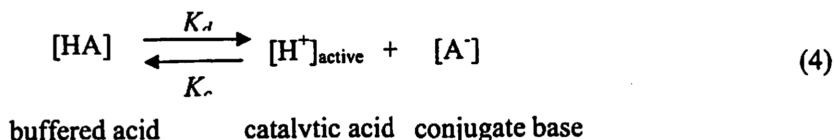

$$[HA] \underset{K_c}{\overset{K_d}{\rightleftharpoons}} [H^+]_{active} + [A^-] \quad (4)$$

buffered acid catalvtic acid conjugate base

$$K_a = \frac{K_d}{K_c} = \frac{[H^+]_{active}[A^-]}{[HA]} \quad (5)$$

The constant pK_a is defined in formula (6), where lower pK_a value means stronger acid

and the pK_a value of pure water is 7.0.

$$pK_a = -\log_{10} K_a \tag{6}$$

Figure 1 shows the pK_a range of fluorinated-super-strong acid and non-fluorinated acid. It shows that the pK_a is much higher in non-aqueous solvents than in the water. This observation implies that even a very strong acid in water can behave as a weak acid in organic matrices. Even for the super strong fluorinated acid, acid strength becomes much weaker in organic solvents and pK_a can turn into positive as shown in Fig.1. In the case of the non-fluorinated sulfonic acid, the acid acts as strong acid in water but becomes weak in organic solvents. Surprisingly, the change in acid-dissociation constants due to the matrix can be as much as more than 10 orders of magnitude. This observation indicates that the assumption of strong acid in resist matrix is not necessarily correct and a more general model that describes the partial acid dissociation need be developed to understand quencher effects.

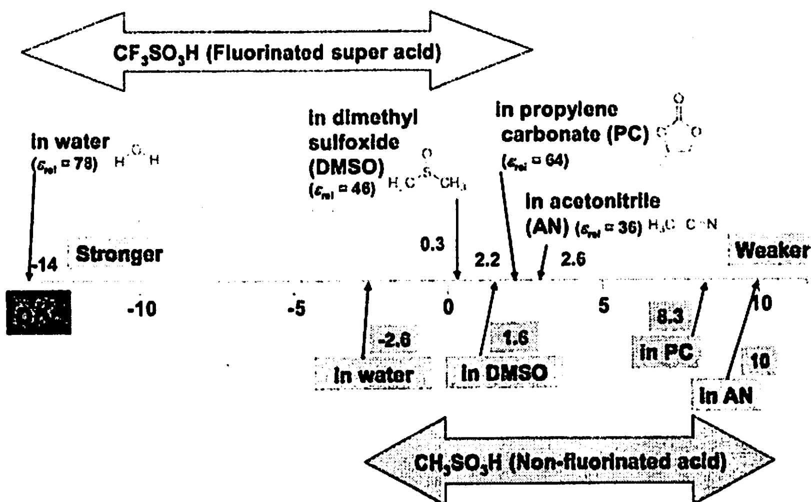

Fig. 1 K_a range of fluorinated-super acid and non-fluorinated weaker acid. Acid becomes weaker in non-aqueous matrices

To include the partial dissociation equilibrium, an acid-equilibrium-quencher (AEQ) model has been proposed by Dr. Nagahara and verified in liquid model resist. In this AEQ model, a neutralization reaction (7) occurs between [HA] and [Q] at first that generates the conjugate base of acid $[A]^-$ (an anion of acid). The reverse reaction in reaction (7) is neglected because the pK_a of the quencher is usually much higher than the acid pK_a.

$$[HA]+[Q] \rightarrow [\mathrm{QH}^+]+[A^-] \qquad (7)$$

The resulted conjugate base $[A]^-$ then pushes the dissociation equilibrium in reaction (4) to the left direction generating buffered acids. Obviously, more quencher loading would produce more buffered acids. This coupling effect of the reactions (4) and (7) is called the "common-ion effect" [82], through which buffered acids are generated by adding

quencher thus providing a more stable resist system. The buffered acid can suppress the change of catalytic $[H^+]_{active}$ due to the consumption of the acid such as by external base contamination. This system is analogous to the pH buffer solution [82] that also consists of a weak acid and a conjugate base of the acid.

3. Experimental preparation

3.1 Resist materials

Two model resists are formulated for the purpose of quencher study. One is an acetal-type KrF resist formulated with diazomethane photoacid generator (PAG) (weak acid generator) as shown in Fig. 2. The other is the ArF resist with sulfonium-salt PAG (strong acid generator) as shown in Fig. 3. In the resist samples, different quencher loadings are applied (0, 10, 25, 40, 60 mol% to PAG mol %).

KrF Resin

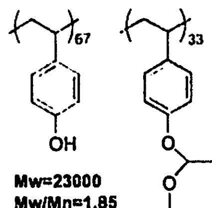

Hydroxystyrene/
Ethylvinylether-hydroxystyrene
Co-polymer

PAG

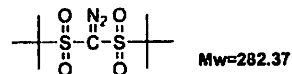

Bis(*t*-butylsulfonyl)diazomethane
Contents: 6 wt% vs. Resin

Quencher

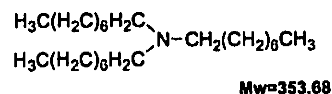

Tri(*n*-octyl)amine
Contents:
0, 0.75, 1.89, 3.0, 4.5 wt% vs. Resin
(0, 10, 25, 40, 60 mol% vs. PAG)

Solvent

PGMEA

Fig. 2 KrF resist (non-fluorinated-weak-photoacid system)

ArF Resin

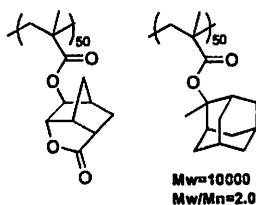

2-Methyl-adamanthyl-2-methacryrate
/2,6-norbornenecarbolactone-5-
methacrylate copolymer

PAG

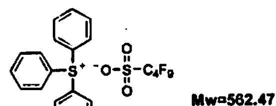

Triphenylsulfonium
nonafluorobutanesulfonate
Contents: 6 wt% vs. Resin

Quencher

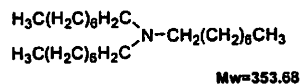

Tri(*n*-octyl)amine
Contents:
0, 0.75, 1.89, 3.0, 4.5 wt% vs. Resin
(0, 10, 25, 40, 60 mol% vs. PAG)

Solvent

PGMEA

Fig. 3 ArF resist (fluorinated-strong-photoacid system)

3.2 Real-time FTIR measurement of reaction kinetics

The *in-situ* FTIR measurement of reaction kinetics during PEB was done with the Litho Tech Japan (LTJ)'s PAGA-100 FTIR system that used Bio-Rad's FTIR spectrometer (Fig. 4) [83].

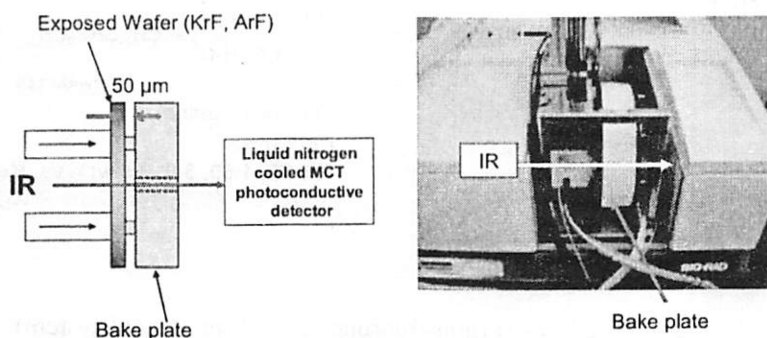

Fig. 4 Real time PEB FTIR measurement system

In this FTIR system, the infrared light passes through a 10-mm-diameter hole that is opened in the center of the PEB hot plate. N_2 is pursed through the optical path to eliminate the effect of CO_2. As a FTIR detector, a newly improved liquid-nitrogen-cooled MCT (Mercury Cadmium Telluride) photoconductive detector was installed and used.

The resist samples were coated on the low-crystal-defect wafers with 500nm thickness without using bottom antireflective coating (BARC) and were irradiated with either KrF or ArF UV light source. The FTIR spectra were recorded along with PEB process in a real time manner.

One example of FTIR spectra measuring reaction kinetics in the KrF model resist (Fig. 5) is presented in Fig. 6. The peaks that are attributed to the protection groups are at $944cm^{-1}$, $1050cm^{-1}$ and $1119cm^{-1}$, all of which show the same decay behavior (inset of Fig. 6) after normalization. In this study, the peak at 944 cm^{-1} is used for reaction measurements because it is less "polluted" by neighborhood peaks and thus has higher signal-to-noise ratio.

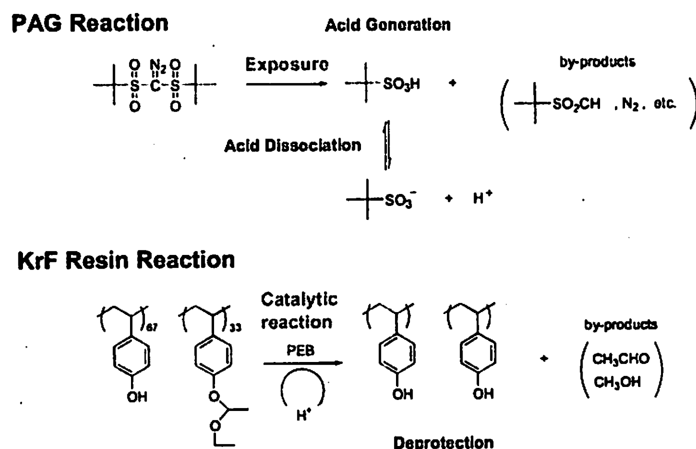

Fig. 5 The reactions in model KrF model resist

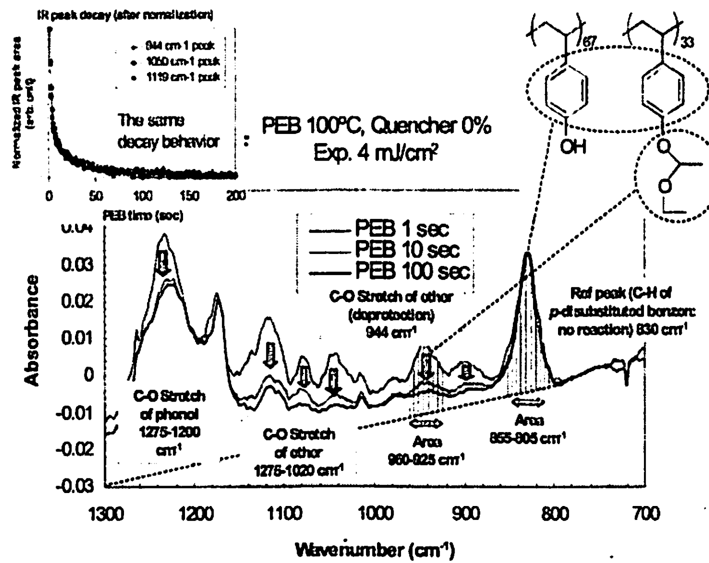

Fig. 6 FTIR Spectra for KrF model resist.

Figure 8 shows one example of FTIR spectra that measures the reaction kinetics in the ArF model resist as described in Fig. 7, where the peak at 1101 cm^{-1} is attributed to the ester-protection group.

PAG Reaction

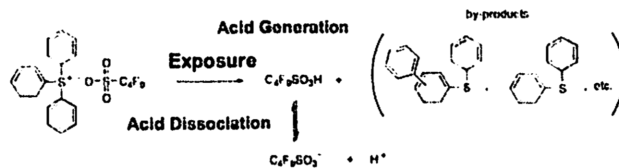

ArF Resin Reaction

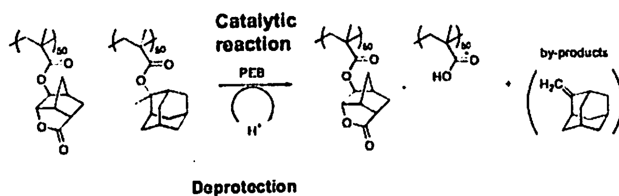

Fig. 7 The reactions in model ArF resist

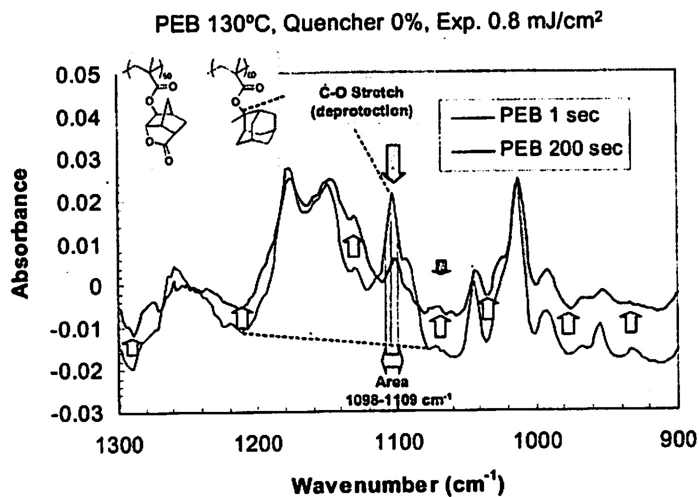

Fig. 8 FTIR Spectra for model ArF resist.

4. AEQ modeling in STORM-II

AEQ modeling in STORM-II applies Dill's model for photoacid generation,

$$[\mathrm{HA}]_{generated} = [\mathrm{PAG}]_0(1-\exp(-CE)) \tag{8}$$

The evolvement of $[H^+]_{active}$ with PEB time is consequence of a variety of processes including acid diffusion, acid neutralization, [HA] dissociation, recombination and intrinsic loss, all of which lead to equation (9). The kinetics of HA and conjugate base $[A^-]$ are described by equation (9) and (10). Equations (11) and (12) model the development of quencher and protection concentration with PEB time.

$$\frac{\partial[H^+]_{active}}{\partial t} = \nabla(D_H\nabla[H^+])) - K_n[H^+][Q] + K_d[HA] - K_c[H^+][A^-] - K_{loss1}[H^+] \tag{9}$$

$$\frac{\partial[HA]}{\partial t} = \nabla(D_{HA}\nabla[HA])) - K_n[HA][Q] - K_d[HA] + K_c[H^+][A^-] - K_{loss2}[HA] \tag{10}$$

$$\frac{\partial[A^-]}{\partial t} = \nabla(D_A\nabla([A^-])) + K_n[HA][Q] + K_d[HA] - K_c[H^+][A^-] - K_{loss3}[A^-] \tag{11}$$

$$\frac{\partial[Q]}{\partial t} = D_Q\nabla^2[Q] - K_n[HA][Q] - K_n[H^+][Q] - K_{loss4}[Q] \tag{12}$$

$$\frac{\partial[P]}{\partial t} = -K_r[H^+][P] \tag{13}$$

Although comprehensive, the above AEQ model is too complex for practical applications and model simplification is necessary. Some assumptions are proposed in this study to simplify AEQ modeling. Firstly, the diffusivities of $[H^+]_{active}$ and [HA] are assumed to be identical and the diffusion of conjugate base $[A^-]$ is negligible. Secondly, the intrinsic acid loss rates of $[H^+]_{active}$ and [HA] are identical. Thirdly, no intrinsic quencher loss occurs. At last, the dissociated photoacid $[H^+]_{active}$ and $[A]^-$ always loss in pairs, which means that $K_{loss1}*[H^+]_{active}$ in equation (9) is equal to $K_{loss3}*[A]^-$ in equation (11). Applying above assumptions generates the AEQ model used by STORM-II

$$\frac{\partial[H^+]_{active}}{\partial t} = \nabla(D_H\nabla[H^+])) - K_n[H^+][Q] + K_d[HA] - K_c[H^+][A^-] - K_{loss}[H^+] \quad (14)$$

$$\frac{\partial[HA]}{\partial t} = \nabla(D_{HA}\nabla[HA])) - K_n[HA][Q] - K_d[HA] + K_c[H^+][A^-] - K_{loss}[HA] \quad (15)$$

$$\frac{\partial[A^-]}{\partial t} = K_n[HA][Q] + K_d[HA] - K_c[H^+][A^-] - K_{loss}[H^+] \quad (16)$$

$$\frac{\partial[Q]}{\partial t} = D_Q\nabla^2[Q] - K_n[HA][Q] - K_n[H^+][Q] \quad (17)$$

$$\frac{\partial[P]}{\partial t} = -K_r[H^+][P] \quad (18)$$

5. Experimental verification of FDQ and AEQ

5.1 Modeling reaction kinetics for KrF model resist

Data points in Fig. 9 record the decay behaviors of the acetal protection group in the KrF model resist with five different quencher loadings at PEB temperature 90^0C. Each plot contains results generated by three different exposure doses, which are 0.5×, 1× and 2× best dose E_0. Here best dose is defined the exposure dose that prints the smallest CD the best.

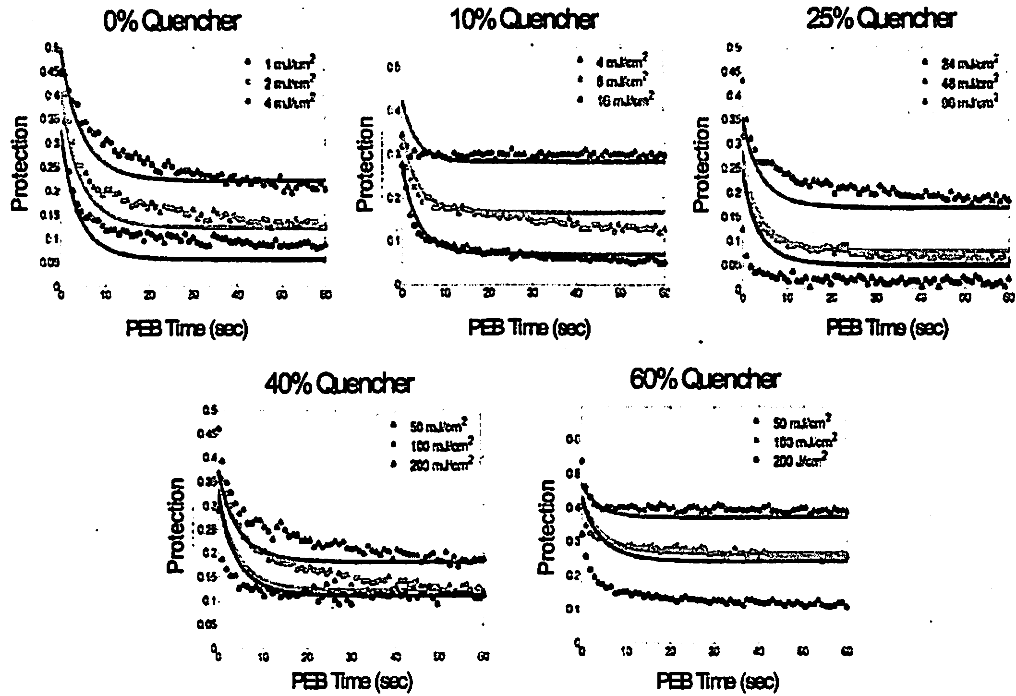

Fig. 9 AEQ fitting of the deprotection reaction (KrF model resist / 90°C PEB)
(data points: FTIR measurements/solid curve: modeling fitting)

The above measured reaction kinetic is best fitted by AEQ model through STORM-II simulations, where no diffusion terms are included since a flood exposure is conducted in the experiments. The fitting results for PEB temperature 90°C are shown by solid curves in Fig. 9. A nice fitting can be obtained by assuming AEQ modeling.

In the case of the KrF model resist, the concentration of protection group in the start of FTIR measurement is found to vary from sample to sample, which indicates that some of deprotection reaction occurs even before the PEB due to lower activation energy of the deprotection reaction. Through the best fitting, it is found that the reaction occurs at 2.5

sec before PEB starting with a same initial deprotection concentration of 0.75 for all samples.

An important fact is that, only one set of parameters (K_a, K_r, K_n, K_l, C-parameter) is needed by AEQ model to correctly predict all measurements at a fixed PEB temperature. This is because the AEQ model is based on correct physical insight rather than the strategy of data fitting.

Figures 10~12 show more fitting results of the protection concentration after 60 sec PEB at three bake temperatures, where both the FDQ and AEQ models are applied and compared. The protection concentrations are plotted against the photo-generated acid minus initial quencher loading ($[HA]_{generated}$ - [Q]). In this plot, triangle and circle markers represent the experimental and simulation results respectively. Different colors correspond to different quencher loadings. It is shown that, the new AEQ model provides a very good fitting of protection measurements while the FDQ model cannot predict measurements at all. The acid dissociation constant K_a is found to be 0.03 independent of quencher loadings and exposure conditions, which indicates that about 15% photo-generated acids dissociate to produce catalytic acids. This result confirms the existence of partial acid dissociation in this weak acid model resist.

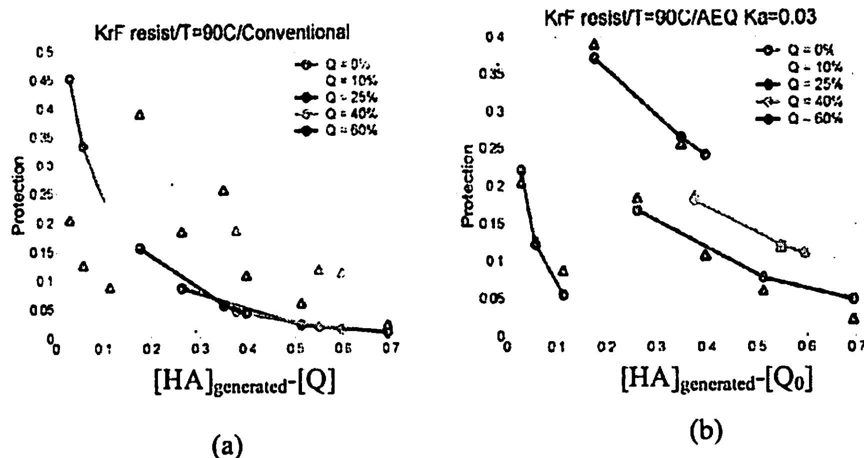

Fig. 10 Prediction of protection concentration at 60 sec 90°C PEB (a) FDQ model ($k_r = 1.0$, $k_l = 0.24$, $k_n = 3.0$, $m = 0.8$, C=0.03) (b) AEQ model (K_a = 0.03, $k_r = 3.6$, $k_l = 0.275$, $k_n = 4.0$, $m = 0.72$, C=0.03) (Triangles are experimental data and circles are the fitting results. $[HA]_{generated}$: photo generated acid, $[Q_0]$: initial quencher loading.)

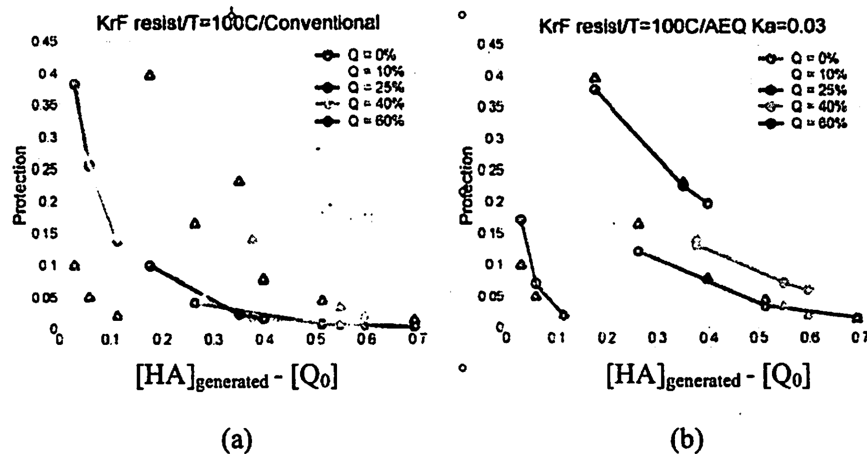

Fig.11 Prediction of protection concentration at 60 sec 100°C PEB (a) FDQ model ($k_r = 1.0$, $k_l = 0.06$, $k_n = 10.0$, $m = 0.8$, C=0.03) (b) AEQ model ($K_a = 0.03$, $k_r = 8.8$, $k_l = 0.24$, $k_n = 15.0$, $m = 0.88$, C=0.03) (Triangles are experimental data and circles are the fitting results. $[HA]_{generated}$: photo generated acid, $[Q_0]$: initial quencher loading.)

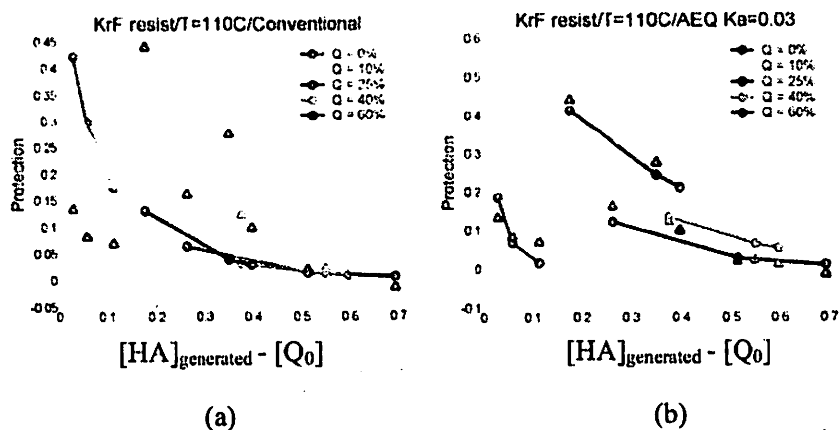

Fig.12 Prediction of protection concentration at 60 sec 110°C PEB (a) FDQ model (k_r = 1.0, k_l = 0.12; k_n = 7.0, m = 0.8, C=0.03) (b) AEQ model (K_a = 0.03, k_r = 15.4 k_l = 0.22, k_n = 18.0, m = 1.02, C=0.03) (Triangles are experimental data and circles are the fitting results. $[HA]_{generated}$: photo generated acid, $[Q_0]$: initial quencher loading.)

As shown in Fig. 13, the extracted deprotection reaction rates follow the Arrhenius relationship fairly well while the neutralization rates roughly show the Arrhenius relationship. The calculated activation energy was E_a = 0.87eV (20.06kcal/mol) for the deprotection reaction and E_a = 0.91eV (20.98 kcal/mol) for the neutralization reaction.

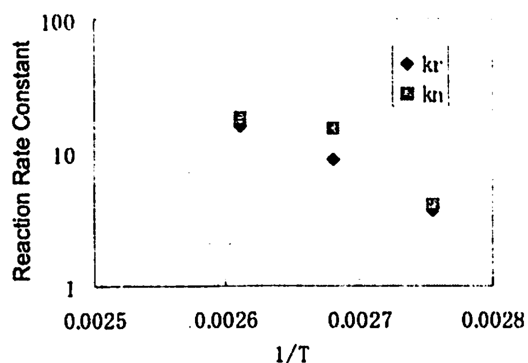

Fig. 13 Arrhenius plot for reactions in KrF resist

5.2 Modeling reaction kinetics in ArF model resist

Similar experiments and fitting strategy were conducted for the ArF model resist. Figure 14 shows FTIR measurements at PEB temperature of 130°C. Different from KrF model resist, the starting deprotection level is the same for all samples indicating that no reaction occurs before PEB.

For ArF model resist, the conventional FDQ model is able to predict the deprotection reaction kinetics fairly accurately as shown in Fig. 14, which indicates a different quencher mechanism from the KrF model resist.

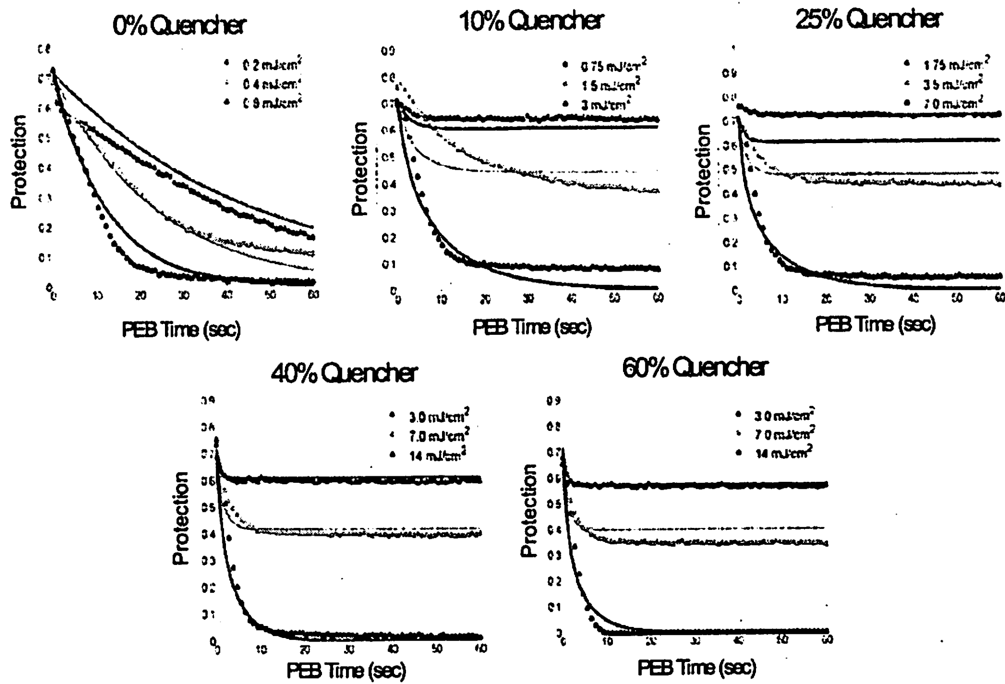

Figure 14: FDQ fitting of deprotection reaction (ArF resist / 120°C PEB).
(data points: FTIR measurements/solid curve: modeling fitting)
PEB 120°C $k_r = 0.44$, $k_l = 0.0$, $k_n = 4.0$, $m = 1.03$, C=0.05.

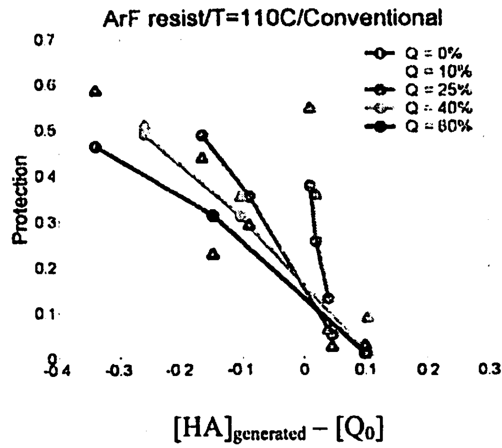

Fig. 15 FDQ prediction of protection concentration at 60sec of 110°C PEB
(k_r=0.22, k_l=0.0, k_n=1.33, m = 1.08, C=0.05)
(triangles: experimental data/circles: model fitting)

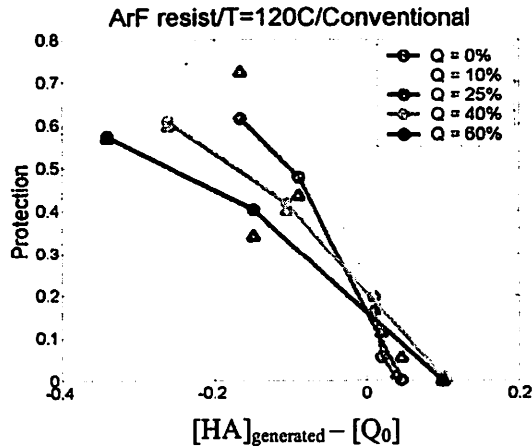

Fig. 16 FDQ prediction of protection concentration at 60sec 120°C PEB
(k_r = 0.44, k_l = 0.0, k_n = 4.0, m = 1.03, C=0.05)
(triangles: experimental data circles: model fitting)

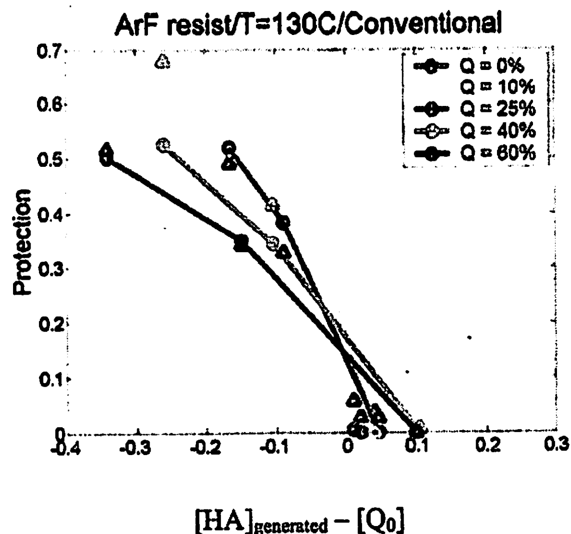

[HA]$_{generated}$ – [Q$_0$]

Fig. 17 FDQ prediction of protection concentration at 60sec 130°C PEB
(k_r=0.66, k_1=0.0, k_n=7.11, m = 0.75, C=0.05)
(triangles: experimental data circles: model fitting)

Figure 15~17 present more FDQ fitting results of reaction kinetics in the ArF model resist for PEB temperatures of 110°C, 120°C and 130°C, where the protection concentrations at 60 seconds PEB are plotted against ([HA]$_{generated}$ - [Q]). Again, only one set of parameters is used for one fixed PEB temperature. It is evident that, for all temperatures, the FDQ model is accurate enough to predict the reaction kinetics in ArF model resist. This means that the fluorinated-super-strong acid in ArF resists is fully dissociated acting like strong acids so that the FDQ model is still effective.

It is interesting to observe that, under most of exposure conditions for ArF model resist, the photoacid concentration is less than quencher, e.g. [H]$_{generated}$ –[Q]$_0$ < 0. Even under

this condition, the deprotection reactions occur to some extent prior to the completion of the neutralization reaction. Another observation is that the reaction speed for a lower-dose sample without quencher is slow but gradually continuing without an apparent stop to the reaction as is observed in the presence of the quencher.

The activation energies of deprotection and neutralization reactions are also calculated for the ArF model resist. Figure 18 shows that both reaction and neutralization rates present the Arrhenius type behavior, which again validates the model accuracy in this study. The calculated activation energies for deprotection and neutralization reactions are E_a = 0.74eV (17.06kcal/mol) and E_a = 0.848eV (19.55kcal/mol).

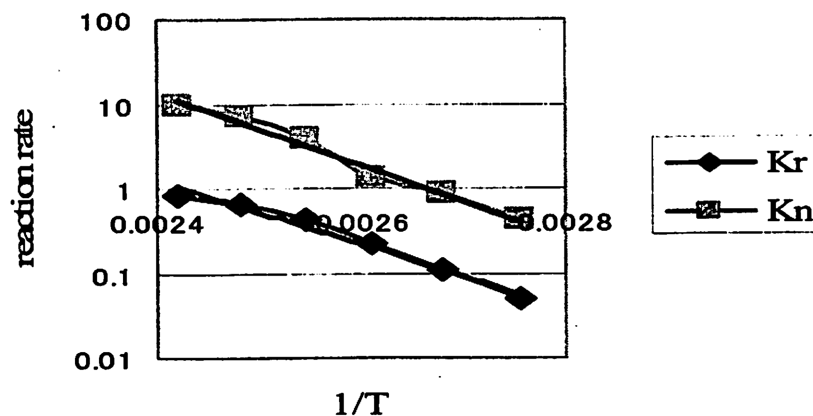

Fig. 18 Arrhenius plot for deprotection and neutralization reactions in ArF model resist

5.3 Disscussion of quencher effects in both model resists

Figure 10~12 and 15~17 show that, for both model resists, with quencher loading increasing, the slope of protection concentration versus ($[HA]_{generated}$ - [Q]) becomes

smaller with the only exception of the highest quencher loading of 60% in the KrF model resist. This result shows the improvement of resist stability to external base contamination. According to these plots, under the external base contamination that changes the value of ($[HA]_{generated}$ - [Q]), less variation of the protection concentration is resulted with higher quencher loading. This slope change due to quencher loading in the KrF model resist was successfully predicted by the new AEQ model. For the ArF model resist, the FDQ model in conjuction with the specific exposure condition that the initial photo generated acid is less the quencher concentration also predicts the same trend. It suggests that the same quencher effect can be acheived by different mechanisms in the weak-acid and strong-acid resist systems.

For both KrF and ArF model resists, adding quencher loading increases the required dose for pattern print thus rendering a high reaction contrast. Figure 19 shows the simulated deprotection contrast of isolated line using KrF model resist at PEB temperature of 100°C. Figure 20 presents the simulated deprotection contrast of isolated space using ArF model resist at bake temperature of 130°C.

As shown in Fig. 19, in the KrF model resist, the highest reaction contrast is obtained by a moderate quencher loading. Increasing quencher loading beyond 25% of PAG starts decreasing the reaction contast because the very high quencher loading suppresses the photoacid dissociation severely as resulted from the acid buffering effect and only very few active acid is produced. This reduction of active acids with too high quencher loading is consistent with the experimental observation that resist pattern cannot be resolved at

60% quencher loading no matter how high dose is exposed. This observation also indicates that the best resist performance in weak-acid resist systems is not necessarily achcived by the highest quencher addition and, instead, the optimized quencher loading is demanded.

With all benefits as described above, adding quencher, however, also degrades resist sensitivity and thus limits wafer throughput. Figure 21 shows the change of best dose under various quencher loadings for both model resists. Here the best dose is defined as the exposure dose that prints the smallest resist line the best. In Fig. 21, the best dose is normalized with that with no quencher. Clearly, much higher doses are required to resolve resist patterns at high quencher concentration. For the KrF model resist, quencher addition results into more buffered acid and much less active acid so that very high dose exposure is required. In contrast, for ArF model resist, the increase of the best dose is smaller due to no acid buffering effect. This observation seems to imply that the second type of quencher mechanism as present in the ArF model resist is preferred in terms of resist sensitivity. Further study is required to make solid conclusion. It should be pointed out that, the degraded resist sensitivity as caused by quencher loading is contradictive to one major motivation of developing CAR systems — high resist sensitivity. Therefore, quencher applications need be carefully tuned up balancing resist sensitivity and quencher benefits and quencher modeling illustrated in this chapter can leverage the use of quencher.

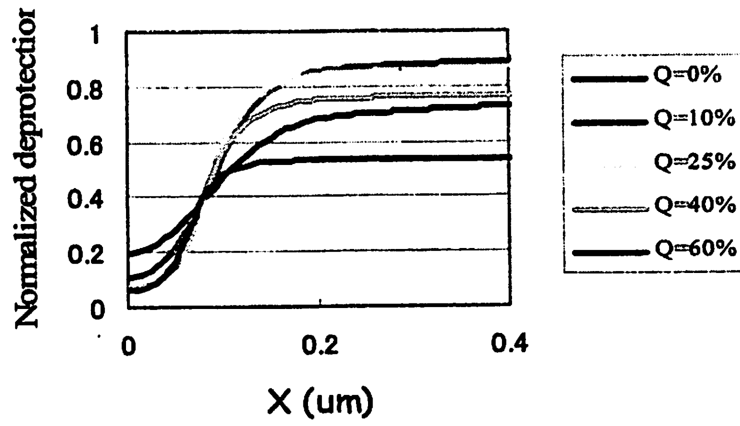

Fig. 19 Reaction contrast with various quencher loading (KrF resist/PEB 100°C)

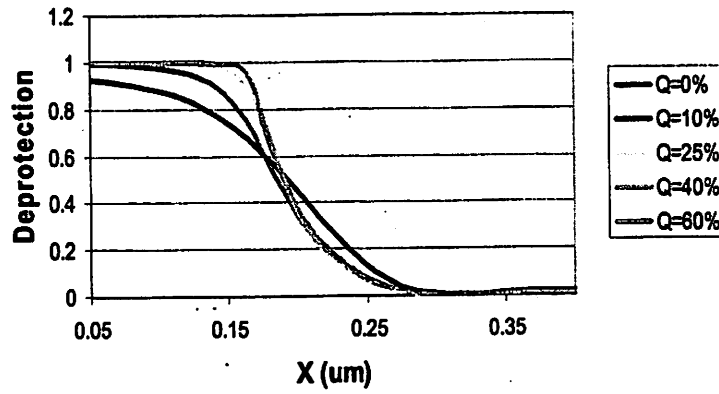

Fig. 20 Reaction contrast with various quencher loading (ArF resist/PEB 130°C)

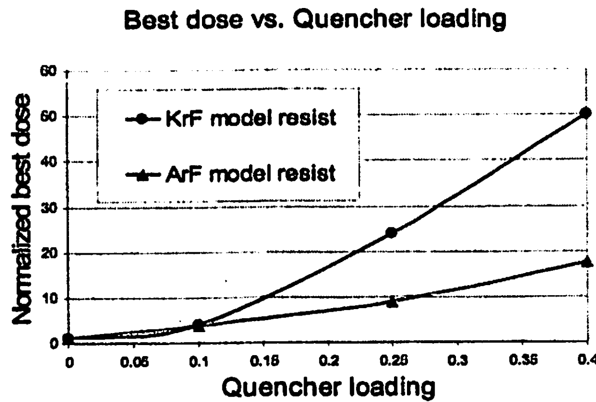

Fig. 21 Best dose variation with quencher loading

6. Calculations of exposure latitude and environmental stability applying AEQ model

Quencher effects on process latitude and environmental stability are simulated using the AEQ model on 160nm isolated line. Illumination constants used are λ=248 nm, NA = 0.60, σ_{out}=0.75, σ_{in} = 0.40. In the exposure latitude calculation, the best doses for each quencher loading are determined to print 160-nm line on wafer at best defocus. The defocus range of 0.0µm ~ 0.50µm and +/−10% dose variation are then simulated to investigate the sensitivity of linewidth to the exposure conditions. Exposure latitude is calculated by the criteria that the linewidth must fall into the range of 150 nm ~ 170 nm. Resist parameters of the KrF model resist at PEB temperature of 100°C are used in STORM-II simulations, where $k_r = 8.8$, $k_l = 0.24$, $k_n = 15.0$, $m = 0.88$, $k_d = 20$, $k_c = 632$, $K_a = 0.03$. Non-Fickian acid diffusion is assumed with constants of $D_0 = 4.5 \times 10^{-4}$

$\mu m^2/s$, ω=-5 and the quencher diffusion constant is $D_Q = 1 \times 10^{-4}$ $\mu m^2/s$.

The first example is the exposure latitude calculation using AEQ model. Figure 22 shows that, with quencher concentration increasing, the process window becomes wider at first and then gradually decreases slightly at very high quencher loading. This trend is consistent with the simulation results of reaction contrast change with respect to quencher loading.

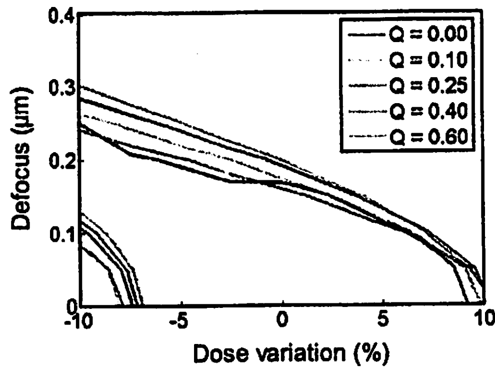

Fig. 22 Exposure latitude calculation (AEQ model)

In the second example, the environmental stability of the CA resist is calculated by evaluating the linewidth change in the presence of external base contaminants as shown in Fig. 23. It is evident that the higher the quencher loading, the more stable the CD in general, which agrees with common observations in real CA-resist processing.

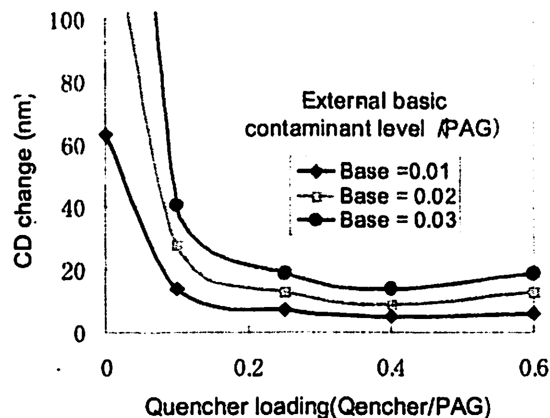

Fig. 23 Environmental stability calculation (AEQ model)

7. Conclusions

An acid-equilibrium-quencher (AEQ) model is examined in the weak-acid KrF model resist and strong-acid ArF model resist. Introducing the concept of the acid-dissociation equilibrium into resist modeling, the AEQ model successfully predicts the FTIR-experimental results for the model KrF resist with a weak photoacid generator. Conventional full-dissociation-quencher (FDQ) model cannot explain these FTIR measurements, which typically show multiple values of deprotection levels for a given $[HA]_{generated} - [Q]$ value if different quencher loadings are applied. As a simplified case of AEQ, the FDQ model is found to be successful in predicting the reaction kinetics for the model ArF resist.

FTIR measurements show that the deprotection variation with respect to ($[HA]_{generated}$ –

[Q]) becomes slower with higher quencher loading for both model resists, which indicates the improvement of resist stability. The stability improvement of KrF model resist is a consequence of acid buffering effect. Differently, in ArF model resist, the stability improvement seems to be obtained by selecting a special exposure condition, under which all reactions occur before the completion of acid neutralization. STORM-II simulations of reaction contrasts at various quencher loadings show that an optimized quencher loading is present for the KrF model resist, which is different from ArF model resist that typically shows better reaction contrast at higher quencher loading. The full AEQ model is included in UC Berkeley STORM-II resist simulator. STORM-II simulations of AEQ modeling show that the process window and environmental stability are improved in the presence of quencher loading.

7 Investigation of Shot Noise Induced Line-edge Roughness (LER) by Continuous Model Based Simulation

1. Abstract

A new strategy for LER simulation is proposed in this study, which applies a discrete model of 1~2nm scale for exposure, continuous reaction-diffusion model of 5nm scale for post-exposure bake (PEB) and a newly developed continuous statistical lateral dissolution model (SLDM) of 1nm scale for development. Without the enormous complexity of a molecular LER simulator, this new LER modeling is able to simulate LER induced by exposure statistics through incorporating impacts of PEB and dissolution. This LER simulator has been used to investigate factors that impact LER generation, such as non-Fickian diffusion, shot noise and resist contrast. SLDM has also been applied to analyze large unlikely roughness event (LURE) that can lead to chip failure through finding an equivalent lateral dissolution path for LURE. At last, a stress induced crack propagation LER model is proposed to understand the large correlation length commonly observed for line-edge roughness and flare related LER formation.

2. Concepts of continuous LER modeling

2.1 Modeling of exposure statistics

Two statistics are incorporated to model acid creation on exposure, which are the PAG dissociation statistics and photon shot noise. PAG dissociation statistics means that, the probability that a single PAG generates a photoacid P is a function of dose density I and resist sensitivity as described by the following formula

$$P = 1 - e^{-C*I} \tag{1}$$

Here C and I are Dill's C parameter and dose density respectively. On the continuous level, formula (1) will give normalized acid concentration. The photon shot noise causes local dose variation even at a uniform exposure. Assuming PAG spacing a, the dose intensity I incident upon single PAG area is given as

$$I = \frac{E_{h\upsilon} * N_{h\upsilon}}{a * a} \tag{2}$$

$E_{h\nu}$ and $N_{h\nu}$ are photon energy and photon number per PAG area. $N_{h\nu}$ follows Poisson statistics so that the term $C*I$ can be approximated by Gaussian statistics. The number $N_{h\nu}$ and the variance of $C*I$ — σ^2_{C*I} depend upon photon energy and resist sensitivity as shown by some examples given in Table 1. In the calculations, the C parameters and dose are chosen so that the same mean photoacid concentration (C*I=0.25) is obtained for all three wavelengths. Assuming the PAG spacing a to be 1.5nm, $N_{h\nu}$ is large for DUV and

about 4~8 for EUV. The variance σ^2_{C*I} increases for resists of high sensitivity.

Table 1 Calculation of σ^2_{C*I}

Wavelength (nm)	Dill's C (cm^2/mJ)	Dose I (mJ/cm^2)	Incident photon density ($photons/cm^2$) [13]	Photons per PAG area ($/nm^2$)	σ^2_{C*I}
248	0.01	25	$3.1x10^{16}$	698	0.0095*C*I
13.4	0.05	5	$3.4x10^{14}$	8	0.09*C*I
13.4	0.10	2.5	$1.7x10^{14}$	4	0.128*C*I

2.2 Modeling of post-exposure bake

The PEB process is modeled by coupled diffusion-reaction equations

$$\frac{\partial A}{\partial t} = k_r(1-A)H$$
$$\frac{\partial H}{\partial t} = \nabla(D\nabla H) - K_l H \tag{3}$$

Here ***A*** and ***H*** are the normalized deprotection and photoacid concentration. K_r, K_l and ***D*** are reaction rate, acid loss rate and acid diffusivity respectively. It is assumed that the deprotection reaction might lead to one of three diffusion types as Fickian diffusion, reduced non-Fickian (RNF) and enhanced non-Fickian diffusion (ENF). In Fickian diffusion, the acid diffusivity D is independent of reaction and remains as a constant value through PEB. The acid diffusivity D is reduced by deprotection reaction in RNF diffusion and increased in ENF diffusion. In STORM-II, non-Fickian diffusion is described by exponential functions,

$$
\begin{aligned}
D &= D_0 && \text{Fickean diffusion} \\
D &= D_0 e^{\alpha A} && \text{Enhanced non - Fickean diffusion} \\
D &= D_0 e^{-\alpha A} && \text{Reduced non - Fickean diffusion}
\end{aligned} \tag{4}
$$

This continuous PEB model does not incorporate any randomness of acid reaction events because its influence on latent edge blur is less noticeable than that of acid statistics due to the acid amplification effect, which means one acid catalyzes 50~100 reaction events in average. For example, *N* acids in a resist pixel volume will catalyze 50x*N*~100x*N* reaction events in total. If both acid generation and reaction events follow Poisson distribution, acid statistics will be the dominant statistic event. The above analysis is best described by a formula derived by Neureuther [84], which models E-beam shot noise as a result of a cascade of dependent sequential events. This formula shows that, for a pixel size that is irradiated with N_1 electrons and has N_2 photo generated acid and N_3 reaction events, the mean value and variance of reaction events in that volume can be formulated as,

$$
\frac{\sqrt{VAR}}{AVE} = \sqrt{\frac{1}{N1} + \frac{1}{N2} + \frac{1}{N3}} \tag{5}
$$

Although this formula is originally developed to track E-beam shot noise effect, it can be simply used to analyze LER generation in optical lithography. It shows that statistics of reaction events is negligible since *N3* is much larger than *N2*. In contrast, some researchers suggested that total resist edge variance is a summation of several components representing various events leading to a different formula,

$$
Var_total = Var1 + Var2 + Var3 + \ldots\ldots \tag{6}
$$

Formula (6) is based on an assumption that all those events are independent, which is certainly not true.

2.3 Statistical lateral dissolution model (SLDM)

SLDM assumes that near-edge dissolution (50~100nm) consists of many independent one-dimension dissolution events that occur only along the lateral direction as depicted in Fig.1. Although the mean deprotection concentration is the same for all lateral dissolution paths, deprotection fluctuation along each one of lateral path leads to line-edge position that fluctuates from path to path. To employ this simulation, deprotection fluctuation is characterized by standard deviation of deprotection concentration σ_A that merges the statistical effects of PAG dissociation and exposure shot noise. The grid size for SLDM calculation in this study is 1nm.

To calculate the dissolved distance for each path, Mack's dissolution rate model [14] is used in this chapter,

$$a = \frac{n+1}{n-1} A_{th}^{\ n}$$
$$R = \frac{R_{\max} * (a+1) * A^n}{(a+A^n)} + R_{\min} \tag{7}$$

R_{max} , R_{min} and A are maximum, minimum dissolution rates and deprotection concentration respectively. A_{th} and n are resist parameters, where a high n factor indicates high resist contrast.

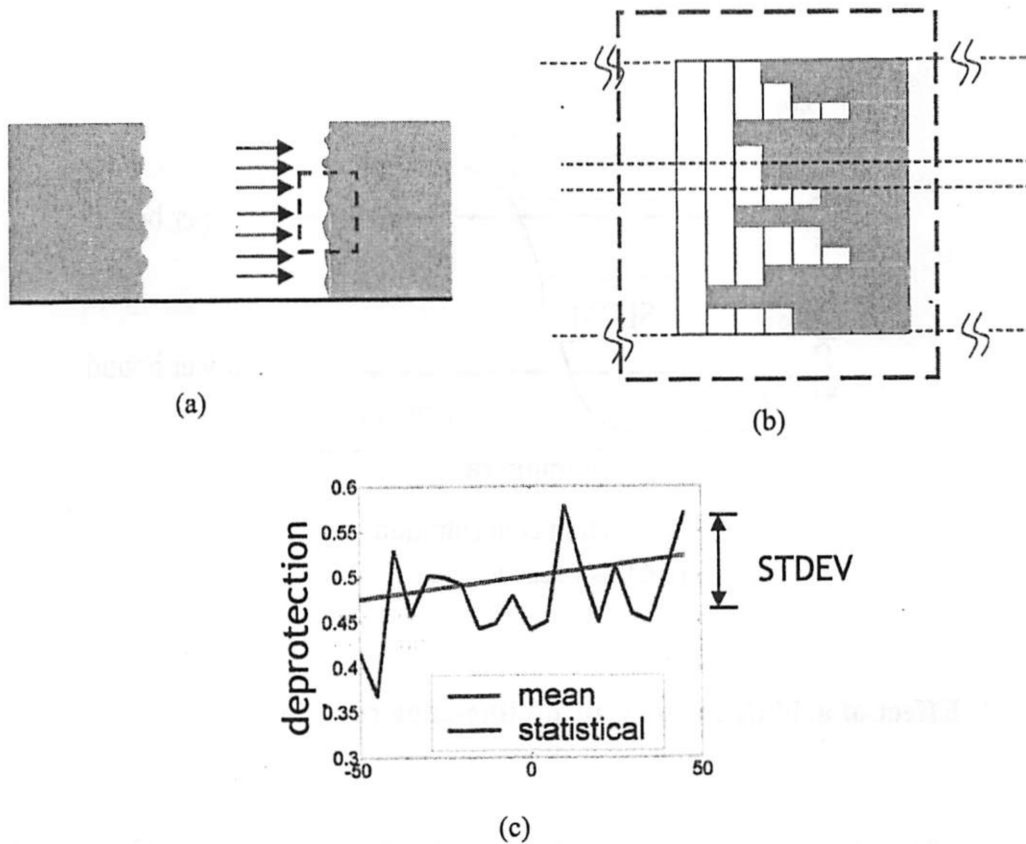

Fig. 1 (a) near-edge dissolution (b) lateral dissolution paths (c) mean and fluctuation of deprotection concentration

The near edge region to which SLDM is to be applied is selected by using preset upper and lower bounds of dissolution rate as illustrated in Fig.2. In region I, dissolution rate is higher than the upper bound and a threshold dissolution model is used. In region II, dissolution rate is smaller than lower bound and no dissolution will occur. SLDM model applies the lateral dissolution only within SLDM region that is defined by lower and upper bound.

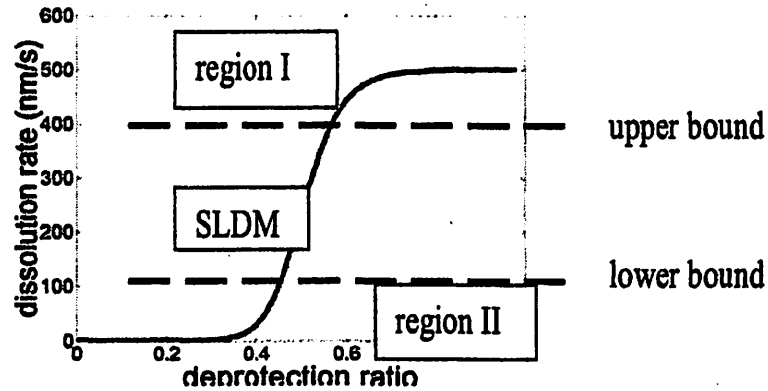

Deprotection concentration

Fig.2 Dissolution rate curve

3. Effect of acid diffusion type on line-edge roughness

It is shown in chapter 3 that state-dependent acid diffusion has significant impact on two-dimensional resist structures. For example, standing wave pattern is sensitive to acid diffusion type. The physical size of the standing wave is invisible for reduced non-Fickian type, only slightly reduced for Fickian diffusion and large for enhanced non-Fickian diffusion as shown in Fig.3. Above observation indicates that reduced non-Fickian diffusion generates the smallest inhomogeneity while enhanced non-Fickian diffusion results in the largest.

The same effect is also observed on the mesoscale inhomogeneity, such as surface roughness generated by partially exposure. In this section, resist surface roughness is simulated using STORM-II with a grid size of 7.5nm. Resist parameters for exposure

and PEB are: C = 0.015 cm^2/mJ, PAG spacing a = 1.7nm, σ^2_{C*I} = 0.1*C*I, I = 20 mJ/cm^2, K_r = 0.25,

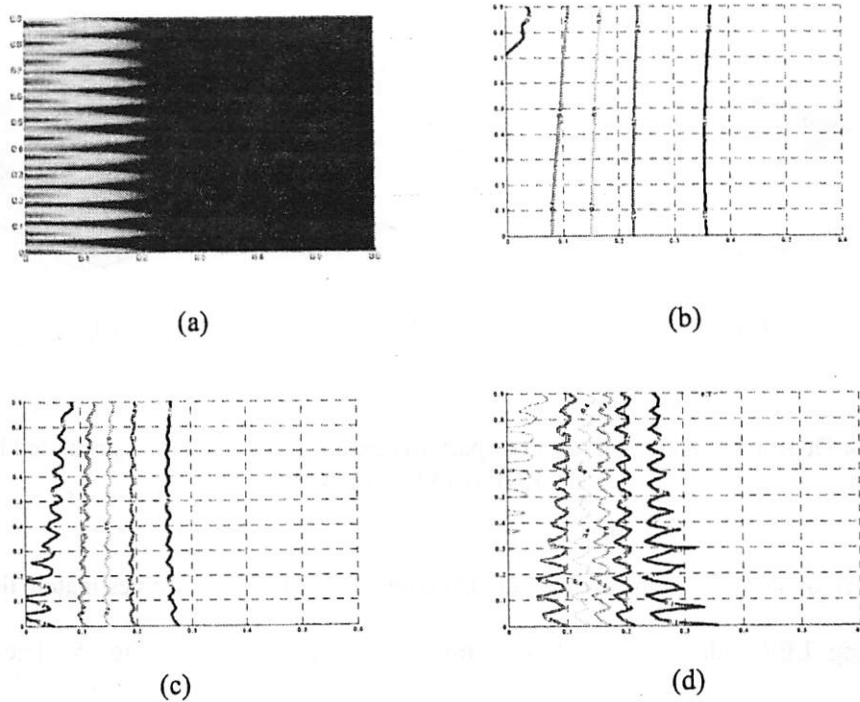

Fig. 3 (a) Image of standing waves (b) contour of deprotection concentration by RNF (c) contour of deprotection concentration by FD (d) contour of deprotection concentration by END

K_l = 0.02, bake time = 60s. Acid diffusion parameters for FD, RNF and ENF diffusions are D_0=5E-5um^2/s, ω = 0, D_0=3E-4um^2/s, ω=-5 and D_0 = 1E-5um^2/s, ω = 4. Diffusion parameters above are chosen such that all types result in the same linewidth and diffusion length. Simulated deprotection concentrations are shown in Fig.4, where z-axis represents the normalized deprotection concentration. It shows that the reduced non-Fickian

diffusion generates the smoothest resist surface while the enhanced non-Fickian diffusion gives the roughest surface. Fickian diffusion is in-between.

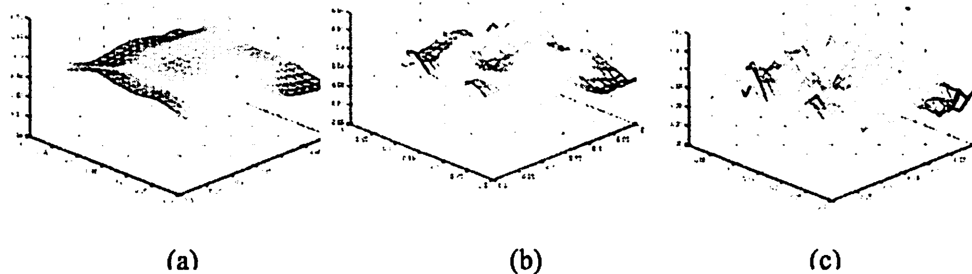

(a) (b) (c)

Fig. 4 Deprotection concentration of partially exposed resist surface simulated by (a) RNF (b) FD (c) ENF

The effect of the state-dependent acid diffusion on LER is also investigated through performing LER calculation to 0.6um trench edge as shown in Fig. 5. The resist parameters are the same as for surface roughness calculation except that a full exposure is applied with a dose of $30mJ/cm^2$. The simulation domain is 300nm x 300nm. Grid sizes ranging from 5nm to 10nm are employed to check the numerical stability to grid size. For each grid size and diffusion type, five simulations are done to reduce statistical errors and the 3σ LER is plotted in Fig.5 (b). The result shows that, continuous LER simulation is stable to the grid size. For all grid sizes, reduced non-Fickian diffusion generates the smallest 3σ LER of about 3nm, while Fickian and enhanced non-Fickian diffusions give about 50% and 100% higher LER respectively.

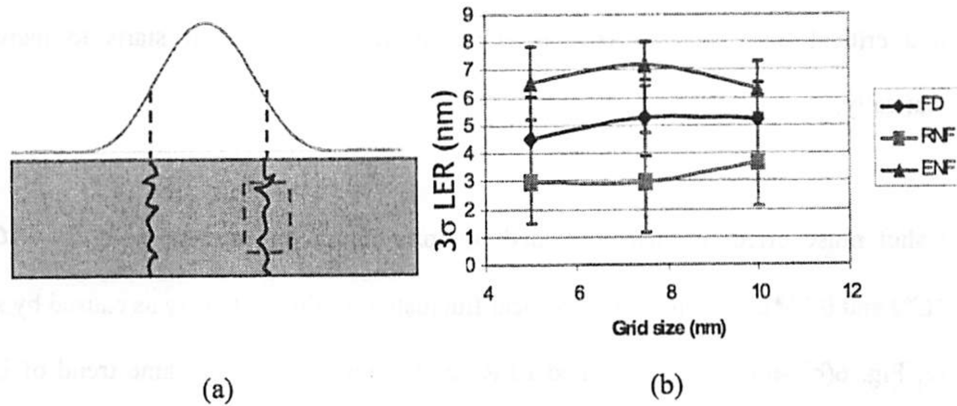

Fig. 5 (a) Resist edge for LER simulation (b) LER calculation results

4. Study of shot noise effect with exposure flare

In this section, flare effect is simply modeled by a background dose as shown in Fig. 6 (a). Four combinations of foreground/background doses are applied, which are 30+0mJ/cm^2, 27.5+2.5 mJ/cm^2, 25+5.0 mJ/cm^2 and 22.5+7.5 mJ/cm^2. These flare levels correspond to flare ratios of 0%, 8%, 16% and 25%. As shown in Fig.6 (a), with no flare, the resist edge is generated in the region of high image slope. As the flare level increases, the resist edge moves to the region of lower image slope. LER simulations here used the same resist parameters as in section 3.

The bottom curve in Fig. 6(b) shows LER results assuming only PAG dissociation statistics and no shot noise effect, which means σ^2_{C*I} is equal to zero. An increase of 3σ LER from 5nm to 11nm is observed while flare ratio increases from 0% to 25%, which is

due to the reduced image slope. It is also evident that the LER does not change much until a critical flare ratio of 16% is achieved, from which LER starts to increase dramatically.

The shot noise effect is then simulated by introducing non-zero σ^2_{C*I} as 0.05*$C*I$, 0.1*$C*I$ and 0.15*$C*I$, which models local fluctuation of dose intensity as caused by shot noise. Fig. 6(b) shows the calculated LER results. First of all, the same trend of LER verse flare ratio is observed and a same critical flare ratio is found. Secondly, the shot noise effect is not significant on LER until the critical flare level is achieved, wherein shot noise effect results in an even larger LER. It seems that PAG dissociation statistics overwhelm the shot noise effect at low flare, but not at high flare. The simulated trend of LER verse flare ratio fits experimental observations for both DUV [85] and EUV resists as shown in Fig.7.

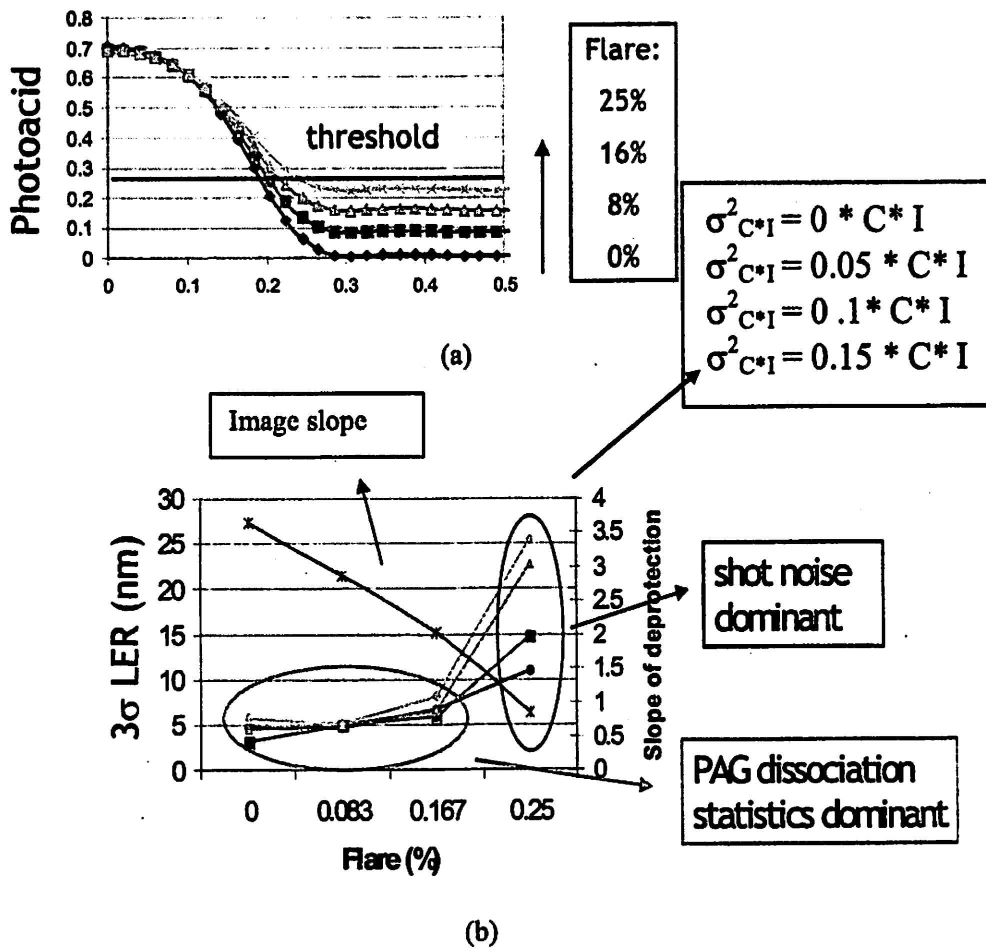

Fig. 6 (a) Image intensity with various flare ratios (b) Shot noise induced LER under different flare ratios

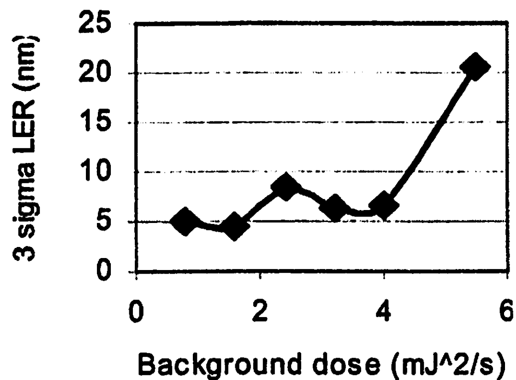

(a)

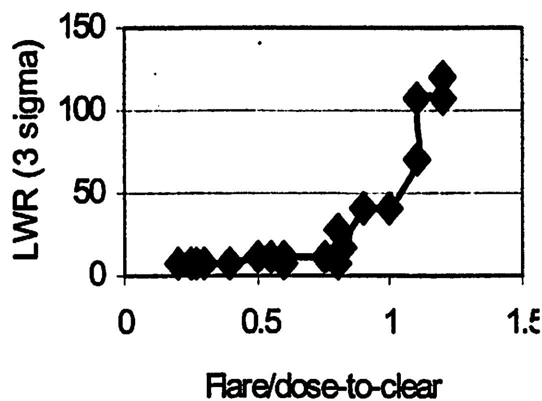

(b)

Fig. 7 LER versus flare (a) KrF resist, UVII-HS (courtesy of M. Williamson [107] at UC Berkeley) (b) EUV resist, EUV-2D, (courtesy of M. Chandhok at Intel)

5. Effect of resist contrast on LER

In this section, the impact of resist contrast on LER is simulated by applying only SLDM. The statistics that origin from both exposure and PEB is modeled by a composite standard deviation of deprotection concentration σ_A. The mean value of deprotection

concentration is calculated from STORM-II simulation of a 0.6um trench. Parameters R_{max}, R_{min} and A_{th} used by the formula (7) are 500nm/s, 0.1nm/s and 0.5. The constant n ranges from 4 to 12 to model different resist contrasts as plotted in Fig.8 (a). Upper and lower bounds of dissolution rate are chosen so that the size of SLDM region at n = 12 is 50nm. The dissolution time for each n is determined to form averaged resist edge location at the same position for all n factors. As shown in Fig.8 (b), higher resist contrast results in worse LER implying that high resist contrast and line edge roughness might be contradictive requirements.

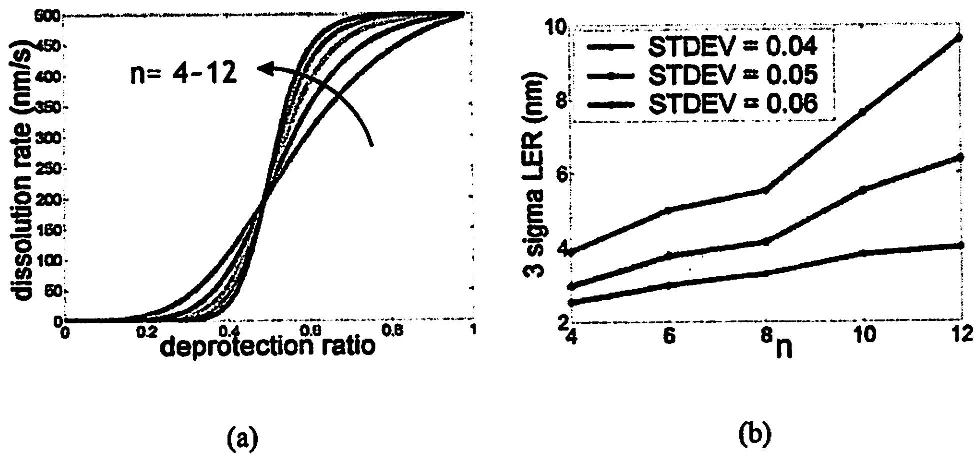

(a) (b)

Fig.8 (a) Dissolution rates for different n factor (b) LER versus n factor

6. Analysis of large unlikely roughness event (LURE)

Large unlikely roughness events (LURE) is assumed to be generated by two quarter-circle dissolution paths that merge and carve a large chuck off resist film as depicted in Fig.9. To analyze the probability of this 2D dissolution path, an equivalent lateral

dissolution path is determined first. It is assumed that a 1D lateral path has the same probability as the 2D path if it takes both paths the same dissolution time. Assuming a simple Gaussian statistics for resist edge deviation distribution, the probability of the equivalent lateral path, as well as of LURE, can thus be analytically calculated.

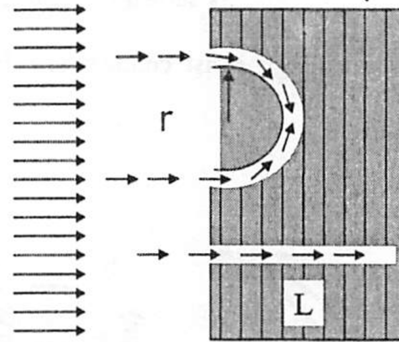

Fig. 9 LURE generation and equivalent lateral dissolution path

SLDM assuming n=12 and σ_A=0.05 is applied to simulate LER with flare ratios of 0%, 16% and 25%. σ_A is the composite standard deviation of deprotection concentration. Standard deviations of resist edge deviation are calculated as 2.47nm, 4.32nm and 9.01nm under those flare levels (Fig.10). Assuming LURE radius to be 15nm that is one third of CD for 45nm node, the lengths of the equivalent lateral paths at three flare ratios are 21.77nm, 22.8nm and 25.4nm. Fig. 10(a) shows that the LURE is located in about 8σ tail of Gaussian distribution for 0% flare ratio, 5σ for 16% flare ratio and 3σ for 25% flare ratio. Calculated LURE probabilities for all flare ratios are 10^{-16}, 10^{-7} and 10^{-3} respectively as shown in Fig. 10(b).

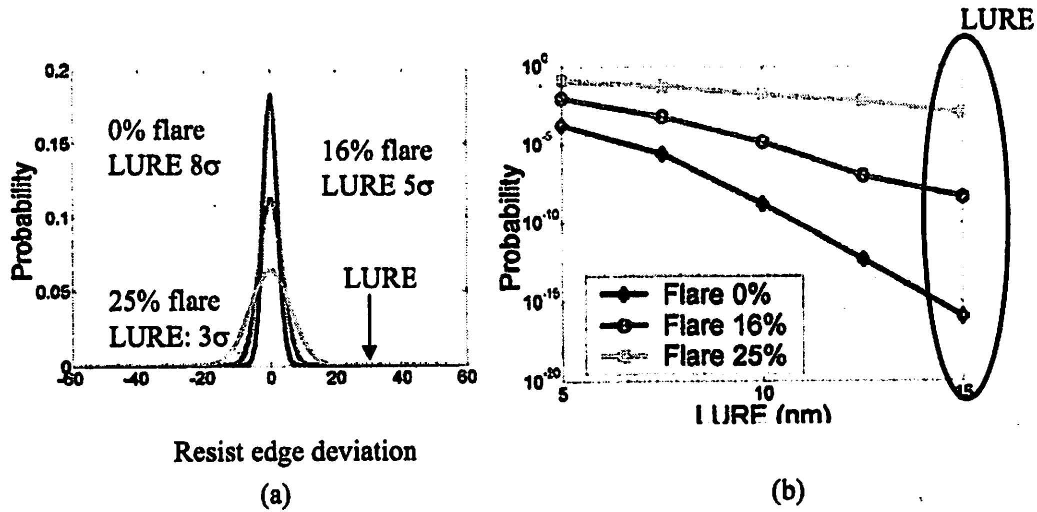

Fig. 10 (a) Statistical distribution of resist edge deviation (b) probability of 2D defect

7. Stress-induced crack propagation LER model

A large correlation length of 100nm~300nm in LER has often been observed in all wavelengths. Figure 11 shows LER SEM for UVII-HS, TOK11 and EUV-2D, which are KrF, ArF and EUV resists respectively. LER in UVII-HS and EUV are exaggerated here by adding background exposure. The scale of correlation distance is much larger than any molecular level phenomena and cannot be predicted by any molecular level or mesoscale LER modeling.

This study proposes a stress-induced crack propagation model to understand the above large length scale. This model assumes that stress in chemically-amplified resist will generate many microscopic cracks that act as micro dissolution channels for solvent penetration into resist film. The random crack propagation and/or merging, whose

length scale is in the same order as stress, are responsible for LER formation of large scale length. Stress in resist can be caused by resist volume swelling and shrinkage that may happen either in PEB or in development. This new model can be applied to investigate the influence of global phenomena on LER, such as flare effect, which cannot be understood by any molecular level LER modeling. According to stress-induced crack propagation LER modeling, the irradiation flare results in resist deformation in the unexposed region that increases strain and stress level in the resist matrix generating more micro cracks in the resist edge. This flare induced stress results in larger LER. The existence of a critical flare level, beyond which LER increases dramatically with higher flare level (Fig. 7(a)), is analogous to the fracture initiation in glassy materials, wherein fracture initiates while stress achieves a threshold value. At a flare level where correspondent stress and strain levels are high enough to initiate a large amount of micro cracks, a dramatic increase of LER values is predicted.

Although this stress-induced crack propagation LER model has not been systematically investigated due to a lack of time, abundant supportive references are present. Cheung et al [86] had observed silicon surface roughness of LER like topography as caused by delaminating bonded wafers, which is a good example correlating roughness with microscopic fracture. Tsuboi and his coworkers [87, 88] measured stress for a variety of resist film and detected the stress level of 7~9 MPa after exposure in both t-BOC CA resist and Novolak resist. Using old style ZEP resist, they found that resist patterns deformed as caused by resist stress. Similar pattern deformation was also observed in advanced EUV resists [89, 90]. However, further study is demanded to distinguish

material origins from optical effects for this pattern deformation. Ouano et al [91] observed crack propagation in PMMA during dissolution and suggested that strain in resist would enhance crack initiation and propagation in dissolution. Kramer et al [92, 93] measured the microscopic deformation and fracture of poly(vinylcyclohexane)-poly(ethylene)(PCHE-PE) block copolymer thin film and observed fracture events of about 100nm for 0.5um~0.7um resist film at a strain of about 5%. All above study somewhat support the new large scale LER model although they need to be verified upon more advanced chemically amplified resists.

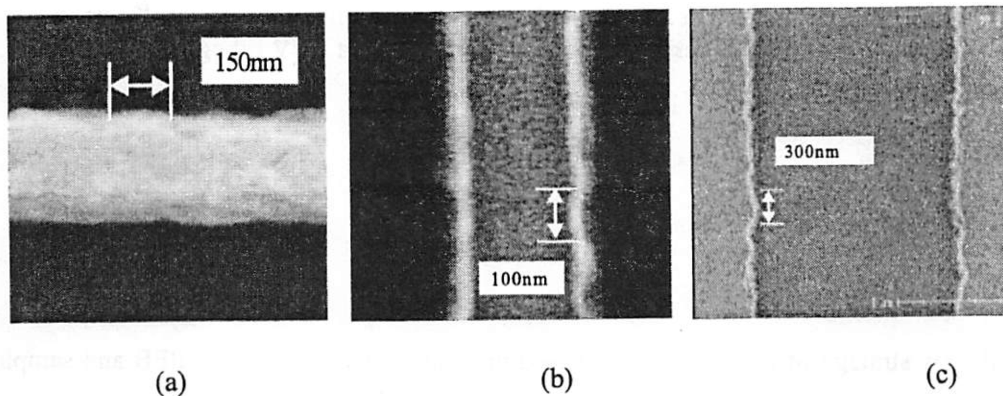

(a) (b) (c)

Fig. 11 Correlation length of LER for (a) UVII-HS (KrF) (b) TOK11 (ArF) (c) EUV-2D (EUV)

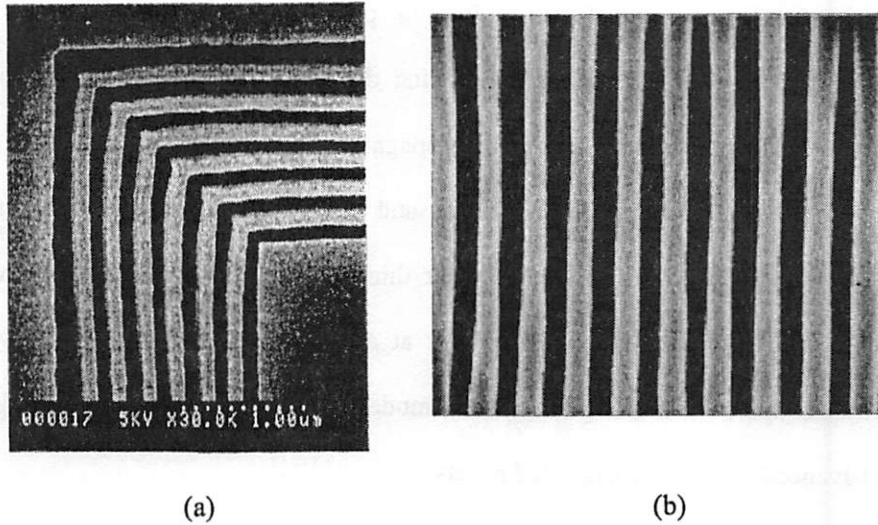

(a) (b)

Fig. 12 Pattern deformation obtained by (a) using ZEP resist in X-ray lithography [88] (b) using Shipley EUV-2D resist in EUV lithography [89, 90]

8. Conclusions

A new strategy of LER simulation based on continuous modeling of PEB and sampling of independent lateral dissolution paths is developed. Without numerical complexity, this continuous LER simulator is successfully applied to study phenomena influencing LER, including non-Fickian diffusion, shot noise and flare, and resist contrast. The nonlinearity of acid diffusion is found to be critical for LER. Among the three diffusion types, reduced non-Fickian diffusion results in the smallest roughness while enhanced non-Fickian diffusion gives the largest. Simulation of shot-noise induced LER shows that the impact of shot noise is not significant at low flare, but increases LER significantly at high flare. High resist contrast is found to result in worse LER. A stress-induced crack propagation

LER model is proposed to understand the large scale of correlation length and flare effect in LER. This new LER model is consistent with observations of polymer micro-fracture and fracture-induced silicon surface roughness found by many authors.

8 Development of Fast Resist Model for Accurate Prediction of Two Dimensional Layouts

1. Abstract

Two compact resist models RTM-α and RTM-β are developed for predicting critical dimension (CD) of two dimensional layouts. RTM-α assumes an adaptive resist threshold as function of image parameters on directions parallel as well as normal to feature edges. In RTM-β, resist threshold is a function of image properties along the direction normal to resist edge as well as the shape of resist contour. In developing the two new models, a new best fitting scheme that minimizes the fitting errors of effective CDs rather than resist threshold is used. Both new models are verified and compared with two widely used commercial models VTU and VT-5 [70-72] through extensive rigorous STORM-II simulation (288 cases) and LSI Logic 130nm technology (87 cases). In predicting SEM measurements of 2D patterns, prediction accuracy is improved by 100% and 40% using RTM-α and RTM-β compared with VT-5 while VTU does not predict correctly.

2. Pattern dependency of resist threshold

Resist threshold model is a rapid method of predicting resist pattern formation, wherein resist material coupled with image intensity above the threshold is dissolved after development and the part with irradiation energy below the threshold remains. Resist threshold is found to be a function of both the shape of resist pattern and imaging properties. Figure 1 shows one example of the pattern dependency of resist threshold, where four patterns are included as line-end gap, trench, trench-end gap and dense line. The definition of critical dimension for each pattern is also shown in Fig. 1. Experiments were done in LSI logic using 130nm technology. The resist material used is 3100A PAR715 (193 resist) on 830A of AR19 BARC. Annular illumination is applied with NA = 0.63, σ_{in} = 0.205 and σ_{out} = 0.58. Soft bake is 130°C-60sec and post-exposure bake (PEB) is 130°C-90sec. Dose ranges from 17mJ/cm^2 to 21mJ/cm^2. Resist thresholds extracted from SEM measurements are shown in Fig. 2(a). It is evident that resist thresholds vary greatly with different pattern shapes.

This pattern dependency can be reproduced by rigorous STORM-II simulations applying the following model of acid diffusion

$$\begin{aligned}
\frac{\partial A}{\partial t} &= K_r(1-A)H^m \\
\frac{\partial H}{\partial t} &= \nabla(D\nabla H) - K_l H \\
H(t=0) &= 1 - e^{-1.0*C*Dose} \\
D &= D_0 e^{\alpha A}
\end{aligned} \tag{1}$$

Resist inputs for the STORM-II simulations are: $K_r = 0.10$, $K_l = 0.03$, C=0.012 cm^2/mJ, dose = 30mJ/cm^2, D_0 = 2.5E-4um^2/s and ω = -4. A threshold dissolution model is used to calculate CDs and the threshold of deprotection concentration is 0.52.

As shown in Fig. 2(b), the resist thresholds extracted from STORM-II calculations demonstrate the same trend of pattern-dependency. This observation indicates that the pattern-dependency of resist threshold in PAR715 resist is mainly induced by acid diffusion during PEB noting that only acid diffusion in STORM simulations leads to multiple resist thresholds. This pattern dependency of resist threshold requires resist model to reflect characteristics of pattern shapes, which is realized in RTM-α and RTM-β through different approaches.

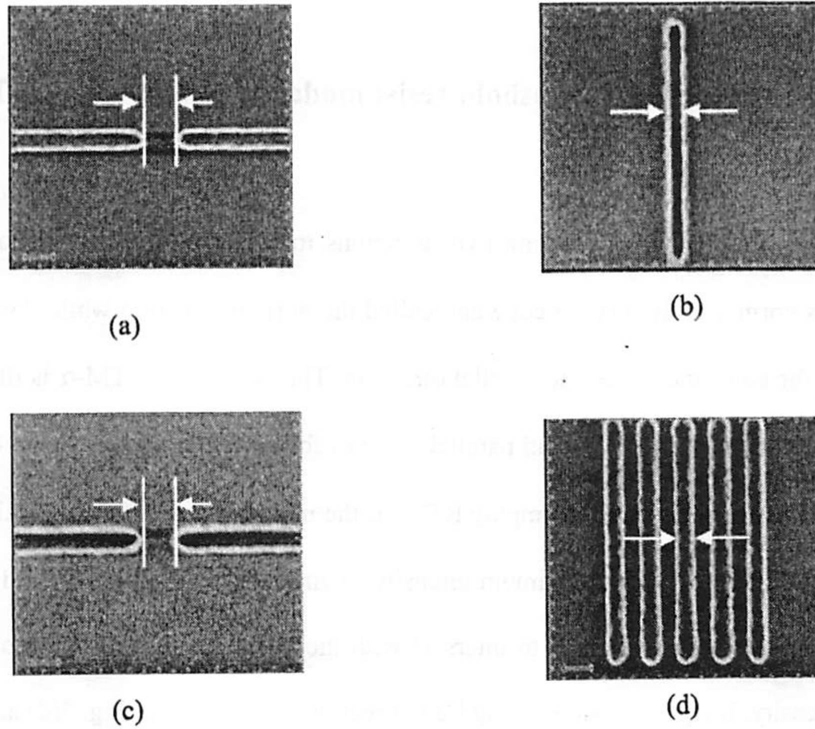

Fig. 1 (a) line-end gap (b) iso trench (c) trench-end gap (d) dense lines

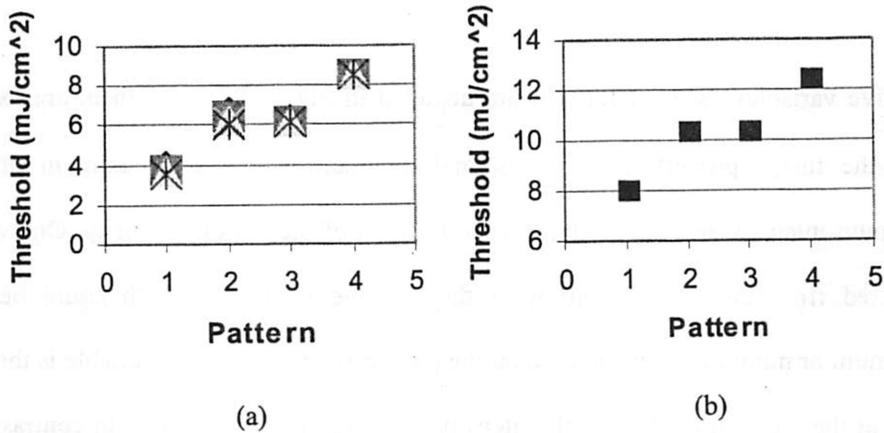

Fig. 2 Thresholds extracted from (a) SEM measurements (b) STORM simulations

3. Formulations of new threshold resist models — RTM-α and RTM-β

RTM-α uses image properties along two directions to determine resist threshold. One direction is normal to the feature edge and called the normal direction while the other is parallel to the edge and called the parallel direction. The concept of RTM-α is illustrated in Fig. 3 (a)~(c), where normal and parallel cutlines for each pattern are shown by solid and dotted lines respectively. To employ RTM-α, the middle image intensity, which is an average of the maximum and minimum intensity, is firstly located on the normal cultine. Then the parallel cutline is taken to intersect with the normal one at the location of the middle intensity. Image intensities along both directions are plotted in Fig. 3(d) and (e). It is shown that the parallel cutline is required to capture pattern characteristics because the intensities on the normal directions are very close to each other regardless of pattern shapes.

The five variables used for RTM-α are depicted in Fig. 4. Three of them are extracted from the image properties on the normal direction, which are maximum intensity, minimum intensity and image slope at the location of the middle intensity. One variable extracted from the parallel cutline is the extreme intensity, which could be either maximum or minimum depending upon the pattern shape. The other variable is the image slope at the location of the middle intensity along the parallel cutline. In contrast, VTU employs five variables that are all taken on the normal direction, which are maximum and

minimum intensity, and image slopes on three equally spaced locations.

RTM-β also uses five variables to determine resist threshold, three of which are image properties on the normal direction and two of which are extracted from image contour. In this section, RTM-β is illustrated by using line end pattern as an example (Fig. 5(a)). Figure 5 (b) plots image intensity along the normal direction in the line end. Three image parameters α_1 α_2 and α_s are minimum, maximum image intensities and image slope on the medium intensity respectively. The other two parameters are extracted from image contour as shown in Fig.5(c). On the contour line, points P_1, P_2 and P_3 are chosen so that the lengths of segments OP_1, P_1P_2 and P_2P_3 are equal to S — a characteristic length of resist proximity effect. Distances of P_1 and P_2 to tangent line then characterize the shape of resist edge and are chosen to formulate resist threshold function for RTM-β. The characteristic length S varies from 30nm to 70nm depending on resist type and need be carefully tuned to optimize RTM-β.

VT-5, another commercially available threshold model, is also used for comparison with RTM-α and RTM-β. The five variables used in VT-5 are minimum intensity, maximum intensity, maximum image slope, image intensity at the maximum slope and the curvature of image contour.

All compact resist models in this chapter employ a second order polynomial function to formulate resist threshold as described by the following equation,

$$
\begin{aligned}
Threshold = & \; C_0 + C_1\alpha_1 + C_2\alpha_2 + C_3\alpha_3 + C_4\alpha_4 + C_5\alpha_5 \\
& + C_6\alpha_1\alpha_2 + C_7\alpha_1\alpha_3 + C_8\alpha_1\alpha_4 + C_9\alpha_1\alpha_5 + C_{10}\alpha_2\alpha_3 \\
& + C_{11}\alpha_2\alpha_4 + C_{12}\alpha_2\alpha_5 + C_{13}\alpha_3\alpha_4 + C_{14}\alpha_3\alpha_5 + C_{15}\alpha_4\alpha_5 \\
& + C_{16}\alpha_1^2 + C_{17}\alpha_2^2 + C_{18}\alpha_3^2 + C_{19}\alpha_4^2 + C_{20}\alpha_5^2
\end{aligned} \tag{2}
$$

The above 21 C coefficients are normally determined by applying least square method of threshold fitting with procedures as following,

$$
\begin{aligned}
& \textit{fitted resist threshold} \quad \tilde{T}_i = \sum_{1}^{21} C_j \alpha_j \\
& T_i \quad : \textit{resist threshold extracted from CD measurement} \\
& \textit{threshold residual error}: R = \sum (T_i - \tilde{T}_i)^2 \qquad i: \textit{case number} \\
& \textit{method of least square}: \\
& \frac{\partial R}{\partial C_j} = 0 \;\; (j: 1 \sim 21) \;\; \Rightarrow \;\; C_j \;\; (j: 1 \sim 21)
\end{aligned} \tag{3}
$$

A modified least square method is developed in this chapter to implement RTM-α and RTM-β. This new method calculates C coefficients by minimizing CD residual error rather than threshold residual error. The CD error is calculated by dividing threshold error by image slope α_s for each test sample. The process flow for this modified least square method is illustrated by equation (4),

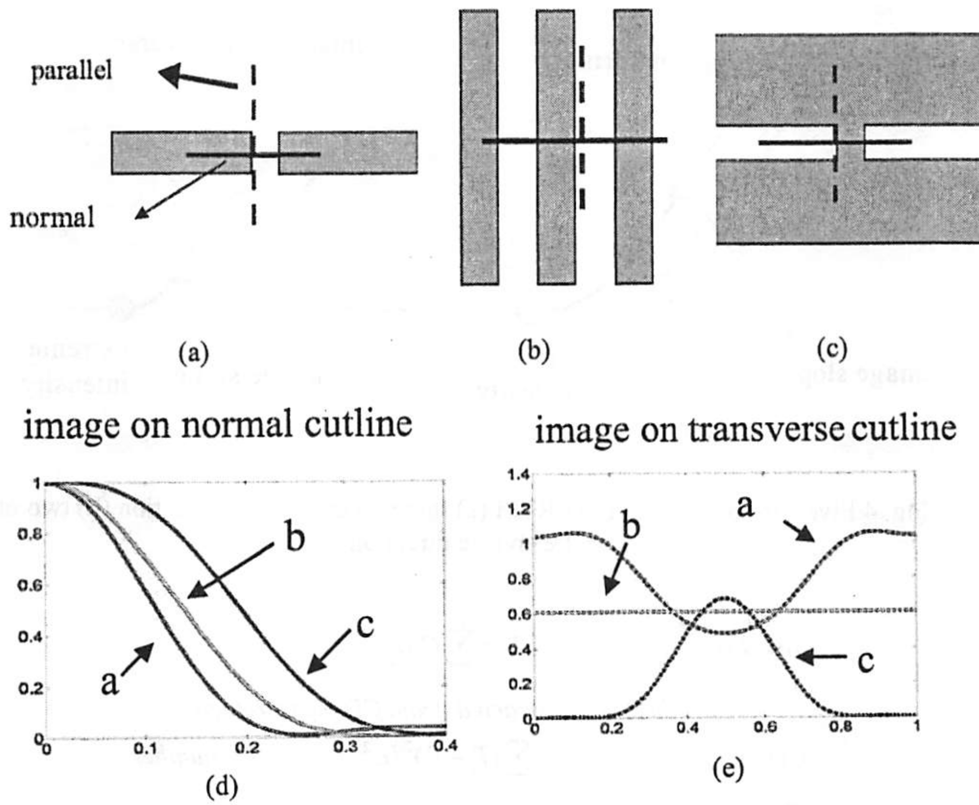

Fig. 3 (a) Line-end gap (b) dense lines (c) trench-end gap
(d) Images on the normal direction (e) images on the transverse direction

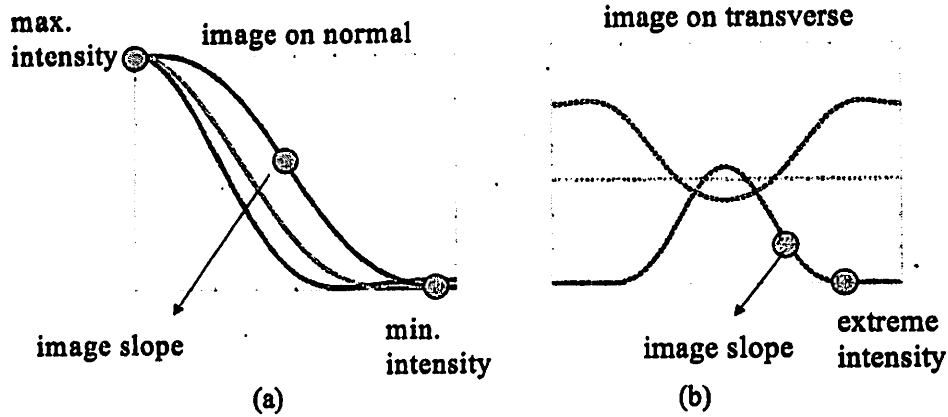

Fig. 4 Five variables used in 2D-RTM (a) three on the normal direction (b) two on transverse direction

$$\textit{fitted resist threshold} \quad \tilde{T}_i = \sum_{1}^{21} C_j \alpha_j$$

$$T_i \quad : \textit{resist threshold extracted from CD measurement}$$

$$\textit{CD residual error}: R = \sum (T_i - \tilde{T}_i)^2 / \alpha_{3,i}^2 \qquad i: \textit{case number} \tag{4}$$

$$\textit{method of least square}:$$

$$\frac{\partial R}{\partial C_j} = 0 \ (j: 1 \sim 21) \ \Rightarrow \ C_j \ (j: 1 \sim 21)$$

4. Numerical verification of resist threshold model

In this section, the effectiveness of VTU, VT-5, RTM-α and RTM-β is verified through fitting rigorous STORM-II simulations as an initial test. Image intensities are calculated based on illumination condition of NA = 0.5 and σ = 0.5. The fitting is made for 9 patterns including isolated line, isolated trench, dense line and space, line to line end, trench to trench end, T-shape line, T-shape trench, contact and post. A total of 288 cases

are made for verification by varying feature sizes from 200nm to 350nm, doses from 30mJ/cm^2 to 35mJ/cm^2 and defocus from 0 to 0.4 um. The first set of STORM simulations for fitting applies the same resist parameters as used in section 2 that gives similar diffusion length as in Shipley UV210 resist. The second set of STORM simulation models acid and quencher mutual diffusion using the following equations

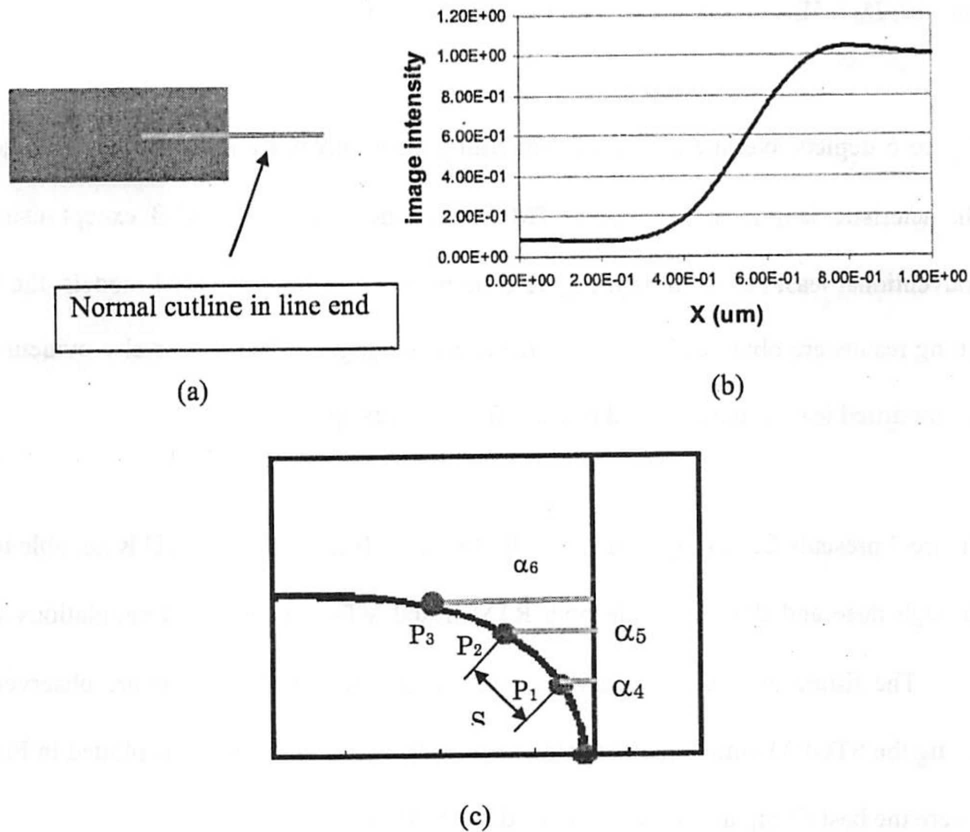

Fig. 5 (a) line end feature (b) image intensity along the normal cut (c) image contour

$$
\begin{aligned}
&\frac{\partial A}{\partial t} = K_r(1-A)H^m \\
&\frac{\partial H}{\partial t} = \nabla(D\nabla H) - K_n HQ - K_l H \\
&\frac{\partial Q}{\partial t} = \nabla(D_Q \nabla Q) - K_n HQ \\
&H(t=0) = 1 - e^{-1.0 * C * Dose} \\
&D = D_0 e^{\omega A}
\end{aligned}
\qquad (5)
$$

The resist parameters for STORM simulations are $K_r = 0.12$, $Kn = 3.0$, $K_l = 0.02$, C=0.012 cm^2/mJ, D_0 = 5E-4 um^2/s and ω = -5. Q_0 = 0.2, D_Q= 1E-4 um^2/s.

Figure 6 depicts average and maximum fitting errors given by RTM-β over a range of characteristic length S. In Fig.6, RTM-Test is the same as RTM-β except using a conventional least square fitting. Figure 6 shows that, for both STORM models, the best fitting results are obtained by using a characteristic length of 70nm. It is also evident that the modified least square method reduces fitting errors apparently.

Figure 7 presents CD fitting results for all 288 cases. It is seen that, VTU is not able to fit through dose and defocus while both RTM-β and VT-5 fits STORM simulations very well. The fitting accuracy of RTM-α is in the middle. Similar results are observed in fitting the STORM simulations of acid and quencher mutual diffusion as plotted in Fig. 8, where the best fitting accuracy is achieved by RTM-β.

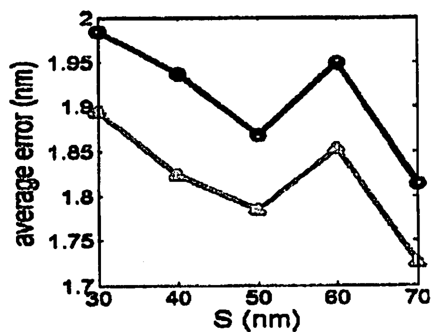

(a)

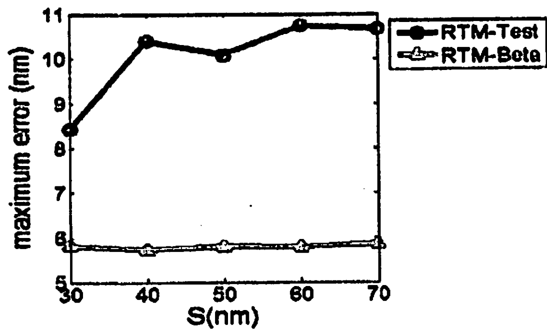

(b)

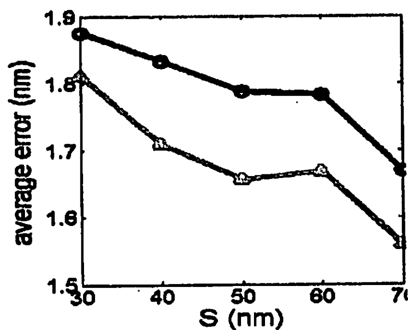

(c)

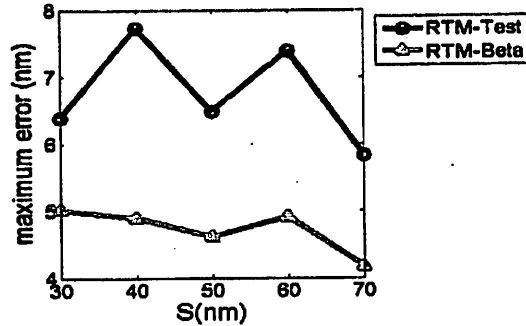

(d)

Fig. 6 Results of fitting STORM simulations by use of RTM-β (a) average error of fitting Model 1 (b) maximum error of fitting Model 1 (c) average error of fitting Model 2 (b) maximum error of fitting Model 2

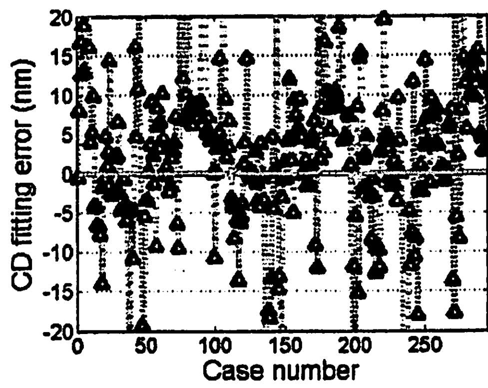

(a)

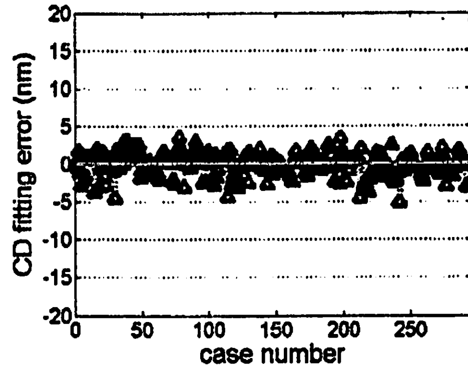

(b)

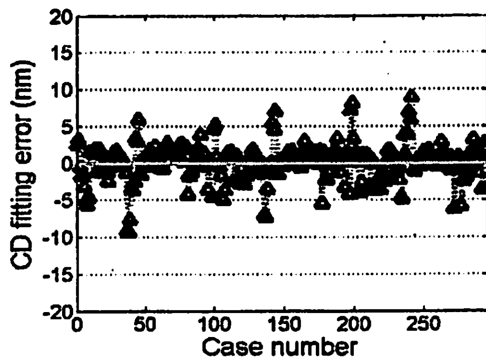

(c)

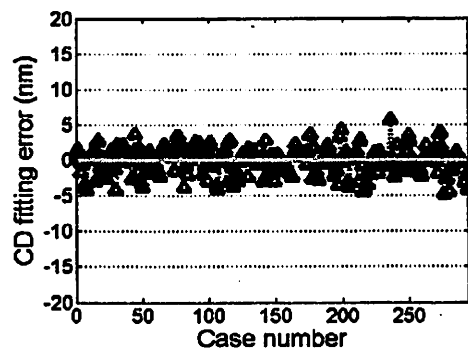

(d)

Fig. 7 Results of fitting the first set of rigorous simulations (a) VTU (maximum/average errors: 55/12.5 nm) (b) VT-5 (maximum/average errors: (5.0/1.5nm) (c) RTM-α (maximum/average errors: (9.3/2.5nm) (d) RTM-β (maximum/average errors: (5.8/1.7nm)

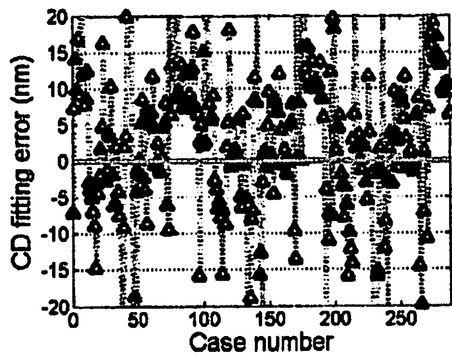

(a)

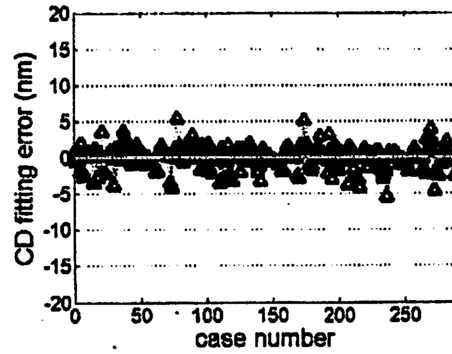

(b)

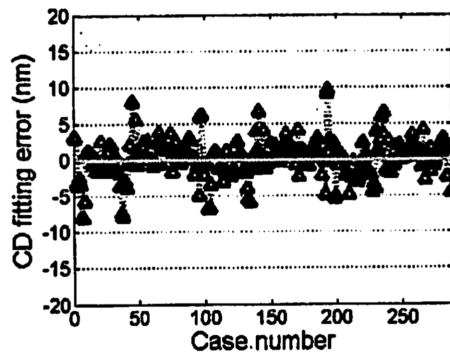

(c)

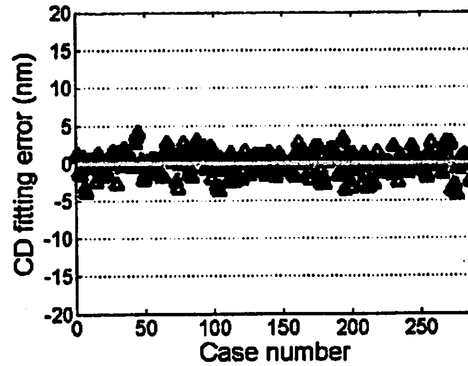

(d)

Fig. 8 Results of fitting the second set of rigorous simulations (a) VTU (maximum/average errors: 53/13 nm nm) (b) VT-5 (maximum/average errors: (5.46/1.58nm) (c) RTM-α (maximum/average errors: (9.6/2.5nm) (d) RTM-β (maximum/average errors: (4.15/1.55nm)

5. Experimental verification of resist threshold model

Experimental verification of model accuracy in this section is based upon experiments of an ArF tool using an in-house resist in LSI Logic. Annular illumination is applied with

NA = 0.63, σ_{in} = 0.205 and σ_{out} = 0.58. Beside those pattern shapes used in the simulation study, contact holes and posts are also incorporated to add more complexity. For each type of pattern, about ten different feature sizes ranging from 150nm to 300nm were printed for model verification. For all four models, a total of 65 cases are best fitted to determine 21 C coefficients in equation (2), which is called training process. The fitting results are shown in Fig. 9. After C coefficients are obtained from the training process, all threshold models were then applied to predict CDs for feature sizes not included in the training process to verify prediction ability, which is called testing process. A total of 20 cases are used for the testing process and the prediction results are shown in Fig. 10.

As shown in Fig. 9 and 10, VTU model presents the largest errors in both training and testing procedures. Although VT-5, RTM-α and RTM-β show similar fitting accuracy as shown in Fig. 9(b) ~ (d), the prediction accuracy in the testing process differs a lot. VT-5 results in maximum and average prediction errors of 5.6nm and 2.8nm. Using RTM-α reduces the prediction errors of VT-5 by more than one half rendering maximum and average errors of 2.69nm and 1.0nm. Compared with VT-5, RTM-β improves the prediction accuracy by about 30%, which gives prediction errors of 4.0/1.8nm. The maximum and average prediction errors obtained by use of VTU are 11.0nm and 4.0nm.

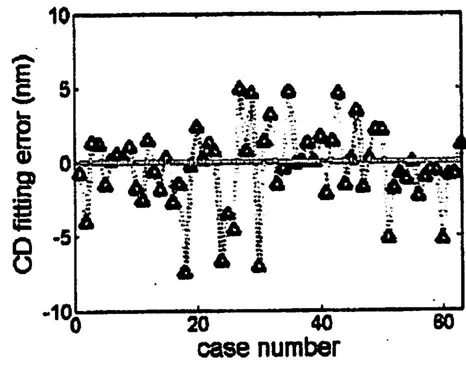

(a)

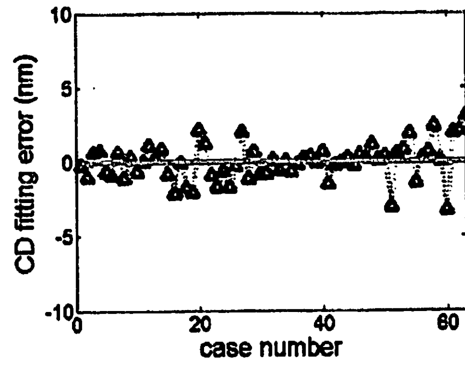

(b)

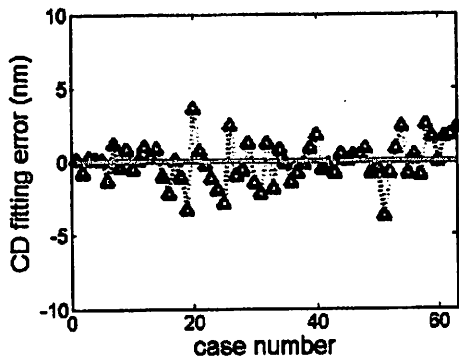

(c)

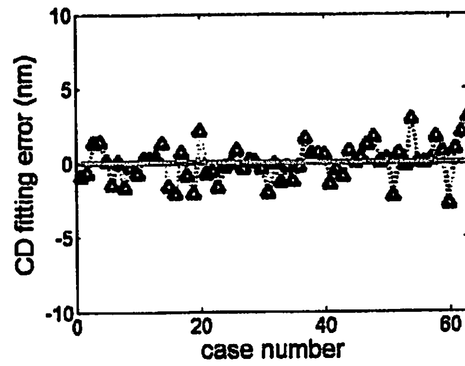

(d)

Fig.9 Fitting errors for training procedure (a) VT-U (maximum/average errors: 7.4/2.67nm) (c) VT-5 (maximum/average errors: 3.25/1.23nm) (e) RTM-α (maximum/average errors: 3.7/1.4 nm) (g) RTM-β (maximum/average errors: 3.0/1.2 nm)

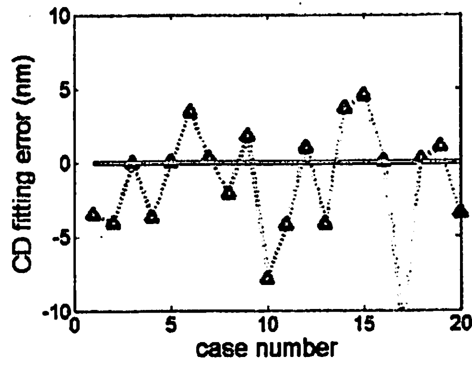

(a)

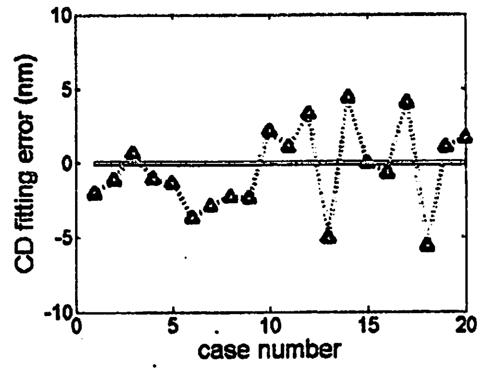

(b)

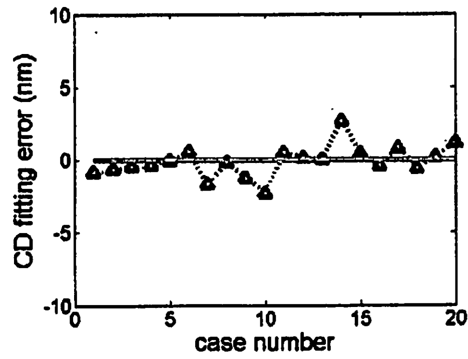

(c)

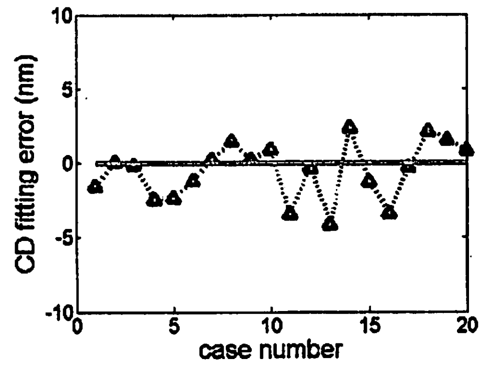

(d)

Fig.10 Prediction errors for predicting procedure (a) VT-U (maximum/average errors: 11.0/4.0nm) (b) VT-5 (maximum/average errors: 5.6/2.8 nm) (c) RTM-α (maximum/average errors: 2.69/1.0 nm) (d) RTM-β (maximum/average errors: 4.0/1.8 nm)

6. Conclusions

Two new compact resist models RTM-α and RTM-β are developed to predict 2D resist pattern print through modeling the dependency of resist threshold on 2D image characteristics. Resist threshold in both models is represented by a second order polynomial formula. The 21 coefficients are determined by minimizing the fitting errors of effective CDs rather than resist thresholds that is often used in other resist threshold models. Using this new best fitting strategy, more uniform CD fitting accuracy has been obtained. The two new models have been verified by extensive STORM-II simulations and SEM measurements and compared with commercially available models VTU and VT5. RTM-β and VT5 are found to fit STORM-II simulated CDs best with fitting accuracy of 1.5nm while RTM-α presents fitting accuracy of 2.5nm. VTU cannot fit simulated CDs correctly with a fitting error of 12nm. In predicting SEM measurements for 130nm LSI Logic technology, RTM-α shows the best performance with maximum/average prediction errors of 2.69nm/1.0nm while RTM-β gives maximum/average prediction errors of 4.0nm/1.8nm. Both VT5 and VTU are not accurate in predicting experimental results, which generate maximum/average errors of 5.6nm/2.8nm and 11.0nm/4.0nm respectively.

9 Summary

This study investigates the image to resist pattern formation of chemically-amplified resist (CAR) in optical lithography as influenced by photoacid diffusion, quencher loading and shot noise through the improvement of resist modeling as well as calibration strategy.

The effect of state-dependent acid transportation on two-dimensional pattern formation of a CAR system has been illustrated. The new physical insight into non-Fickian acid diffusion shows that, in enhanced non-Fickian diffusion (ENF), acid diffusion into reacted sites is preferred that tends to remain image non-uniformity in resist. In reduced non-Fickian (RNF) diffusion, more acid will move into unexposed region that can smooth image non-uniformity more effectively. The effect of Fickian diffusion is in the middle. This new understanding has resulted in a new strategy to determine acid diffusion type in CAR employing two acid diffusion sensitive structures — a sequentially double exposed cross pattern and standing waves. This new strategy has been successfully applied to Shipley UV210 and IBM APEX-E resists. In both resists, reduced non-Fickian diffusion predicts the corner-to-corner spacing in the double exposed cross pattern and the invisibility of standing waves the best. This study shows a clear evidence of the existence of RNF in both resists, which is critical for quantitative resist modeling, especially 2D pattern simulations.

For resists with small acid diffusion length, such as UV210 resist, the double exposed cross and standing wave on isolate line or trench are still not sufficiently sensitive. In this dissertation, a double exposed sharp resist pattern (DEST) is found to be highly sensitive to acid diffusion type as well as diffusion length. DEST profile is able to magnify the size of standing waves by one order of magnitude compared with that of one-dimensional line or space thus providing an accurate method of characterizing non-Fickian diffusion. A strong evidence of RNF in UV210 is shown by the disappearance of standing wave effects in DEST profiles.

In this dissertation, DEST structure has also been proved to be an excellent test pattern for resist characterization and a great process monitor. This dissertation shows that the DEST profile is an excellent monitor of resist surface phenomena because its shape is a strong function of substrate materials. For example, acid contamination is indicated by a long DEST tail of about 300nm as observed in DEST structures on top of silicon nitride coating. A first observation of "aircraft carrier" shape undercut is found in UV210 DEST on top of bare silicon, which implies either quencher surface loss or acid accumulation on the bottom substrate. The above capability also makes DEST structure potential applications in the characterization of resist component leaching and water uptake in immersion lithography. Both numerical and experimental studies show that the length of the DEST wedge-shape islands is about 10 times more sensitive to process condition fluctuations than linewidth and thus DEST is good for accurate process monitor needed by stringent process control for the cutting edge technology.

Quencher loading has become very common in advanced chemically-amplified resist. However, quencher mechanism still remains unclear limiting both quantitative resist modeling and better use of quencher. This dissertation has explored the quencher mechanism in both strong-acid and weak-acid model resists by use of real-time FTIR measurement of reaction kinetics during PEB. The model resists used in this work consist of both a KrF acetal type resist with weak photoacid generator (PAG) and ArF ester-type resist with strong photoacid generator. Both model resists have five different quencher loadings.

This dissertation has shown that different quencher mechanisms exist in these two types of model resists through interpreting reaction kinetics over a variety of exposure doses and PEB temperatures. In the weak-acid resist, photo-generated acid only partially dissociated to realize acid dissociation equilibrium because acid strength decreases dramatically in organic solvent such as resist matrix. The quencher loading essentially influences the dissociation equilibrium to generate more buffered acid and thus makes resist system more robust in a mechanism analogous to "buffered acid". This mechanism was modeled by acid-equilibrium quencher (AEQ) model that was first proposed by Nagahara [19~21]. In the strong acid model resist, a fully photoacid dissociation occurs and there is no buffered acid. However, under the exposure conditions that the photo-generated acid concentration is lower than quencher level, adding quencher loading can still achieve an improvement of environment stability in ArF strong-acid model resist. In this case, all deprotection reactions occur before the completion of acid neutralization.

A new strategy for LER simulation has been developed in this study to evaluate process effects on LER formation without any numerical complexity. It applies a discrete model at 1~2nm scale for exposure, continuous reaction-diffusion model at 7nm scale for post-exposure bake (PEB) and a newly developed continuous statistical lateral dissolution model (SLDM) of 1nm scale for development.

This new LER simulation strategy is able to predict correct trends of LER formation with lithography conditions. This LER simulator correctly predicts that LER gradually increases with higher flare level and dramatically rises beyond a threshold flare level as observed in both DUV and EUV resists. This is the first time that this trend on LER formation can be predicted by simulation. Simulation also shows that shot noise only causes minor difference in LER except that, when flare level is higher than the threshold level, shot noise effect increases LER apparently. This new simulation scheme has also been applied to investigate effects of state-dependent acid transportation and resist contrast on LER generation, which shows that reduced non-Fickian diffusion type is able to reduce LER size and high resist contrast will result in larger LER.

Stress-induced crack propagation model has been proposed to understand the large length scale in LER that cannot be predicted in any other LER models. This model suggests that strain/stress in resist generates micro cracks that act as micro dissolution channels in development leading to LER generation. The strain and stress are resulted from resist deformation that may occur during either post-exposure bake or dissolution process. In

this new model, the length scale of LER should be at the same as the stress effect that is responsible for the large correlation distance. This new LER model also explains the more global flare effect on LER and the sudden increase of LER while flare level is higher than a threshold value. Preliminary experimental proofs of the stress-induced crack propagation LER model have been found in some publications, but far from adequate. Innovative techniques need to be developed to observe micro crack generation in chemically-amplified resists in the future.

Two compact resist models RTM-α and RTM-β have been developed in this dissertation. Both new models are verified and compared with two widely used commercial models VTU and VT-5 through extensive rigorous STORM-II simulation (288 cases) and LSI Logic 130nm technology (87 cases). In fitting rigorous STORM-II simulation, VT-5 and RTM-β show the least fitting error and RTM-α comes next. In predicting SEM measurements of 2D patterns for LSI logic 130nm technology, prediction accuracy is improved by 100% and 40% using RTM-α and RTM-β compared with VT-5 while VTU does not predict correctly at all. It shows that the compact models RTM-α and RTM-β provide two alternative methods to evaluate 2D layout printing of full chip scale.

Bibliography

[1] Gordon E. Moore, "Cramming more components onto integrated circuits", Electronics, Vol. 38, number 8, April 19, 1965

[2] IRTS roadmap, http://public.itrs.net/

[3] H.Ito and C.G. Willson, Polym. Eng. Sci., vol.23, 1021, 1982.

[4] J.Frechet, H. Ito and C.G. Willson, Proc. Microcircuit Eng. Vol.82, 260, 1982.

[5] F.H. Dill, "Optical lithography", IEEE Trans. Electron. Devices, ED-22(7), 440, 1975

[6] F.H. Dill, W.P. Hornberger, P.S. Huage, and J.M. Shaw, "Characterization of positive photoresist", IEEE Trans. Electron Devices, ED-22(7), 445, 1975

[7] K.L. Konnerth and F.H. Dill, "In situ measurement of dielectric thickness during etching or developing process", IEEE Trans. Electron Devices, ED-22(7), 452, 1975

[8] F.H. Dill, A.R. Neureuther, J.A. Tuttle and E.J. Walker, "Modeling projection printing of positive photoresists", IEEE Trans. Electron Devices, ED-22(7), 456, 1975

[9] J.L. Reynolds, A.R. Neureuther and W.G. Oldham, "Simulation of dry etched line edge profiles", Journal of Vacuum Science & Technology, vol.16, no.6, Nov.-Dec. 1979, pp.1772-5.

[10] A.R. Neureuther, C.Y. Liu and C.H. Ting, "Modeling ion milling", Journal of Vacuum Science & Technology, vol.16, no.6, Nov.-Dec. 1979, pp.1767-71.

[11] A.R. Neureuther and W.G. Oldham, "Simulation and modeling of profiles in lithography and etching", Third Biennial University/Industry/Government Microelectronics Symposium. IEEE. 1979, pp.116-22. New York, NY, USA.

[12] A.R. Neureuther, D.F. Kyser and C.H. Ting, "Electron-beam resist edge profile

simulation", IEEE Transactions on Electron Devices, vol.ED-26, no.4, pp.686-93. 1979.

[13] W.G. Oldham, S.N. Nandgaonkar, A.R. Neureuther and M. O'Toole, "A general simulator for VLSI lithography and etching processes. I. Application to projection lithography", IEEE Transactions on Electron Devices, vol.ED-26, no.4, pp.717-22. 1979.

[14] C.A. Mack, "PROLITH: A Comprehensive Optical Lithography Model", Proc. Of SPIE, Vol. 538, 207, 1985

[15] W. Henke, D. Mewes, M. Weiss, G. Czech and R. Schiessl-Hoyler, "Simulation of defects in 3-Dimensional resist profile in optical lithography", Microelectronic Engineering, vol. 13, 497, 1991

[16] M.E. Law and R.W. Dutton, "Verification of analytic point defect models using SUPREM-IV", IEEE Trans. CAD, vol. 7, 181, 1988.

[17] http://cuervo.eecs.berkeley.edu/Volcano/

[18] http://www.panoramictech.com/

[19] S. Nagahara, M. Fujimoto, M. Yamana, and M. Tominaga, J. Photopolym. Sci. Technol., Vol.16, 351, 2003.

[20] S. Nagahara, M. Fujimoto, M. Yamana, and M. Tominaga, "Advances in Imaging Materials and Processes", edited by H. Ito, P. R. Varanasi, M. M. Khojasteh and R. Chen, 233, 2004.

[21] S. Nagahara, L. Yuan, W.J. Poppe, A. Neureuther, Y. Kono, A. Sekiguchi, K. Fujiwara, T. G. Watanabe, K. Taira, S. Kusumoto, T. Nakano and T. Shimokawa, "understanding quencher mechanism by considering photoacid-dissociation equilibrium in chemically amplified resist", Proc. Of SPIE, vol. 5753, 2005.

[22] Q. Lin, R. Sooriyakumaran and W.S. Huang, "Toward controlled resist line-edge

roughness: material origin of line-edge roughness in chemically amplified positive-tone resists", Proc. Of SPIE, vol. 3999, 230, 2000.

[23] S.V. Postnikov, M.D. Stewart, H.V. Tran, M.A. Nierode, D.R. Medeiros, T. Cao, J. Byers, S.E. Webber and C.G. Willson, "Study of resolution limits due to intrinsic bias in chemically-amplified photoresists", J. Vac. Sci. Technol. B, vol.17, no.6, pp.3335-8, Nov. 1999.

[24] K. Hattori, J. Abe, and H. Fukuda, Proc. SPIE, 4691, 1243 (2002).

[25] Hattori K, Hotta S, Hagiwara T, Fukuda H. "Analysis of quencher diffusion in chemically amplified resists and its effect on imaging characteristics", Journal of Photopolymer Science & Technology, vol.13, no.3, 477-84, 2000.

[26] M. D. Smith, C. A. Mack, J. D. Byers, Proc. SPIE, vol. 5977, 1482 (2004)

[27] R.A. Ferguson, "Modeling and simulation of reaction kinetics in advanced resist process for optical lithography", PhD thesis, University of California at Berkeley

[28] Zuniga M, Tomacruz E, Neureuther AR. "Diffusion effects in chemically amplified deep-UV resists", Proc. of SPIE, vol.2195, pp.320-8. 1994.

[29] J.S. Peterson, C.A. Mack, J. Sturtevant, J. Byers and D.A. Miller, "Non-constant diffusion coefficients: short description of modeling and comparison to experimental results", Proc. of SPIE, Vol. 2438, pp.167-180, 1995.

[30] M.D. Stewart, M.H. Somervell, V.T. Hoang, S.V. Postnikov, C.G. Willson, "Study of acid transportation using IR spectroscopy and SEM", Proc. Of SPIE, Vol. 3999, 665, 2000.

[31] E. Croffie, Mosong Cheng and Andrew Neureuther, "Moving Boundary transport model for acid diffusion in chemically amplified resists", J. Vac. Sci. Technol. B17(6),

3339-3344, 1999.

[32] F.A. Houle, W.D. Hinsberg, M. Morrison, M.I. Sanchez, G.Wallraff, C. Larson and J. Hoffnagle, "Determination of coupled acid catalysis-diffusion processes in a positive-tone chemically amplified photoresist", J. Val. Sci. Technol., B, 18(4), Jul/Aug, pp. 1874-1885, 2000.

[33] J. Byers, J. Peterson and J. Sturtevant, "Calibration of chemically amplified resist models", Proc. of SPIE, Vol. 2724, pp.156-162, 1996.

[34] Lin EK, Soles CL, Goldfarb DL, Trinque BC, Burns SD, Jones RL, Lenhart JL, Angelopoulos M, Willson CG, Satija SK, Wen-li Wu. "Measurement of the spatial evolution of the deprotection reaction front with nanometer resolution using neutron reflectometry", Proc. Of SPIE, vol.4690, 2002, pp.313-20.

[35] Lin EK, Soles CL, Goldfarb DL, Trinque BC, Burns SD, Jones RL, Lenhart JL, Angelopoulos M, Willson CG, Satija SK, Wen-li Wu. Direct measurement of the reaction front in chemically amplified photoresists. Science, vol.297, no.5580, pp.372-5, July 2002.

[36] Croffie E, Lei Yuan, Mosong Cheng, Neureuther A, Houlihan F, Cirelli R, Watson P, Nalamasu O, Gabor A. "Modeling influence of structural changes in photoacid generators on 193 nm single layer resist imaging", J. Vac. Sci. Technol B, vol.18, no.6, pp.3340-4, Nov. 2000.

[37] L. Yuan and A. R. Neureuther, Proc. SPIE, vol. 5039 (2003)

[38] R.J.LeSuer, F.F. Fan, A.J. Bard, J.C. Taylor, P. Tsiartas, C.G. Willson, W.E. Conley, G. Feit and R.R. Kunz, Proc. SPIE, vol. 5376, 115, 2004

[39] I. Grodnensky, K. Suwa, N. Farrar, E. Johnson and J. Pan, "Technique for optical

characterization of exposure tool imaging performance down to 100nm", J. Vac. Sci. Technol. B, 17(6), 3285, Nov/Dec 1999.

[40] L. Yuan, S. Nagahara and A. Neureuther, "Applying Double Exposed Sharp Tip (DEST) Technique to Characterize Material Phenomena in DUV Photoresist", Proc. Of SPIE, vol. 5753, 2005.

[41] I. Grodnensky, K. Suwa, N. Farrar, E. Johnson and J. Pan, "Technique for optical characterization of exposure tool imaging performance down to 100nm", J. Vac. Sci. Technol. B, 17(6), 3285, Nov/Dec 1999

[42] K. Izuha, M. Asano, T. Fujisawa and S. Inoue, "Novel in-situ focus monitor technology in attenuated PSM under actual illumination condition", Proc. SPIE, vol. 5040, 590, 2003.

[43] D. J. H. Funhoff, H. Binder, and R. Schwalm, Proc. SPIE, 1672 (1992) 46

[44] Y. Kawai, A. Otaka, J. Nakamura, A. Tanaka, and T. Matsuda, J. Photopolym. Sci. Tech., 8 (1995) 535.

[45] K. Asakawa, T. Ushirogouchi, and M. Nakase, Proc. SPIE, 2438 (1995) 563.

[46] S. Funato, Y. Kinoshita. T. Kudo, S. Masuda, H. Okazaki, M. Padmanaban, K. J. Przybilla, N. Suehiro, and G. Pawlowski, J. Photopolym. Sci. Tech., 8 (1995) 543.

[47] S. Saito, N. Kihara, T. Naito, M. Nakase, T. Nakasugi, and Y. Kato, Proc. SPIE, 3049 (1997) 659.

[48] J. Hatakeyama, S. Nagura and T. Ishihara, J. Photopolym. Sci. Technol., Vol.13, (2000) 519.

[49] D. Van Steenwinckel, M. Shimizu and J. H. Lammers, Advances in Imaging Materials and Processes, edited by H. Ito, P. R. Varanasi, M. M. Khojasteh and R. Chen

(2004) 149

[50] T. Kai, S. Nishiyama, A. Saitou, and T. Shimokawa, J. Photopolym. Sci. Tech., 16 (2003) 447.

[51] R. L. Brainard, J. Cobb, and Charlotte A. Cutler, J. Photopolym. Sci. Technol., Vol.16, (2003) 401

[52] K. Hattori, J. Abe, and H. Fukuda, Proc. SPIE, 4691 (2002) 1243

[53] T. B. Michaelson, A. T. Jamieson, J. Byers, and C. G. Willson, Proc. SPIE, 4691 (2002) 1243

[54] M. D. Smith, C. A. Mack, J. D. Byers, Proc. SPIE, 5977 (2004) 1482

[55] T. B. Michaelson, A. T. Jamieson, J. Byers and C. G. Willson, "Understanding the role of base quenchers in photoresists", Proc. Of SPIE, 5977 (2004)

[56] S. Nagahara, L. Yuan, W.J. Poppe, A. Neureuther, Y. Kono, A. Sekiguchi, K. Fujiwara, T. G. Watanabe, K. Taira, S. Kusumoto, T. Nakano and T. Shimokawa, "understanding quencher mechanism by considering photoacid-dissociation equilibrium in chemically amplified resist", Proc. Of SPIE, vol. 5753, 2005

[57] L. W. Flanagin, W. K. Singh and C. G. Willson, J. Vac. Sci. Technol, B, vol. 17(4), 1371 (1999)

[58] G. M. Schmid, M. D. Smith, C. A. Mack, V. K. Singh, S. D. Burns and C. G. Willson, Proc. SPIE, vol. 4345, 1037 (2001)

[59] M. D. Stewart, G. M. Schmid, D. L. Goldfarb, M. Angelopoulos and C. G. Willson, Proc. SPIE, vol. 5039 (2003)

[60] A. R. Pawloski, J. A. Torres, P. F. Nealey and J. J. de Pablo, J. Vac. Sci. Technol, B, vol. 17, 3371 (1999)

[61] L. E. Ocola, P. A. Orphanos, W. Y. Li, W. Waskievicz, A. E. Novembre and M. Sato, J. Vac. Sci. Technol, B, vol. 18, 3435 (2000)

[62] J. Cobb, F. Houle, and G. Gallatin, Proc. SPIE, vol. 5037, 397 (2003)

[63] H. Smith, J. Vac. Sci. Technol, B, vol. 4, 148 (1986)

[64] H. Smith, J. Vac. Sci. Technol, B, vol. 6, 346 (1988)

[65] S. C. O'Brien and M. E. Mason, Proc. SPIE, vol. 4346, 534 (2001)

[66] G. M. Gallatin and J. A. Liddle, Microelectronic Engineering, vol. 46, 365 (1999)

[67] G. M. Gallatin, Proc. SPIE, vol. 4404, 123 (2001)

[68] A. Neureuther and F. Pease, "Shot noise models for sequential processes and the role of lateral mixing", to be presented in EIPBN 2005.

[69] L. Yuan and A. Neureuther, "Investigation of shot noise induced line-edge roughness in chemically-amplified resist by continuous-model based simulation", Proc. of SPIE, Vol. 5376, 2004.

[70] Y. Granik and N. Cobb, Proc. of SPIE, Vol. 5040, pp.1166 (2003)

[71] Y. Granik, N. Cobb and T. Do, "Universal process modeling with VTRE for OPC", Proc. of SPIE, vol. 4691, pp.377 (2002)

[72] Y. Granik, Proc. of SPIE, "Correction for etch proximity: new models and applications", vol. 4346, pp.98 (2001)

[73] T. A. Brunner, R. A. Ferguson, "Approx. models for resist processing effects", Proc. of SPIE, vol. 2726, 198 (1996)

[74] J. Randall, K. Ronse, T. Marschner, M. Goethals and M. Ercken, "Variable threshold resist model for lithography simulation", Proc. of SPIE, vol. 3679, pp.176 (1999)

[75] J. Randall, H. Gangala and A. Tritchkov, "Lithography simulation with aerial image –

variable threshold resist model", Microelcctronics Engineering, vol. 46, pp.59 (1999)

[76] T. Brunner, C. Fonseca, N. Seong and M. Burkhardt, "Impact of resist blur on MEF, OPC and CD control", Proc. Of SPIE, vol. 5377, 141, 2004

[77] C. Mack, Proc. of SPIE, "Enhanced lumped parameter model for photolithography", vol. 2197, pp. 501 (1994)

[78] M. D. Smith and C. A. Mack, "Processing sensitivity and optimization with full and simplified resist models", Proc. of SPIE, vol. 5040, pp.1509 (2003)

[79] E. Croffie, "Simulation tools for optical resist models STORM", PhD dissertation, 2001.

[80] L. Yuan and A. Neureuther, Proc. of SPIE, Vol. 4690, 2002.

[81] M. Williamson and A. Neureuther, Proc. of SPIE, Vol. 4690, 2002

[82] K. Izutsu, "Hisuiyoueki no denkikagaku"; Baifukan, (1995), p48, p53 (in Japanese); K. Izutsu, "Electrochemistry in Nonaqueous Solutions", Wiley-VCH, Weinheim, (2002); Nihon Kagakukai, "Kagaku Binran Kisohen II," Maruzen, 322 (in Japanese); K. Izutsu, "Acid-Base Dissociation Constants in Dipolar Aprotic Solvents," Blackwell Sci.

[83] A. Sekiguchi, Y. Kono and Y. Sensu, J. Photopolym. Sci. Technol., Vol.16, (2003) 209

[84] A. Neureuther and F. Pease, "Shot noise models for sequential processes and the role of lateral mixing", EIPBN, 2005.

[85] M. Williamson and A. R. Neureuther, Proc. SPIE, vol. 5039, pp. 423,2003

[86] Privite communication

[87] S. Tsuboi, Y. Yamashita, T. Matsuo et al, "X-Ray mask distortion induced in back-etching preceding subtractive fabrication: resist and absorber stress effect", Jpn. J. Appl.

Phys. Vol. 35, 2845, 1996.

[88] S. Tsuboi, Y. Yamashita and S. Mitsui, "Highly sensitive and stress free chemically-amplified negative working resist, TDUR-N9, for 0.1um synchrotron radiation (SR) lithography", Jpn. J. Appl. Phys. Vol. 35, L130, 1996.

[89] Shumway MD, Snow EL, Goldberg KA, Naulleau P, Cao H, Chandhok M, Liddlc JA, Anderson EH, Bokor J. "EUV resist imaging below 50 nm using coherent spatial filtering techniques", Proc. Of SPIE, vol.5374, no.1, 2004, pp.454-9. USA.

[90] Michael D. Shumway, Patrick P. Naulleau, Kenneth A. Goldberg, Eric L. Snow, and Jeffrey Bokor, "Resist evauation at 50 nm in the EUV using interferometric spatial-frequency-doubled imaging", Proc. Of SPIE 5037 910, 2003.

[91] A.C. Ouano and J.A. Carothers, "Dissolution dynamics of some polymers: solvent-polymer boundaries", Polymer Engineering and Science, vol. 20, No.2, 160, 1980. (104)

[92] C.Y. Ryu, J. Ruokolainen, G.H. Fredrickson and E.J. Kramer, "Chain architecture effects on deformation and fracture of block copolymer with unentangled matrices", Macromolecules, vol.35, 2157, 2002

[93] J. Ruokolainen, G.H. Fredrickson and E.J. Kramer, "Effect of thermal history and microdomain orientation on deformation and fracture properties of poly(cyclohexylethylene)-Polyethylene triblock copolymers containing cylindrical PE domains", Macromolecules, vol. 35, 9391, 2002

[94] P. M. Dentinger, L. L. Hunter, D. J. O'Connell, S. Gunn, D. Goods, T. H. Fedynyshyn, R. B. Goodman and D. K. Astolfi, J. Vac. Sci. Technol, B, vol. 20(6), 2962 (2002)

[95] L. Yuan, A. Neureuther and E. Croffie, "Fast resist model and its application in

model-based OPC for 193nm lithography", Proc. of SPIE, Vol. 5376, 2004

[96] E. Croffie, M. Cheng, Zuniga, M, A.R. Neureuther, "Efficient simulation of post-exposure bake processes in STORM", SPIE, vol.3678, p.1227-34, 1999.

[97] D. Fuard, M. Besacier, P. Schiavone, "Assessment of different simplified resist models", Proc. of SPIE, vol. 4691, pp. 1266 (2002)

[98] A. Krasnoperova, M. Khan, S. Rhyner, J. Taylor, Y.Z. Chu and F. Cerrina, J. Vac. Sci. Technol. B, 12(6), 3900, 1994

[99] H. Fukuda, S. Okazaki, "Kinetics model and simulation for chemically amplified resist", J. Electrochem Soc., vol.137, no.2, 675, 1990

[100] J. Byers, C. Mack, R. Huang, S. Jug, "Automatic calibration of lithography simulation parameters using multiple data sets", Microelectronics Engineering, vol. 61, 89, 2002.

[101] W. Hinsberg, J. Hoffnagle and F. Houle, "Chemistry and physics of the post-exposure bake process in a chemically-amplified resist", Microlithography World, vol. 9, no.2, 16, 2000

[102] W. Hinsberg, F. Houle, M. Sanchez, J. Hoffnagle, G. Wallraff, D. Medeiros, G. Gallatin and J. Cobb, "Extendibility of chemically amplified resists: another brick wall", Proc. Of SPIE, vol. 5039, 2003.(invited paper)

[103] G. Wallraff, J. Hutchinson, W. Hinsberg, F. Houle, P. Seidel, "Kinetics of thermal and acid-catalyzed deprotection in deep-UV resist materials", Microelectronics Engineering, vol. 27, 397, 1995.

[104] Mosong Cheng, Lei Yuan, Croffie E, Neureuther A. Improving resist resolution and sensitivity via electric-field enhanced post-exposure baking. [Journal Paper] Journal of Vacuum Science & Technology B, vol.20, no.2, March 2002, pp.734-40. Publisher: AIP

for American Vacuum Soc, USA.

[105] M. Cheng, E. Croffie and A. Neureuther, Proc. of SPIE, vol.3678, 1999

[106] E. Croffie, M. Cheng, A. Neureuther, R. Cirelli, F. Houlinhan, J. Sweeney, P. Watson, O. Nalamasu, I. Rushkin, O. Dimov, A. Gabor, "Overview of the STORM program application to 193nm single layer resists", Microelectronic Engineering, Vol.53, (no.1-4), pp.437-442, 1998.

[107] Zuniga, M, "Fundamental mechanism in advanced resist system in optical lithography", PhD thesis, University of California at Berkeley

[108] M. Cheng, E. Croffie and A. Neureuther, "Fast imaging algorithm for simulating pattern transfer in DUV resist and extracting post exposure bake parameters", Proc. of SPIE, vol.3999, Part.1, pp.854-864, March, 2000

[109] Mosong Cheng, Croffie E, Lei Yuan, Neureuther A. Enhancement of resist resolution and sensitivity via applied electric field. [Conference Paper] AIP for American Vacuum Soc. Journal of Vacuum Science & Technology B, vol.18, no.6, Nov. 2000, pp.3318-22. USA

[110] T.Watanabe, Y. Yamashita, J. Vac. Sci. Technol. B, 12(6), 3879, 1994

[111] J.R. Sheats and B.W. Smith (edit), "Microlithography: science and technology", Lattics Press, 1998.

[112] Joseph W. Goodman, "Statistical optics", 1985.

[113] Harry Levinson, "Principles of lithography", SPIE Press, 2001.

[114] Alfred Kwok-Kit Wong, "Resolution Enhancement technique in optical lithography", SPIE Press, 2001.

[115] Alfred Kwok-Kit Wong, "Optical Imaging in Projection Microlithography", SPIE

Press, 2005.

[116] O.C. Zienkiewicz and R.L. Taylor, "The Finite Element Method 2, Solids and Fluid Mechanics, Dynamics and Non-Linearity", McGraw Hill, 1991.